MULTICHANNEL BLIND DECONVOLUTION OF CIRCULARLY POLARIZED IMAGERY

DISSERTATION

Patrick B. Cunningham, Major, USAF

AFIT-ENG-DS-22-S-014

DEPARTMENT OF THE AIR FORCE
AIR UNIVERSITY

AFIT AIR FORCE INSTITUTE OF TECHNOLOGY

AFIT-ENG-DS-22-S-014

MULTICHANNEL BLIND DECONVOLUTION OF CIRCULARLY POLARIZED IMAGERY

DISSERTATION

Presented to the Faculty

Department of Electrical Engineering

Graduate School of Engineering and Management

Air Force Institute of Technology

Air University

Air Education and Training Command

In Partial Fulfillment of the Requirements for the

Degree of Doctor of Philosophy

Patrick B. Cunningham, BS EE, MS EE

Major, USAF

August 2022

AFIT-ENG-DS-22-S-014

MULTICHANNEL BLIND DECONVOLUTION OF CIRCULARLY POLARIZED IMAGERY

Patrick B. Cunningham, BS EE, MS EE

Major, USAF

Committee Membership:

Maj David J. Becker, PhD
Chair

Christine Schubert Kabban, PhD
Member

Matthew J. Vincie, PhD
Member

Maj Tyler J. Hardy, PhD
Member

ADEDJI B. BADIRU, PhD
Dean, Graduate School of Engineering and Management

AFIT-ENG-DS-22-S-014

Abstract

Manmade objects tend to be more polarized than natural objects. This allows polarization to be a viable detector for terrestrial manmade targets by discriminating between the targets and their natural background [1]. The two main ways of describing polarized light are Jones vectors and Stokes vectors. Stokes vectors, the version that will be analyzed here, describes the light's intensity in terms of total intensity, linearly polarized light, and circularly polarized light. Currently, a method developed by Dr. Cain and Dr. Lemaster, can be used to recreate an expected Stokes polarization vector from returning light [2]. This method currently applies to three of the Stokes parameters, that is, the linear polarization components, but can be expanded to include circular polarization. Circular polarization is not currently being utilized for object characterization because the mathematical complexity is greater than for that of linear polarization. This research will analyze a way to expand existing algorithms to include circular polarization and enable the complete reconstruction of the Stokes vector from the measured light.

Acknowledgments

I would like to express my sincere appreciation to my faculty advisor, Dr. David Becker, for his guidance and support throughout the course of this thesis effort. I am also thankful that Dr. Daniel Lemaster was willing to take the time to help me better understand his work. Their insight and experience were certainly appreciated.

I would also like to thank the rest of my committee, Dr. Matthew Vincie, Dr. Schubert Kabban, and Dr. Tyler Hardy for taking the time to review this research. I am also grateful to my wife, for having faith in me throughout this process and helping me out when I needed it. Finally, I would like to thank God for giving me the strength and perseverance to get through this rigorous program.

Patrick B. Cunningham

Table of Contents

List of Figures

MULTICHANNEL BLIND DECONVOLUTION OF CIRCULARLY POLARIZED IMAGERY

1. Introduction

1.1. Chapter Overview

This chapter starts with the motivation for exploration and expansion of polarimetric based target detection/characterization. Then, it shall go into the different tasks necessary to complete the research. Following this, the chapter lists the various assumptions made in developing this research. Lastly, the chapter lists an overall chapter by chapter layout of the remainder of the document.

1.2. Motivation

The ability to monitor the health of a satellite is important to its maintenance. In geosynchronous orbit, this can be difficult due to the inability to resolve images. Polarimetry techniques may allow a sensor to tell the difference between an inactive space rock and a satellite that is active. Polarimetry enables the detection of acoustic vibrations which is for detecting if an electrical system is on [3]. However, in addition to detecting the difference between a manmade and naturally occurring orbital object, it is also important to be able to characterize the objects themselves. It should come as no surprise that the current National Security Space Strategy states that "space is vital to U.S. national security and our ability to understand emerging threats, project power globally, conduct operations, support diplomatic efforts, and enable global economic viability" [4]. After all, today, on the civilian side, we depend on orbital satellites for everything from banking to

internet access to travel directions. On the military side, we are even more dependent upon situational awareness, which largely depends upon space dominance. To this end, the 2010 U.S. National Space Policy directs us to develop methods and technologies which are able to "detect, identify, and attribute actions in space that are contrary to responsible use and the long-term sustainability of the space environment" as well as "pursue capabilities to detect, track, catalog, and characterize near-Earth objects to reduce the risk of harm to humans from an unexpected impact on our planet and to identify potentially resource-rich planetary objects" [5].

While many methods currently exist to attempt to detect/characterize objects, these all rely on linear polarization. Linear polarization methods have the advantage of enabling passive detection. For example, when unpolarized solar light reflects off of a manmade object, the Degree of Linear Polarization (DoLP) typically increases [6], [7]. This allows the sensor to detect the object's presence without using any active means, which can sometimes give away the sensor's location/intent.

Circular polarization very rarely occurs naturally and thus, a sensor that utilizes it will not find anything using passive detection methods [8]. However, if a beam of circularly polarized light is used to illuminate a target, the response can be measured and characterized. This allows for the detection of characteristics (specifically, certain portions of the Mueller matrix of a material) that are not currently measured. This research develops a means of expanding the current linear polarization Generalized Expectation Maximization (GEM) algorithms to include circular polarization for active detection. These GEM algorithms are designed to be used with a blind deconvolution algorithm.

1.3. Research Tasks

1. Develop a way to characterize circular polarization.
2. Develop an algorithm to express circular polarization in terms of the variables used in Dr. Lemaster's dissertation [2].
3. Validate the algorithm through simulations/laboratory experiments.

1.4. Assumptions and Limitations

The following assumptions are made throughout this research, unless otherwise stated.

1. Both photon counting noise and background noise follows a Poisson distribution.
2. The background noise is unpolarized.
3. No circular polarization is generated naturally.
4. The intensities of the light on different pixels on the Charged Coupled Device (CCD) are statistically independent.

1.5. Document Outline

In this dissertation, chapter 2 outlines some background work that was discovered during the literature review. The papers that were reviewed focused mostly on polarimetric sensing techniques. This chapter will discuss previous work done in this field and how this work can be improved. It then goes on to explain the GEM method in more depth as well

as how it will be improved. Next, chapter 3 describes the methodology used to complete this research. Chapter 4 displays the results of the experiments described in chapter 3, and chapter 5 draws conclusions from the result in chapter 4 as well as recommendations for potential future research in this area.

2. Background and Literature Review

2.1. Chapter Overview

This chapter discusses the background and literature review that was utilized by this research. It will begin with a brief overview of imaging in general. Next it will discuss atmospheric phase screens and methods of modelling them, followed by a discussion of polarimetry to include Jones and Stokes vectors (two methods of describing polarization states). Then, an overview of GEM will be given as well as its current and potential uses. Lastly, some potential improvements will be analyzed in more depth.

2.2. Imaging

A camera measures the irradiance of the light that reaches a given pixel [8]. The idea is that, based on the irradiance at that pixel, and given knowledge of the path that the light travels, you can calculate the light reflected off of (or in some cases emitted by) the object. Additionally, if you go back a step further and know the characteristics of the light that reached the object, you can calculate the reflectance parameters of that object. While this may sound simple, phenomenon such as atmospheric aberrations can severely limit your knowledge of the effects of the path on the light. Thus, the data collected by the camera (also known as the image) can be described by Equation (2.1) where $i(y)$ is the received irradiance at the plane of the image on the detector array, per pixel (in the image plane coordinates), y, $o(x)$ is the reflected irradiance of the object, per pixel (in the object

plane coordinates) x, and $h(y-x)$ is the Point Spread Function (PSF). y and x are shorthand for (y_1, y_2) and (x_1, x_2) in the two dimensional case. In the discrete case, this obviously simplifies this expression in Equation (2.2) which is much more manageable. [9]

$$i(y) = \int_{-\infty}^{\infty}\int_{-\infty}^{\infty} o(x_1, x_2)\, h\big((y_1 - x_1) - (y_2 - x_2)\big)\, dx_1 dx_2 = \int_{-\infty}^{\infty} o(x)\, h(y-x)\, dx\,. \qquad (2.1)$$

$$i(y) = \sum_{x} o(x_1, x_2)\, h\big((y_1 - x_1) - (y_2 - x_2)\big) = \sum_{x} o(x)\, h(y-x)\,. \qquad (2.2)$$

Thus, for an ideal situation, $h(y-x) = \delta(y-x)$, leading the recovered image to be identical to the irradiance at the object plane ($i = o$). However, in the real world there are effects that cause the PSF, h, to deviate from a δ function. Two of the effects that will be discussed here are diffraction and atmospheric turbulence. The image is degraded by diffraction as a function of the aperture size. This ultimately limits the image resolution. The diffraction effect on the PSF, which includes the effect of the aperture size, is shown below in Equation (2.3) for the continuous case and Equation (2.4) for the discrete case as $h_{diffraction}(x)$. $A(u)$ describes the aperture function (the shape of the aperture), u describes the coordinate system inside the aperture plane, and k is a constant related to the wavelength and the propagation distance. [10]

$$h_{diffraction}(x) = \left| \int_{-\infty}^{\infty} A(u)\, e^{-2j\pi kxu}\, du \right|^2 . \qquad (2.3)$$

$$h_{diffraction}(x) = \left| \sum_{u} A(u)\, e^{-2j\pi kxu} \right|^2 . \qquad (2.4)$$

The second, and more complex cause of image path degradation is atmospheric turbulence. Atmospheric turbulence causes a phase shift in the light that passes through it on the basis of temperature and pressure at a given location and time. Thermal eddies create a temperature gradient which causes the index of refraction to change. When this is happening independently in many regions within the field of view, this produces a phase shift in the light for one region relative to another [11]. Mathematically, this is defined as $e^{j\varphi(u)}$, where φ is the random phase effect cause by the propagation of the light through the atmosphere. While a more thorough treatment of this topic can be found in [8], the combined equation for the two effects are given in Equation (2.5) for the continuous case and Equation (2.6) for the discreet case.

$$h(x) = \left| \int_{-\infty}^{\infty} A(u) e^{-2j\pi kxu} e^{j\varphi(u)} du \right|^2 . \tag{2.5}$$

$$h(x) = \left| \sum_{u} A(u) e^{-2j\pi kxu} e^{j\varphi(u)} \right|^2 . \tag{2.6}$$

2.3. Atmospheric Phase Screens

There are two primary methods of simulating atmospheric phase screens. One is known as the Zernike method and the other the Fourier Transform method [11] [12]. The Fourier Transform method is much faster to compute, but has been shown to have errors when dealing with lower spatial frequency harmonics [11] [13]. Because computation time was not a concern, the Zernike method was used in this research.

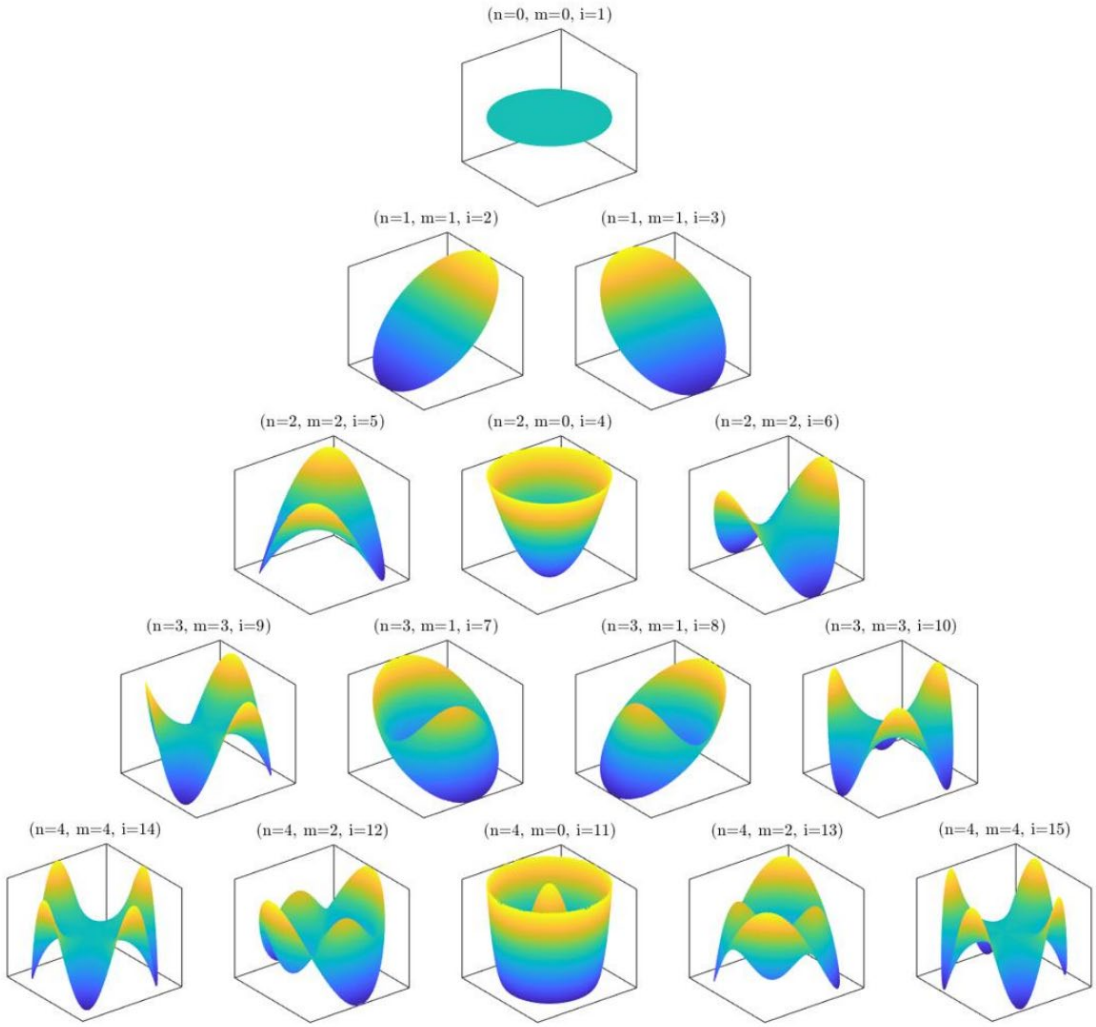

Figure 1: Zernike Phase Screen Pictorial [14]

The Zernike method utilizes a series of polynomials each representing a different type of aberration. Figure 1 shows what the individual phase screens for fifteen of these would look like. Each of the polynomials that are used in the approximation are weighted and then added together to produce the total phase screen.

The Zernike polynomials are a set of polynomials defined on a unit circle, with a key property of being orthogonal over the unit circle. The Zernike polynomials are defined as follows [14]: the equation for a Zernike polynomial is given in Equation (2.7), where *r*

and θ define the polar coordinates, Z_i is the i[th] Zernike polynomial, m is the azimuthal frequency and n is the radial degree. $R_n^m(r)$ is the radial factor and is defined in Equation (2.8). $G^m(\theta)$ is known as the annular factor and is defined in Equation (2.9).

$$Z_i(r,\theta) = \begin{cases} \sqrt{2(n+1)} R_n^m(r) G^m(\theta) & m \neq 0 \\ R_n^0(r) & m = 0 \end{cases}. \tag{2.7}$$

$$R_n^m(r) = \sum_{s=0}^{(n-m)/2} \frac{(-1)^s (n-s)!}{s!\left(\frac{n+m}{2}-s\right)!\left(\frac{n-m}{2}-s\right)!} r^{n-2s}. \tag{2.8}$$

$$G^m(\theta) = \begin{cases} \sin(m\theta) & i \text{ odd} \\ \cos(m\theta) & i \text{ even} \end{cases}. \tag{2.9}$$

These polynomials are then weighted and added together to produce the phase screen, φ, in Equation (2.6) that is used in the various simulation. This is expressed mathematically in Equation (2.10) where C_i is the Zernike coefficient that describes the weighting value of the *i*th Zernike polynomial [14]. The number of coefficients needed depends on the ratio of the aperture diameter (*d*) and the atmospheric seeing parameter (r_0).

$$\varphi(r,\theta) = \sum_{i=1}^{i=i_{\max}} C_i Z_i(r,\theta). \tag{2.10}$$

In the simulations performed throughout this research, the phase screens were created by MATLAB programs called `zern_phase_screen` [15]. This program utilizes a common method of simulating atmospheric turbulence by the creation of Zernike polynomials. It utilizes the coherence diameter (r_0), the size of the pupil (*d*), the number

of pixels in the scene (N) and the number of Zernike coefficients to calculate. In the baseline simulation, when $\frac{d}{r_0} = 10$, 100 Zernike polynomials were used. In other words, $i_{\max} = 100$.

2.4. Polarimetry

One of the most commonly accepted methods for describing light is as a transverse electric field traveling in the z direction. In unpolarized light, this field has a random and generally unpredictable polarization angle. In linearly polarized light, the polarization angle is constant. Linear polarization is typically achieved by placing a polarization filter (also known as a polarization analyzer) in front of a source. The filter blocks out all light that does not have the appropriate polarization angle, thus the only light passing through is 'polarized' at the permissive angle. These angles are generally described as the combination of $\overrightarrow{E_x}$ and $\overrightarrow{E_y}$. $\overrightarrow{E_x}$ is a vector in the x direction of magnitude E_x, representing the portion of electric field vector in the x direction and $\overrightarrow{E_y}$ is a vector in the y direction of magnitude E_y, representing the portion of light that is polarized in the y direction. Both of these vectors oscillate in a waveform as described in Equations (2.11) and (2.12), where ω is the temporal frequency of the light (proportional to the wavelength), t is the time, k the spatial frequency of light, and z is the location in the direction of propagation. The term ε, is the phase difference between $\overrightarrow{E_y}$ and $\overrightarrow{E_x}$, which is 0 in the case of linearly polarized light. The polarization angle of the field is said to be the angle of the sum of the two vectors at a given point. A visual representation of this case is shown in Figure 2.

$$\overrightarrow{E_x}(z,t) = E_x \cos(kz - \omega t)\,. \tag{2.11}$$

$$\overrightarrow{E_y}(z,t) = E_y \cos(kz - \omega t - \varepsilon)\,. \tag{2.12}$$

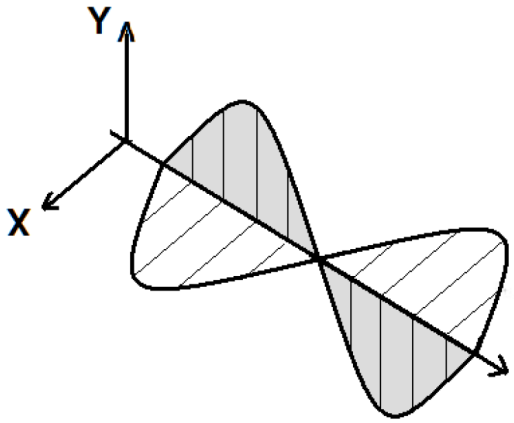

Figure 2: Linear Polarization [6]

Partially polarized light consists of a combination of both polarized and unpolarized light. This is achieved when you have light from a polarized source and natural light reaching your sensor at the same time [10]. The unpolarized portion of partially polarized light perturbs the polarization angle from its expected angle.

The resulting field can be measured by a set of three channels. One channel is unfiltered. This gives the total intensity of the field. The remaining two channels are orthogonally polarized filters at the receiver, one to measure the intensity of E_x and one to measure the intensity of E_y. It is worth noting that the measured quantity of total intensity in terms of photoelectrons is actually equal to the sum of E_x^2 and E_y^2 as shown in Equation

(2.13). $\overline{E}$ is the sum of the two vectors $\overline{E_x}$ and $\overline{E_y}$. This is shown below in Equation (2.14). The angle of polarization is $\tan^{-1}\left(\overline{E_x} / \overline{E_y}\right)$.

$$I = E_x^2 + E_y^2. \tag{2.13}$$

$$\overline{E} = \overline{E_x} + \overline{E_y}. \tag{2.14}$$

2.4.1. Stokes Parameters

One common method of expressing polarimetric data is through a Stokes vector, $\overline{S}$. The Stokes vector is composed of four different parameters (also known as the Stokes parameters). These will be referred to as S_0, S_1, S_2, and S_3. The vector itself, $\overline{S}$, is shown below in Equation (2.15). S_0 denotes the total intensity of the vector (typically normalized to 1). S_1 is a function of the amount of light that is polarized in either the horizontal or vertical direction. Thus, when the polarization state is horizontal, $S_1 = 1$, and when the light is completely vertical, $S_1 = -1$. S_2 is a function of the component of light with a polarization angle, α, of $45°$ (midway between the two extremes for S_1). S_3 is a function of the intensity of the light that is circularly polarized. A list of common Stokes vectors is shown below in Table 1 for reference. The physical definitions of the respective Stokes parameters are shown below in Equation (2.16).

One advantage presented by using Stokes vectors is that they can be calculated from intensities which can be directly measured. A downside of the Stokes vector, from a

physical modeling perspective is that, with the exception of S_0, the other parameters can be negative. This poses a problem for statistical modeling because Poisson distributions only deal with positive numbers [6]. This is problematic because photon arrival at a CCD is governed by a Poisson distribution and a Poisson distribution cannot have a negative value [16].

$$\overline{S} = \begin{bmatrix} S_0 \\ S_1 \\ S_2 \\ S_3 \end{bmatrix}. \tag{2.15}$$

$$\begin{aligned} S_0 &= \langle E_x \rangle^2 + \langle E_y \rangle^2 \\ S_1 &= \langle E_x \rangle^2 - \langle E_y \rangle^2 \\ S_2 &= \langle 2E_x E_y \cos\varepsilon \rangle \\ S_3 &= \langle 2E_x E_y \sin\varepsilon \rangle \end{aligned} \text{ . [10]} \tag{2.16}$$

Table 1: Stokes Vector Descriptions [10]

Description	Stokes Vector
Horizontal	$\begin{bmatrix}1\\1\\0\\0\end{bmatrix}$
Vertical	$\begin{bmatrix}1\\-1\\0\\0\end{bmatrix}$
+45º	$\begin{bmatrix}1\\0\\1\\0\end{bmatrix}$
-45º	$\begin{bmatrix}1\\0\\-1\\0\end{bmatrix}$
Right Hand Circular	$\begin{bmatrix}1\\0\\0\\1\end{bmatrix}$
Left Hand Circular	$\begin{bmatrix}1\\0\\0\\-1\end{bmatrix}$

The fact that the Stokes parameters represent an easily measurable quantity, the light's intensity, allows the individual Stokes parameters to be calculated from the results of a data collect using four different polarization analyzers (three if circular polarization is ignored). The first is simply a filter that reduces all light passing through by 50%. The resulting intensity is I_0. The second is a horizontally polarized filter. The intensity that it reads is

known as I_1. The third channel contains a filter polarized in $\phi = 45°$. Its intensity is referred to as I_2. Finally, the fourth channel uses a circular polarizer opaque to L-state polarized beams. Its intensity is I_3. The relationship between these four intensities and their resulting Stokes vector parameters is shown below in Equation (2.17). Because this equation contains the total intensity (I_0), it is possible to back calculate how polarized the light is, in addition to its polarization angle. These Stokes vectors are usually normalized (though it is not required), which simply means the vector is divided by S_0 [10]. This convention is shown below in Equation (2.18).

$$\begin{bmatrix} 2I_0 \\ 2I_1 - 2I_0 \\ 2I_2 - 2I_0 \\ 2I_3 - 2I_0 \end{bmatrix} = \begin{bmatrix} S_0 \\ S_1 \\ S_2 \\ S_3 \end{bmatrix}. \tag{2.17}$$

$$S_0 \begin{bmatrix} 1 \\ \dfrac{2I_1 - 2I_0}{2I_0} \\ \dfrac{2I_2 - 2I_0}{2I_0} \\ \dfrac{2I_3 - 2I_0}{2I_0} \end{bmatrix} = \begin{bmatrix} S_0 \\ S_1 \\ S_2 \\ S_3 \end{bmatrix}. \tag{2.18}$$

2.4.2. Circular Polarization

Circular polarization occurs when $\varepsilon \neq 0$ from Equation (2.12). As a result of the offset along the *z* axis of the two fields $\overline{E_x}(z,t)$ and $\overline{E_y}(z,t)$ (from Equations (2.11) and (2.12) respectively), the angle of polarization is no longer constant in the direction of propagation.

Because the angle is nonconstant, it is more difficult to model. This is displayed visually in Figure 3.

Typically, circular polarization is only monitored in active sensing. Passive sensing depends upon the reflection of natural light off of an object. Because circular polarization is not naturally occurring, it is therefore not a factor in passive imaging [6] [8]. Active sensing, by contrast, utilizes a controlled source. This source could contain circularly polarized light.

The DoLP of a measurement refers to the amount of the incoming light that is linearly polarized, as described below in Equation (2.19) [2]. While most of the GEM discussion will revolve around the DoLP, it is important to distinguish this value from the degree of total polarization, *P*, shown below in Equation (2.20), which includes the circularly polarized component.

$$DoLP = \frac{\sqrt{S_1^2 + S_2^2}}{S_0}. \tag{2.19}$$

$$P = \frac{\sqrt{S_1^2 + S_2^2 + S_3^2}}{S_0}. \tag{2.20}$$

Calculating the polarization angle, α, is shown in below in Equation (2.21) [8].

$$\alpha = \frac{1}{2}\tan^{-1}\left(\frac{S_2}{S_1}\right). \tag{2.21}$$

DoLP does not include circular polarization as a component. Thus, when circular polarization is considered, the polarization factor that is used will not be the DoLP, but will instead be *P* for total polarization.

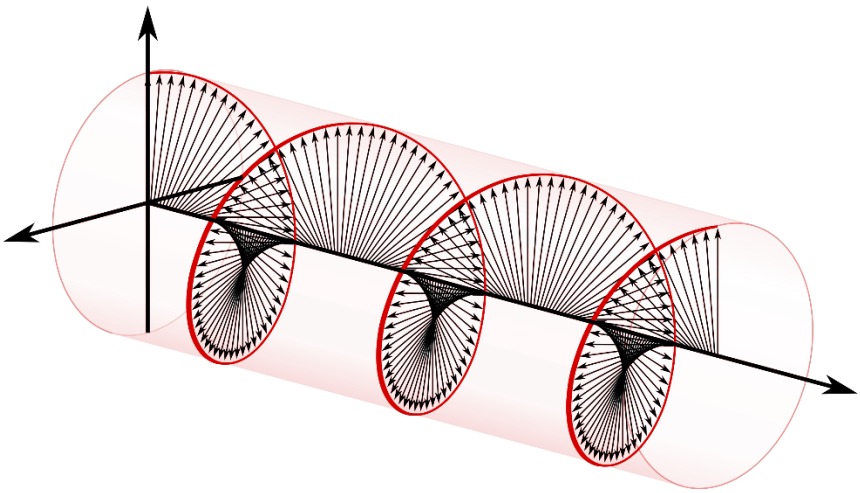

Figure 3: Right Circularly Polarized Light

The direction that the light rotates is determined by ε from Equation (2.12). If the field is rotating clockwise in the direction of propagation (as depicted in Figure 3) the field is considered to be right-circularly polarized. This occurs when $\varepsilon = -\frac{\pi}{2} + 2m\pi$, where *m* is an integer. If the direction of rotation is counter-clockwise, it is considered to be left-circularly polarized. This occurs when $\varepsilon = \frac{\pi}{2} + 2m\pi$.

2.4.3. Mueller Matrices

Once the optical system has taken measurements that can reconstruct the Stokes vector of the light that arrives at the camera, the effect of the interface may be calculated

(assuming the Stokes parameters of the light before it reached that object are known). This can either be reflectance parameters of the object or the effect the interface has on light that passes through it, depending upon the position of the camera [10]. The relationship for calculating a Mueller transform matrix is shown below in Equation (2.22). $\overline{S}_{final}$ is the light that exits the interface, **M** is the Mueller matrix of the interface (which can used to be described as the reflectance parameters of the objects) and $\overline{S}_{initial}$ is the Stokes vector of the light that reaches the interface. Some sample Mueller matrices and their corresponding effects are shown below in Table 2.

$$\overline{S}_{final} = \mathbf{M}\overline{S}_{initial} \tag{2.22}$$

Table 2: Mueller Matrix Examples [10]

Effect	Mueller Matrix
Horizontal Polarizer	$0.5\begin{bmatrix} 1 & 1 & 0 & 0 \\ 1 & 1 & 0 & 0 \\ 0 & 0 & 0 & 0 \\ 0 & 0 & 0 & 0 \end{bmatrix}$
Vertical Polarizer	$0.5\begin{bmatrix} 1 & -1 & 0 & 0 \\ -1 & 1 & 0 & 0 \\ 0 & 0 & 0 & 0 \\ 0 & 0 & 0 & 0 \end{bmatrix}$
+45º Polarizer	$0.5\begin{bmatrix} 1 & 0 & 1 & 0 \\ 0 & 0 & 0 & 0 \\ 1 & 0 & 1 & 0 \\ 0 & 0 & 0 & 0 \end{bmatrix}$
-45º Polarizer	$0.5\begin{bmatrix} 1 & 0 & -1 & 0 \\ 0 & 0 & 0 & 0 \\ -1 & 0 & 1 & 0 \\ 0 & 0 & 0 & 0 \end{bmatrix}$
Quarter Wave Plate; (Fast Axis: Horizontal)	$\begin{bmatrix} 1 & 0 & 0 & 0 \\ 0 & 1 & 0 & 0 \\ 0 & 0 & 0 & 1 \\ 0 & 0 & -1 & 0 \end{bmatrix}$
Quarter Wave Plate (Fast Axis: Vertical)	$\begin{bmatrix} 1 & 0 & 0 & 0 \\ 0 & 1 & 0 & 0 \\ 0 & 0 & 0 & -1 \\ 0 & 0 & 1 & 0 \end{bmatrix}$

2.4.4. Jones Vectors

Thanks to Muller matrices, Stokes vectors are quite effective at displaying the effect of an interface, however, they do not perform well at calculating the propagation of light through a medium. To do this, Jones vectors are used. A Jones vector is a two-element vector describing the light that has a parallel polarization in element one and the light that has a perpendicular polarization in element two as shown below in Equation (2.23) [10], [9]. While Jones vectors are more difficult to measure outright, they are conceptually simpler. Like Stokes vectors, Jones vectors are a way to display the relationship of E_x and E_y however Jones vectors do not, by themselves, contain the information needed to calculate the DoLP or *P*.

$$\overline{J} = \begin{bmatrix} E_x \\ E_y \end{bmatrix}. \tag{2.23}$$

To display circular polarization, phase shifts are utilized, thus the resulting vector elements become complex numbers. Sample Jones vectors are shown below in Table 3.

Table 3: Jones Vector Examples

Description	Jones Vector
Horizontal	$\begin{bmatrix}1\\0\end{bmatrix}$
Vertical	$\begin{bmatrix}0\\1\end{bmatrix}$
+45º	$\frac{1}{\sqrt{2}}\begin{bmatrix}1\\1\end{bmatrix}$
-45º	$\frac{1}{\sqrt{2}}\begin{bmatrix}1\\-1\end{bmatrix}$
Right Hand Circular	$\frac{1}{\sqrt{2}}\begin{bmatrix}1\\-i\end{bmatrix}$
Left Hand Circular	$\frac{1}{\sqrt{2}}\begin{bmatrix}1\\i\end{bmatrix}$

2.4.5. Polarimetric Reflection

Reflective objects reflect polarized light slightly differently than unpolarized light. In addition, they reflect the light differently if it is polarized perpendicularly or in parallel to the plane of incidence. $R_{\parallel}$ describes the ratio of light that is polarized parallel to the incidence plane that reflects off the surface. Similarly, $R_{\perp}$ determines how much

of the light that is perpendicularly polarized with the incidence plane that reflects off of the surface. [10]

2.5. GEM Overview

Collecting polarization data typically requires the utilization of multiple different polarization analyzers. A polarimetric image contains information regarding the polarization state of the object scene. GEM combines the joint likelihood of the outputs of the independent polarization analyzers (each output is a separate polarization channel). The GEM itself is an iterative algorithm for determining the maximum likelihood (ML) estimates of the scene parameters. The GEM is divided into two steps, the Expectation step and the Maximization step. In the Expectation step, the algorithm calculates an expected likelihood value for the complete data (the scene truth, in the case of an optical system) based upon the measured data as well as the previous iteration output of the GEM. In the Maximization step, the parameters are selected such that the likelihood value in the Expectation step is maximized. In other words, the Maximization step selects the parameter set that has the highest likelihood based upon the measured data, *d*, (sometimes referred to as the incomplete data) and the likelihood of the parameter set selected by the previous iteration of the algorithm [2].

2.5.1. GEM Primer

The GEM 'algorithm' is not an algorithm, per se, but a framework for developing the most likely result of a given function [17]. If d is the incomplete data and D is the complete data, than the maximum-likelihood estimate of D given d is defined by the function L, given Equation (2.24) where $g\left(D|d\right)$ is the conditional Probability Density

Function (PDF) of D given d. The goal, is to find the value that gives the D that is most likely to have yielded the d that has been observed. Frequently, this will be an iterative process of guessing a value for D, looking at the resulting $L(D)$, changing D and going back to see if that improved $L(D)$. Two limitations that could be set up as bounds are a limited number of iterations, or a minimum value of $L(D)$.

$$L(D) = g(D|d). \tag{2.24}$$

When the function is discrete this is simply a summation, but this is obviously problematic when the PDF is continuous. Thus, a different set of random variables, z, which depend upon D, can be built. Then the PDF $f(z|d)$ is constructed, such that maximizing $f(z|d)$ is simpler than maximizing $g(D|d)$. Mathematically, this is shown below in Equation (2.25).

$$g(D|d) = \int f(z|d)dz. \tag{2.25}$$

2.5.2. Expectation Step for Three Channel Case

Section 2.5.2, Section 2.5.3, Section 2.5.4, and Section 2.6 largely describe the work done by Dr. Lemaster in [2] and [6]. In generic terms, the Expectation step defines the objective function that is being maximized. For a given iteration, n, the objective function Q^n is the same as the conditional expectation of the complete data log-likelihood, based upon the measured (incomplete) data as well as the previous iteration's estimates of the

function's parameters. In the more specific case of a polarimetric data, the parameters of interest are λ_u, λ_p, h, and α. λ_u represents the amount of light that is unpolarized in the measured sample. By contrast, λ_p represents the amount of light that is (linearly) polarized in the measured sample. h denotes the PSF which describes the transformation that occurs between the source and the plane where the measurement is taken. Equation (2.26) shows how the object function is broken down into the unpolarized and polarized components and Equation (2.27) shows that the image function is a convolution of what the object actually looks like and the PSF. The incomplete data, because it receives both polarized and unpolarized light from a given channel, is displayed in Equation (2.28). The expectation function for the unpolarized and polarized components, for a given channel and *x,y* pair are shown in Equations (2.29) and (2.30), where the subscript *k* is either *u* for unpolarized data or *p* for a polarized data. α describes the angle of polarization of the signal. y is the location in the imaging space, *x*, is the location in the object plane. *o* is the object function, that is, what the object actually looks like, and *i*, the image function, which is the same as the mean of *d*. The subscript *c*, as well as the *c* in the summation, denotes a specific channel which will correspond with a specific polarization angle. For example, θ_c denotes the polarization angle of the polarimeter associated with channel *c*. D_{uc} signifies the unpolarized (subscript *u*) portion of the complete data seen in channel *c*. Similarly, D_{pc} signifies the polarized (subscript *p*) portion of the complete data seen in channel *c*.

$$o_c(x) = \frac{1}{2}\lambda_u(x) + \lambda_p(x)\cos^2\left(a(x) - \theta_c\right). \tag{2.26}$$

$$i_c(y) = \sum_x o_c(x) h_c(y-x). \tag{2.27}$$

$$d_c(y) = \sum_x D_{uc}(y,x) + \sum_x D_{pc}(y,x). \tag{2.28}$$

$$E\left[D_{uc}(y,x)\right] = \frac{1}{2}\lambda_u(x) h_c(y-x). \tag{2.29}$$

$$E\left[D_{pc}(y,x)\right] = \lambda_p(x)\cos^2\left(a(x)-\theta_c\right) h_c(y-x). \tag{2.30}$$

The objective function is defined below in Equations (2.31) and (2.32), where L is the log likelihood of the data. While log likelihood is derived more thoroughly in [2] , it is shown below in Equation (2.33).

$$Q^n\left(\lambda_u,\lambda_p,h,\alpha\right) = E\left[L\left(\lambda_u,\lambda_p,h,\alpha \mid d,\lambda_u{}^{n-1},\lambda_p{}^{n-1},h^{n-1},\alpha^{n-1}\right)\right]. \tag{2.31}$$

$$Q^{n+1}\left(\lambda_u,\lambda_p,h,\alpha\right) = E\left[L\left(\lambda_u,\lambda_p,h,\alpha \mid d,\lambda_u{}^{n},\lambda_p{}^{n},h^{n},\alpha^{n}\right)\right]. \tag{2.32}$$

$$\begin{aligned} &L\left(\lambda_u,\lambda_p,h,\alpha \mid d,\lambda_u{}^{n},\lambda_p{}^{n},h^{n},\alpha^{n}\right) = \\ &\sum_x\sum_y\sum_c\left\{D_{uc}(y,x)\ln\left[\frac{1}{2}\lambda_u(x)h_c(y-x)\right] - \frac{1}{2}\lambda_u(x)h_c(y-x)\right\}. \\ &+\sum_x\sum_y\sum_c\begin{Bmatrix} D_{pc}(y,x)\ln\left[\lambda_p(x)h_c(y-x)\cos^2\left(\alpha(x)-\theta_c\right)\right] \\ -\lambda_p(x)h_c(y-x)\cos^2\left(\alpha(x)-\theta_c\right)\end{Bmatrix} \end{aligned} \tag{2.33}$$

The expectation value itself is defined as $\psi_{kc}^{n+1}(y,x)$ in Equation (2.34). The results for the *u* and *p* portions of the expectation value may be found by referencing back to Equations (2.29) and (2.30) [2].

$$\psi_{kc}^{n+1}(y,x) = E\left[D_{kc}(y,x) \mid d_c,\lambda_k^n,\alpha^n,h_c^n\right]. \tag{2.34}$$

$$\psi_{uc}^{n+1}(y,x) = \frac{1}{2}\frac{d_c^n(y)}{i_c^n(y)}\lambda_u^n(x)h_c^n(y-x). \tag{2.35}$$

$$\psi_{pc}^{n+1}(y,x)=\frac{d_c^n(y)}{i_c^n(y)}\lambda_p^n(x)h_c^n(y-x)\cos^2\left(\alpha^n(x)-\theta_c\right). \tag{2.36}$$

2.5.3. Maximization Step for Three Channel Case

To find the maximization of the likelihood, you must take the derivative of Q^{n+1} with respect to the individual parameter that you are attempting to maximize and set that equal to 0 for a given pixel, x_0. For example, looking at λ_u, λ_p, or α in this case yields: Equations (2.37), (2.38), and (2.39), respectively.

$$\frac{dQ^{n+1}}{d\lambda_p(x_0)}=\sum_y\sum_c\left[\frac{\psi_{pc}^{n+1}(y,x_0)}{\lambda_p(x_0)}\right]-\sum_c\left[\cos^2\left(\alpha(x_0)-\theta_c\right)\right]\equiv 0. \tag{2.37}$$

$$\frac{dQ^{n+1}}{d\lambda_u(x_0)}=\sum_y\sum_c\left[\frac{\psi_{uc}^{n+1}(y,x_0)}{\lambda_u(x_0)}\right]-\frac{C}{2}\equiv 0. \tag{2.38}$$

$$\frac{dQ^{n+1}}{d\alpha(x_0)}=\sum_y\sum_c\left[\psi_{pc}^{n+1}(y,x_0)\tan\left(\alpha(x_0)-\theta_c\right)\right]+\sum_c\left[\lambda_p(x_0)\sin\left(2\left(\alpha(x_0)-\theta_c\right)\right)\right]\equiv 0. \tag{2.39}$$

By choosing θ_c in such a way that the orientations of the polarimeter are evenly distributed over all linear polarization states, some of these terms can be found to simplify into Equation (2.40) where *k* is used to symbolize either *u* for the unpolarized or *p* for the polarized state and *C* is the number of available channels [2] .

$$\lambda_k^{n+1}(x)=\frac{2}{C}\sum_y\sum_c\left[\psi_{kc}^{n+1}(y,x)\right]. \tag{2.40}$$

The polarization angle found from the maximization function can be expressed in terms of the two linearly polarized Stokes parameter estimates via Equation (2.41) [2].

$$\alpha^{n+1}\left(x_0\right)=\frac{1}{2}\tan^{-1}\left(\frac{S_2^{n+1}\left(x_0\right)}{S_1^{n+1}\left(x_0\right)}\right). \tag{2.41}$$

2.5.4. Point Spread Function (PSF) Estimator

The derivative of Q^{n+1} with respect to the PSF, at pixel $z=y-x$ is shown below in Equation (2.42).

$$\frac{dQ^{n+1}}{dh_c\left(z\right)}=\sum_y\frac{\psi_{pc}^{n+1}\left(y,y-z\right)+\psi_{uc}^{n+1}\left(y,y-z\right)}{h_c\left(z\right)}-\sum_y o_c^{n+1}\left(y-z\right). \tag{2.42}$$

Equation (2.42) enables us to use a PSF estimator originated by Schulz [18]. First, use the definition of $A\left(u\right)$ as aperture function, such that $A\left(u\right)=1$ when $u<r$ and $A\left(u\right)=0$ when $u>r$. The resulting definition is shown below in Equation (2.43), which is simply an expansion of the discrete case of Equation (2.6) for an iterative estimation process. k (in the exponential term) is a constant dealing with both the wavelength and sampling effects, and φ_c^{n+1} refers to the current estimate (in the same vein as ψ_c^{n+1} from the previous section) of the atmospherically induced phase modulation for channel *c*. This allows us to use a phase retrieval algorithm from [2] shown below in Equation (2.44) where $\xi\left(x\right)$ is defined in Equation (2.45). $d_c\left(y\right)$ is simply *d* (the incomplete data) at pixel *y* on channel *c*. Therefore, $i_c^n\left(y\right)$ is the mean of n^{th} iteration of the estimation of *i* at pixel *y* on channel *c*. D_c is the complete data on channel *c*. o_c^n is the n^{th} iteration of the estimation of the object function on channel *c*.

$$h_c^{n+1}\left(x,\varphi_c^{n+1}\right)=\left|\sum_u A(u)e^{-i2\pi kux}e^{i\varphi_c^{n+1}(u)}\right|^2. \tag{2.43}$$

$$\varphi_c^{n+1}=\begin{cases}\widetilde{\varphi_c} & \text{if } \sum_x\left(\xi(x)\ln\left[h_c\left(x,\widetilde{\varphi_c}\right)\right]\right)\\ \varphi_c^n & \text{otherwise}\end{cases}. \tag{2.44}$$

$$\xi(x)=\frac{h_c\left(x,\varphi_c^n\right)}{D_c}\sum_y\frac{d_c(y)}{i_c^n(y)}o_c^n(y-x). \tag{2.45}$$

Given Equation (2.46), we can use Equation (2.45), to find Equation (2.47) where $\Im^{-1}$ is an inverse Fourier transform, and phase is a function that extracts the phase angle from a complex number. This GS process is performed multiple times within each GEM iteration.

$$D_c=\sum_x o_c^{n+1}(x)=\sum_y d_c(y). \tag{2.46}$$

$$\widetilde{\varphi}_c=\text{phase}\left[\Im^{-1}\left(\sqrt{\xi\left(x,\varphi_c^n\right)}e^{i(\varphi_c^{n+1}(u)-2\pi kux)}\right)\right]. \tag{2.47}$$

2.6. Existing GEM-based Blind Deconvolution Utilization

The GEM algorithm has been used experimentally in the past to reconstruct the initial polarization angles of measured light. This has been achieved even through a random phase screen, which creates aberrations simulating that of the atmosphere. The experiment in [6] consisted of two bars of light, each fully polarized, at orthogonal polarization angles. Unless the polarization analyzer was set, such that it filtered out all light from one bar, a phase shift dominated. In the end, there was about a 10^{0} bias in the results. The cause of

this bias was not fully understood, though one theory was that the bias was the result of the imperfections in the polarization analyzers.

A different experiment involved the simulation of target data. This scenario was theoretically identical to the first, in that there were two bars polarized at orthogonal polarization angles. Also, atmospheric interference was simulated using the first nine Zernike polynomials. These parameters were input into a MATLAB simulation which assumed a Poisson distribution for all relevant light sources.

The results of these experiments were quantified with a Normalized Mean Squared Error (NMSE) measurement shown in Equation (2.48) where $\hat{f}(x)$ is the individual estimate and $f(x)$ is the known truth.

$$NMSE = \frac{\Sigma\left[f(x) - \hat{f}(x) \right]^2}{\sum f^2(x)}. \tag{2.48}$$

The results of the error for the three linear Stokes parameters are shown below in Figure 4. The graphs depict the *median* (the second quartile) with bars representing the first and third quartile limits. This means that 50% of the data is contained within the bars (so 25% is above the median and 25% is below the median). The median was used, as opposed to the mean and standard deviation, to avoid having negative values for the lower NMSE.

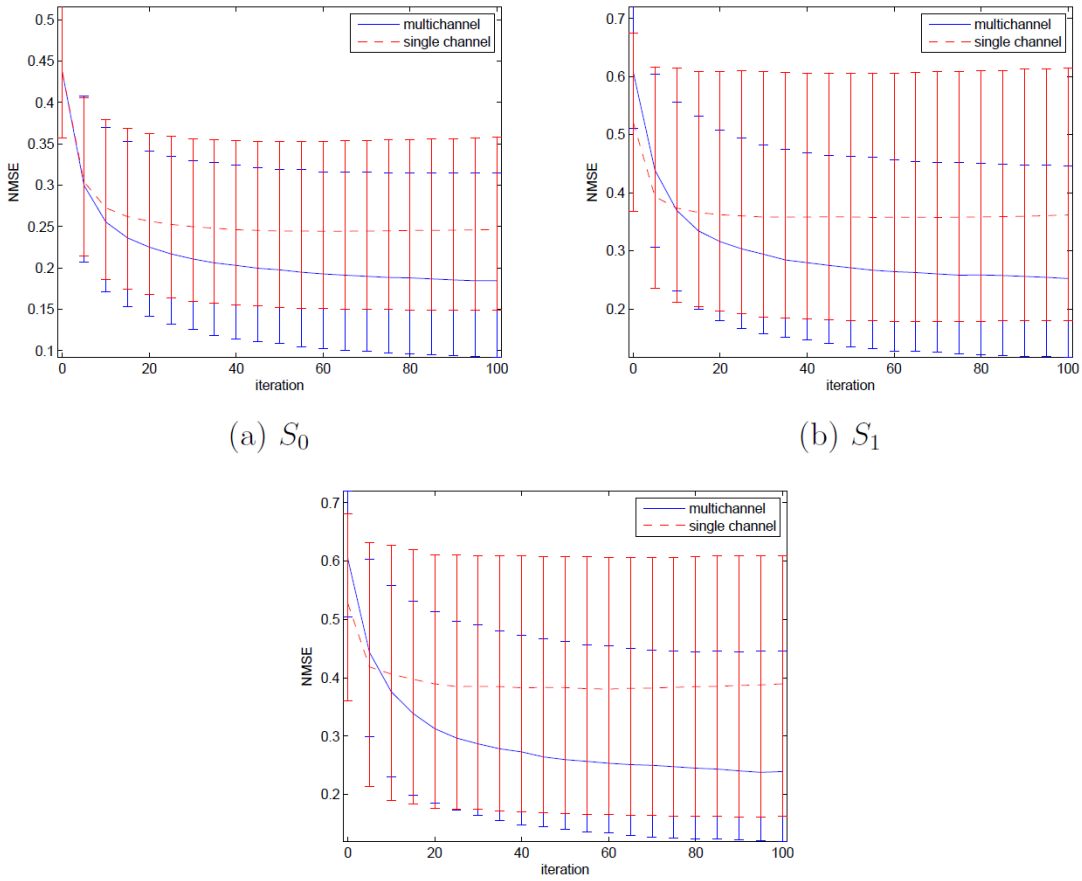

Figure 4: Stokes Parameter Estimations from Multichannel GEM

In order to reconstruct the Stokes vector, *S,* the polarization angle, α, is necessary. $\overline{S}$ can be recomputed as shown below in Equation (2.49) with definitions shown in Equations (2.50) and (2.51) for the unpolarized component of the vector, $\overline{S}_u$, and the polarized component, $\overline{S}_p$, respectively. S_0 is the total light intensity. This gives the ability to use these principles for partially polarized light as well as completely polarized light, as was the case in these experiments. When the light was completely polarized, all elements of $\overline{S}_u$ are equal to 0.

$$\overline{S} = \overline{S}_u + \overline{S}_p \,. \tag{2.49}$$

$$\overline{S}_u = \lambda_u \begin{bmatrix} 1 \\ 0 \\ 0 \\ 0 \end{bmatrix} = (1-P) S_0 \begin{bmatrix} 1 \\ 0 \\ 0 \\ 0 \end{bmatrix}. \tag{2.50}$$

$$\overline{S}_p = \lambda_p \begin{bmatrix} 1 \\ \cos(2\alpha) \\ \sin(2\alpha) \\ 0 \end{bmatrix} = P S_0 \begin{bmatrix} 1 \\ \cos(2\alpha) \\ \sin(2\alpha) \\ 0 \end{bmatrix}. \tag{2.51}$$

Setting $S_3 = 0$ makes the assumption that the circularly polarized component of the light received has an intensity of 0. In natural light, this has been demonstrated to be true [8], however, expanding this method into the circular domain could allow for certain active detection methods to work as well as the passive approaches described here. This would require the illumination of the target with an active, circularly polarized beam and then measuring the effect that the reflection has on the beam.

2.7. Material Classification

Fully identifying a specific material is challenging using only polarimetry. However, classifying certain characteristics, using polarimetry, has been done. Dielectric metallic objects can be identified using the polarization Fresnel ratio [8] [19]. The Fresnel ratio is defined by F in Equation (2.52). $F > 2.0$ is indicative of a dielectric surface, while $F < 2.0$ is indicative of a metallic surface [19]. An example of an image produced with this classification method is shown below in Figure 5 [8]. On the top of the figure is the portion of the image flagged as ‘metallic’ and the bottom of the figure is portion flagged

as ‘dielectric’. In the case of the scissors, the metallic blade is clearly visible on the top and the dielectric handle on the bottom. The spots on the bottom left image are rust spots on the blade that are correctly identified as dielectric. Similarly, with the printed circuit board, the metallic traces are clearly visible in the top image and the dielectric substrate is highlighted in the bottom of the figure.

$$F = \frac{R_{\perp}}{R_{\parallel}}. \tag{2.52}$$

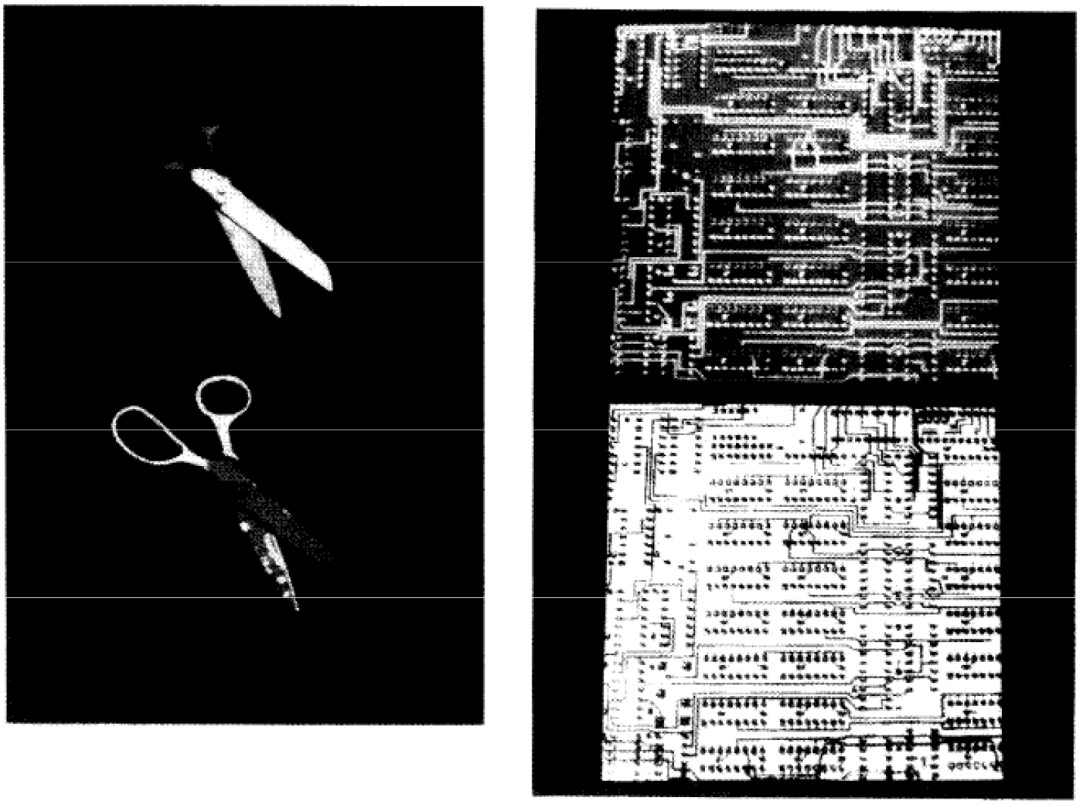

Figure 5: Metallic/Dielectric Polarimetric Classification [8]

Another method that is used to distinguish between metallic and dielectric substances involves a slightly more complex calculation but in essence is looking at the DoLP as described above in Equation (2.19) [20]. It was noted that the DoLP ‘map’

(displayed below in Figure 6) dielectric materials, such as vinyl chloride, demonstrated a convex pattern, and metallic materials, such as copper, displayed a concave pattern. The z-axis is the DoLP and the x and y axes correspond to the pixels in the above photographs. The white dot in the graphs is the estimated point where the center of the light source hits the object.

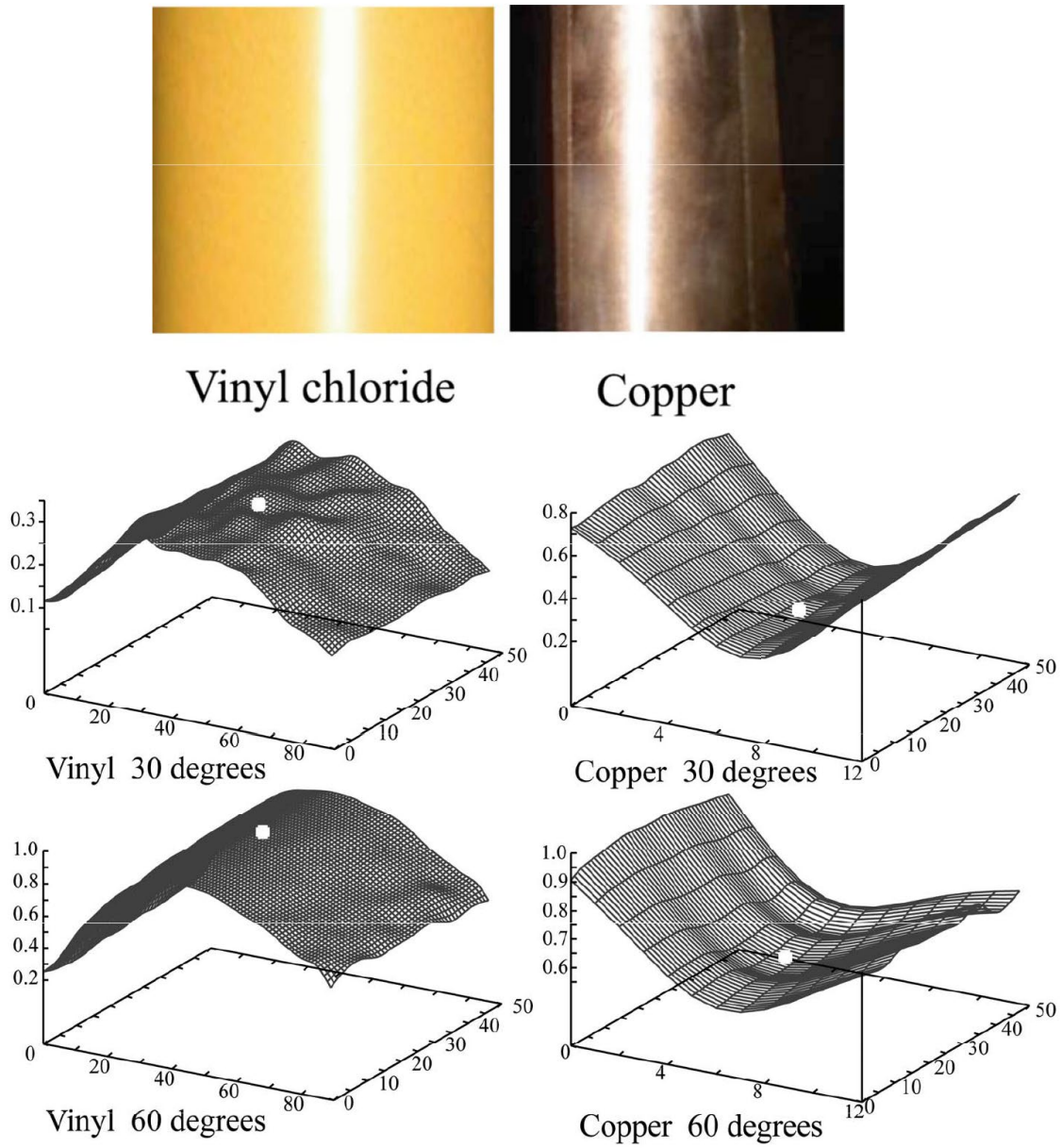

Figure 6: DoP Dielectric/Metallic Map [8]

2.8. Polarimetric Material Classification via GEM

Continuing on the above work, there has been some study into the additional application of GEM to polarimetric material characterization. Dr. Hyde's work shows the potential of identifying predetermined materials via the DoLP of the return light [8]. There

are some limitations to this, however, and only a few sets of materials were examined. By reflecting unpolarized light off of a surface and measuring the return light with a polarimetric imager (shown below in Figure 7) he was able to observe a very strong correlation between the object material type and the DoLP.

In one experiment utilizing this setup, Dr. Hyde used iron and glass samples with different roughness levels (σ) of each. He then varied the angle of incidence, θ_i (and the corresponding angle of reflection, θ_r) to observe the impact σ had on his measurements. The result was that σ had much less of an impact than the actual material index of refraction, which makes material type identification much more manageable. This is shown below in Figure 8. Initially only DoLP is used, but later the complex index of refraction for the material, η, (with real part n and imaginary part κ) at point x, is recovered for greater material discrimination [8].

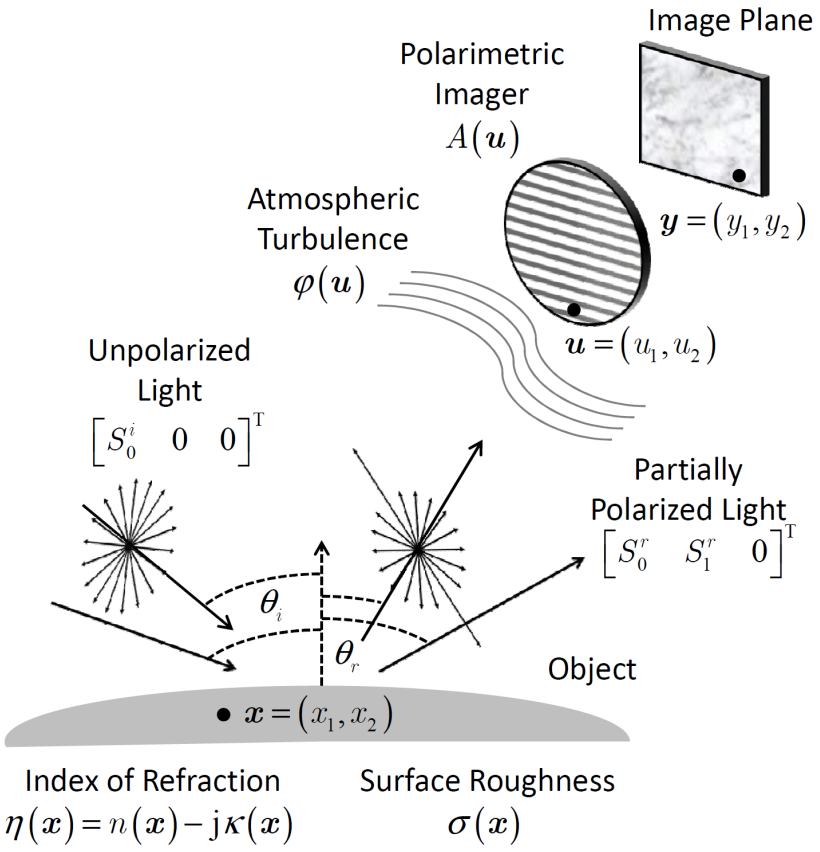

Figure 7: Polarimetric Material Characterization Experiment [8]

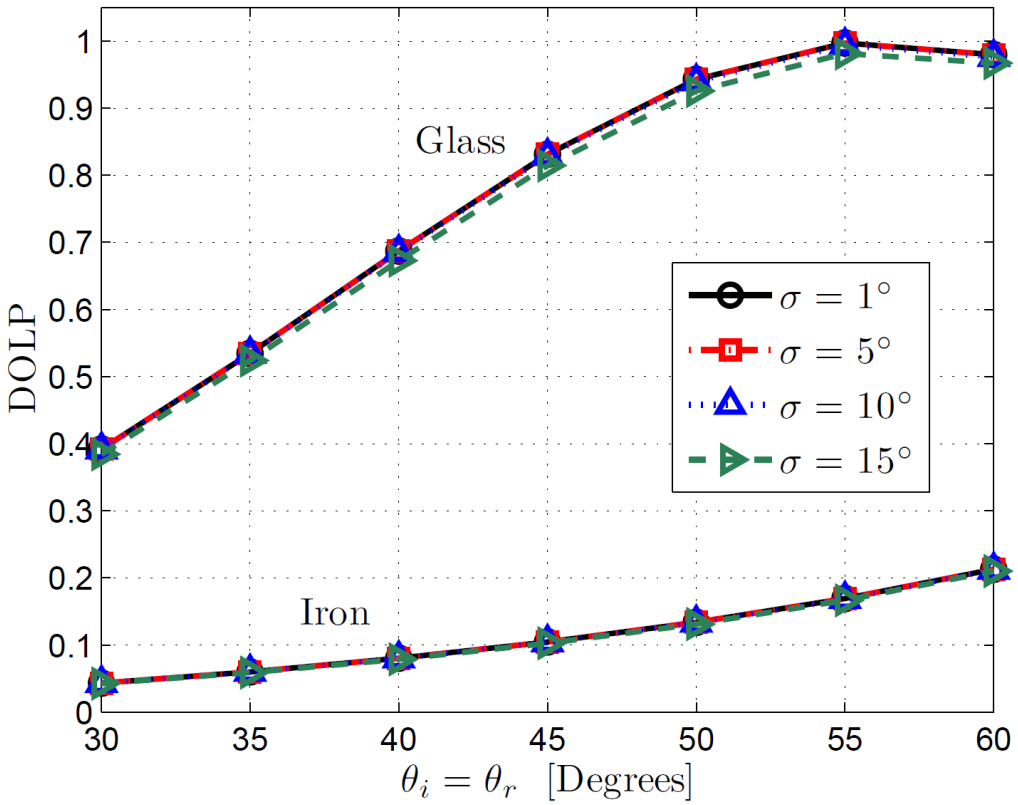

Figure 8: Interpreted Material DoLP [8]

A flowchart of the methodology used by Hyde for the material recovery is shown below in Figure 9. The flowchart represents the i^{th} iteration of the process for the given experiment. The superscript *thy* is for a theoretical number, the superscript *meas* is for a measured number. It is necessary to have prior information about the objects you are attempting to discriminate between in order to set up the initial hypotheses which is potentially problematic for a large database, but when there are only a few material types (dielectric vs metallic) this works well. In the end the experiment was able to recover fairly accurate κ values from the various metals (though the mean values of η are typically not

very close). The results for four different materials, with and without turbulence, and then with correction, are shown below in Figure 10.

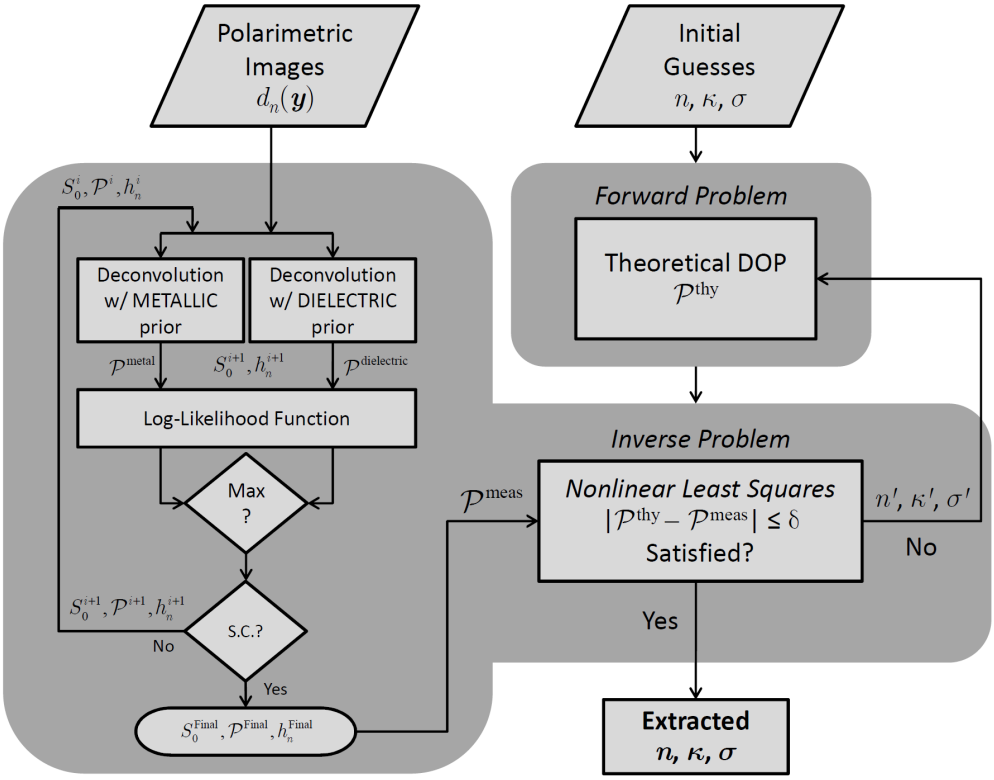

Figure 9: Material Characterization Flowchart [8]

	Aluminum ($n = 1.44$, $\kappa = 16$) Area				Steel ($n = 3.60$, $\kappa = 5.88$) Area			
	$\mathrm{E}[n]$	σ_n	$\mathrm{E}[\kappa]$	σ_κ	$\mathrm{E}[n]$	σ_n	$\mathrm{E}[\kappa]$	σ_κ
No Turb.	3.8614	1.487	11.1757	3.7652	3.8649	1.6921	5.7123	1.6088
Turb. $D/r_0 \approx 7.9$	4.1437	1.1708	11.9855	2.8092	4.4741	1.1529	6.3506	1.0067
Turb. $D/r_0 \approx 12.9$	4.2454	1.0718	12.2713	2.7750	4.8632	0.52165	6.7198	0.59269
Corr. $D/r_0 \approx 7.9$	3.9451	1.2605	11.3748	3.1434	4.6241	1.2863	4.6493	1.3366
Corr. $D/r_0 \approx 12.9$	3.9762	1.0008	11.9791	2.2400	4.8465	0.84901	5.0693	1.0472

	Green Paint ($n = 1.39$, $\kappa = 0.34$) Area				Green Paint ($n = 1.39$, $\kappa = 0.34$) Area			
	$\mathrm{E}[n]$	σ_n	$\mathrm{E}[\kappa]$	σ_κ	$\mathrm{E}[n]$	σ_n	$\mathrm{E}[\kappa]$	σ_κ
No Turb.	2.2467	1.2717	1.4073	1.4859	2.1424	1.1946	1.1951	1.0491
Turb. $D/r_0 \approx 7.9$	2.2420	1.2777	1.5772	1.9564	2.3459	1.2942	1.4020	1.6017
Turb. $D/r_0 \approx 12.9$	2.3074	1.3033	1.8434	2.5221	2.3819	1.3459	1.7714	2.207
Corr. $D/r_0 \approx 7.9$	1.2832	0.30757	0.68629	0.14007	1.3290	0.40899	0.63531	0.22920
Corr. $D/r_0 \approx 12.9$	1.3586	0.49623	0.77617	0.34729	1.3874	0.67263	0.74994	0.65207

Figure 10: Index of Refraction Recovery [8]

2.9. Summary

Polarimetry is commonly used in the characterization of objects. Linear polarization is more commonly used than circular polarization because it occurs naturally and thus lends itself well to passive polarimetric detection schemes. However, circular polarization is becoming increasingly interesting in certain circles and little has been done to characterize it due to its increased complexity as well as the requirement for active sensing. Stokes parameters are a common means of describing the polarization of the intensity of a light wave. A GEM based approach exists for describing a scene via Stokes parameters but only based upon the linear set of parameters. This research intends to expand that approach to include circular polarization as well.

3. Methodology

This chapter begins with a physical description of the system that was tested and simulated. Then it shall discuss the development and adaptation of the existing GEM frame work to this model and how these methods shall incorporate circular polarization. Next it will discuss how this was adapted into MATLAB as well as some variations on that simulation. Lastly, a laboratory experiment will be described to validate the algorithm as well as several variations of the experiment.

3.1. Test Setup

In addition to turbulence, this simulation also involves a polarization filter at the end to enable the collection of the polarimetric state of the data (including the ellipticity). The orientation of this filter will be different for each channel. The differences in orientation will allow for the data to be collected properly. This filter will consist of a waveplate ($\mathbf{M}_{wp}$, which is defined in Equation (3.1)) of retardance ϕ and a linear polarizer ($\mathbf{M}_{D}$). For each channel the waveplate will be rotated to a different angle, θ, to allow differentiation between the channels and to enable the algorithm to function properly. The linear polarizer will remain untouched. This is shown below in Figure 11.

$$\mathbf{M}_{wp}\left(\theta,\phi\right)=\mathbf{M}_{R}\left(\theta\right)\mathbf{M}_{w}\left(\phi\right)\mathbf{M}_{R}\left(-\theta\right). \tag{3.1}$$

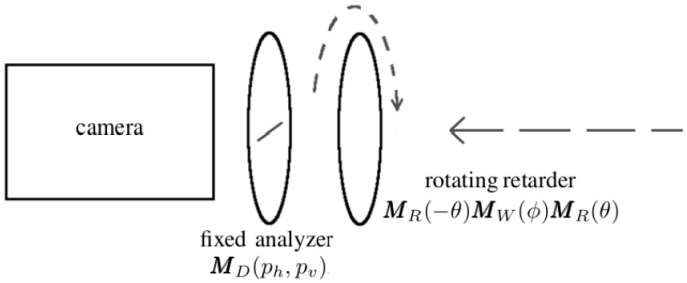

Figure 11: Experimental Setup [21]

The mathematical interpretation of this setup is similar to that performed in [6] except for the addition of the fourth Stokes element. The Mueller matrix is a means of describing the effect that a system has on the light that passes through it. Specifically, this will calculate the polarization state of the light after it passes through. The basic equation is shown below in Equation (3.2) where $\overline{S}_{in}$ is the Stokes vector of the light entering the system, $\mathbf{M}$ is the Mueller matrix of the system, and $\overline{S}_{out}$ is the Stokes vector of the light leaving the filter.

$$\overline{S}_{out} = \mathbf{M}\overline{S}_{in}. \tag{3.2}$$

In this case, there will be two elements to the Mueller matrix. They are the waveplate and the linear polarization filter. The linear filter will be set at an angle of $\theta = 0$ which has a Mueller matrix $\mathbf{M}_D$ shown below in Equation (3.3). The waveplate's Mueller matrix, $\mathbf{M}_{wp}(\theta,\phi)$ is determined by Equation (3.1). $\mathbf{M}_R(\theta)$, which defines the effect rotating an element has on a system, is defined in Equation (3.4) where θ denotes the angle that the waveplate is rotated to, relative to the polarization filter. $\mathbf{M}_w(\phi)$ is the Mueller

matrix for a waveplate, as shown in Equation (3.5) where ϕ denotes the ellipticity (that is, the angular difference between the fast and slow axis) of the plate [21]. Thus, plugging Equations (3.4) and (3.5) into Equation (3.1), $\mathbf{M}_{wp}(\theta,\phi)$ becomes Equation (3.6).

$$\mathbf{M}_D = \begin{bmatrix} 1 & 1 & 0 & 0 \\ 1 & 1 & 0 & 0 \\ 0 & 0 & 0 & 0 \\ 0 & 0 & 0 & 0 \end{bmatrix}. \tag{3.3}$$

$$\mathbf{M}_R(\theta) = \begin{bmatrix} 1 & 0 & 0 & 0 \\ 0 & \cos(2\theta) & \sin(2\theta) & 0 \\ 0 & -\sin(2\theta) & \cos(2\theta) & 0 \\ 0 & 0 & 0 & 1 \end{bmatrix}. \tag{3.4}$$

$$\mathbf{M}_w(\phi) = \begin{bmatrix} 1 & 0 & 0 & 0 \\ 0 & 1 & 0 & 0 \\ 0 & 0 & \cos(\phi) & \sin(\phi) \\ 0 & 0 & -\sin(\phi) & \cos(\phi) \end{bmatrix}. \tag{3.5}$$

$$\mathbf{M}_{wp}(\theta,\phi) = \begin{bmatrix} 1 & 0 & 0 & 0 \\ 0 & \cos^2(2\theta)+\sin^2(2\theta)\cos(\phi) & \cos(2\theta)\sin(2\theta)(1-\cos(\phi)) & \sin(2\theta)\sin(\phi) \\ 0 & \cos(2\theta)\sin(2\theta)(1-\cos(\phi)) & \cos^2(2\theta)\cos(\phi)+\sin^2(2\theta) & -\cos(2\theta)\sin(\phi) \\ 0 & -\sin(2\theta)\sin(\phi) & \cos(2\theta)\sin(\phi) & \cos(\phi) \end{bmatrix}. \tag{3.6}$$

In Mueller calculus, the multiplication sequence is from left to right. That is, the last element that the light passes through, then the first, then the original Stokes vector to get the outgoing Stokes vector. Thus, the full equation begins with the linear polarizer (the last element) is followed by the waveplate, and ends with the input light, as shown below in Equation (3.7) [21].

$$\overline{S}_{out} = \mathbf{M}_D \mathbf{M}_{wp} \overline{S}_{in} . \tag{3.7}$$

It is important to note that the detector will only be able to read the total intensity, not the entire Stokes vector. After multiplying through the elements in Equation (3.7), the total intensity, $\overline{S}_{0,in}$ for a given system is shown in Equation (3.8) below and $\overline{W}_c$ consists of the elements of the Mueller matrix that are used to calculate $\overline{S}_{0,in}$ for that channel. The subscript *c* indicates the variables that vary by channel.

$$\overline{S}_{0c,out} = \overline{W}_c \overline{S}_{c,in} = \begin{bmatrix} 1 \\ \cos^2(2\theta_c) + \cos(\phi_c)\sin^2(2\theta_c) \\ (1-\cos(\phi_c))\cos(2\theta_c)\sin(2\theta_c) \\ -\sin(\phi_c)\sin(2\theta_c) \end{bmatrix}^T \begin{bmatrix} S_{0c,in} \\ S_{1c,in} \\ S_{2c,in} \\ S_{3c,in} \end{bmatrix}. \tag{3.8}$$

There will be four different elements needed in the output (effectively the four elements of the Stokes vector), meaning that there will be four channels needed for the experiment. Therefore, in the end, $\mathbf{W}$ will be a 4x4 matrix. Selecting the angles needed for these channels is a matter of minimizing Stokes readout error for the overall system. The intensity seen by the camera will actually add a noise vector, $\overline{n}$, to Equation (3.8) , causing the light intensity read by the camera to become Equation (3.9).

$$\overline{I}_{camera} = \mathbf{W}(\overline{S}_{in} + \overline{n}) . \tag{3.9}$$

To find an estimate of $\overline{S}_{in}$ without knowing $\overline{n}$, the pseudoinverse of $\mathbf{W}$ is taken [22]. Here, the pseudoinverse is the same as the inverse if the inverse exists, and results in the minimum norm, least square error reconstruction otherwise (as would the case when

there are fewer than four channels for instance). This pseudoinverse is defined as κ and is known as the condition number [23]. The original Stokes vector is then computed by Equation (3.11) where $\hat{\bar{S}}_{in}$ is the reconstructed estimate.

$$\kappa = \left\|\mathbf{W}\right\|\left\|\mathbf{W}^{-1}\right\|. \tag{3.10}$$

$$\hat{\bar{S}}_{in} = \kappa \bar{I}_{camera}\,. \tag{3.11}$$

There will be an error in this reconstruction, $\Delta\bar{S}$, based on the pseudoinverse and the noise. Substitution of $\bar{I}_{camera}$ from Equation (3.11) into Equation (3.9) yields Equation (3.12), which shows that minimizing κ will minimize the error in the Stokes vector recreation [22].

$$\bar{S}_{in} - \hat{\bar{S}}_{in} = \Delta\bar{S} = \kappa\bar{n}\,. \tag{3.12}$$

In prior work, S_0, S_1, and S_2 were calculated, which allowed for only three channels of different angles [2]. In this case, the angles needed across the four channels to reach the minimum condition value for the four Stokes element case is given by the following vectors, where Channel *c* would consist of a waveplate of ellipticity ϕ_c which is rotated to an angle of θ_c relative to the horizontal, and then followed by a horizontal polarization filter [23]. The minimum κ will minimize the error sensitivity of the total system. This minimum is achieved at the ϕ_c and θ_c values listed below in Equations (3.13) and (3.14) [21] [23] [22]. These angles were chosen to optimize SNR. Optimizing the SNR of the incomplete data gives the best inputs into the log likelihood equation. Giving the algorithm a noisy signal would make it more difficult to reconstruct the original target.

Additionally, the choice of these angles, by minimizing κ, allows decoupling of variables later on in the GEM algorithm development.

$$\phi = \begin{bmatrix} 132 \\ 132 \\ 132 \\ 132 \end{bmatrix}. \tag{3.13}$$

$$\theta = \begin{bmatrix} -51.69 \\ -15.12 \\ 15.12 \\ 51.69 \end{bmatrix}. \tag{3.14}$$

After inserting Equations (3.13) and (3.14) into the partial Mueller matrix in Equation (3.6), we have a new transfer matrix, $\mathbf{W}$, shown below in Equation (3.15). This is not a Mueller matrix, but will function in a similar manner, mathematically. Inserting $\mathbf{W}$ back into Equation (3.2) shows how the system will effect each of the different channels based upon the inputs received, where d_c is the data received for a particular channel, c.

$$\mathbf{W} = \begin{bmatrix} 0.50 & -0.29 & 0.19 & 0.36 \\ 0.50 & 0.29 & -0.36 & 0.19 \\ 0.50 & 0.29 & 0.36 & -0.19 \\ 0.50 & -0.29 & -0.19 & -0.36 \end{bmatrix}. \tag{3.15}$$

$$\begin{bmatrix} d_1 \\ d_2 \\ d_3 \\ d_4 \end{bmatrix} = \mathbf{W} \begin{bmatrix} S_{0,in} \\ S_{1,in} \\ S_{2,in} \\ S_{3,in} \end{bmatrix}. \tag{3.16}$$

Thus, to go back from the data to the Stokes vector at the polarimeter you would multiply the data vector by the inverse of $\mathbf{W}$ matrix, or $\mathbf{W}^{-1}$.

As with [2], converting the Stokes vector into its polarized intensity and unpolarized intensity splits the data into two Poisson variables which can feed into the existing GEM. The Stokes components at that point are given by Equation (3.17).

$$\begin{aligned} S_0 &= I \\ S_1 &= PS_0 \cos(2\chi)\cos(2\alpha) \\ S_2 &= PS_0 \cos(2\chi)\sin(2\alpha) \\ S_3 &= PS_0 \sin(2\chi) \end{aligned}. \tag{3.17}$$

P is the Degree of Polarization and I is the total intensity that reaches the receiver. χ is the ellipticity of the light and α is the polarization angle of the light. The unpolarized portion of the Stokes vector, which only concerns the top component is shown as $\overline{S}_u$ in Equation (3.18) and the polarized component as $\overline{S}_p$ in Equation (3.19).

$$\overline{S}_u = (1-P)S_0 \begin{bmatrix} 1 \\ 0 \\ 0 \\ 0 \end{bmatrix}. \tag{3.18}$$

$$\overline{S}_p = PS_0 \begin{bmatrix} 1 \\ \cos(2\chi)\cos(2\alpha) \\ \cos(2\chi)\sin(2\alpha) \\ \sin(2\chi) \end{bmatrix}. \tag{3.19}$$

Measured through the system of polarization analyzers described above in Equation (3.8) the resulting intensity is shown in Equation (3.20).

$$I(\phi_c,\theta_c)=\frac{1}{2}\begin{pmatrix} S_0+S_1\left(\cos(2\theta_c)^2+\sin(2\theta_c)^2\cos(\phi_c)\right) \\ +S_2\left(\left(1-\cos(\phi_c)\right)\left(\cos(2\theta_c)\sin(2\theta_c)\right)\right) \\ -S_3\sin(2\theta_c)\sin(\phi_c) \end{pmatrix} \tag{3.20}$$

The fully polarized component, λ_p, is shown below in Equation (3.21) . Similarly, the unpolarized component, λ_u, is shown below in Equation (3.22).

$$\lambda_p = PS_0 \tag{3.21}$$

$$\lambda_u = (1-P)S_0 \tag{3.22}$$

Thus the total intensity, found by substituting Equations (3.22) and (3.21) into Equation (3.20) is shown below in Equation (3.23). For the sake of simplification, $T(\chi,\alpha,\theta_c,\phi_c)$ is defined in Equation (3.24).

$$I(\phi_c,\theta_c)=\frac{1}{2}(1-P)S_0+\frac{1}{2}PS_0T(\chi,\alpha,\theta_c,\phi_c)=\frac{1}{2}\lambda_u+\lambda_pT(\chi,\alpha,\theta_c,\phi_c). \tag{3.23}$$

$$T(\chi,\alpha,\theta_c,\phi_c)=\frac{1}{2}\begin{pmatrix} 1+\left(\cos(2\chi)\cos(2\alpha)\right)\left(\cos(2\theta_c)^2+\sin(2\theta_c)^2\cos(\phi_c)\right) \\ +\left(\cos(2\chi)\sin(2\alpha)\right)\left(\left(1-\cos(\phi_c)\right)\left(\cos(2\theta_c)\sin(2\theta_c)\right)\right) \\ -\left(\sin(2\chi)\right)\left(\sin(2\theta_c)\sin(\phi_c)\right) \end{pmatrix}. \tag{3.24}$$

3.2. GEM Integration

3.2.1. Expectation Step

As described in section 2.5.2, the Expectation step defines the objective function that is being maximized. Unlike the three Stokes case described in section 2.5, the parameters of interest here are λ_u, λ_p, h, α, and χ. Equation (3.25) defines the object function as a sum of the unpolarized and polarized components. The incomplete data, because it receives both polarized and unpolarized light from a given channel, becomes Equation (3.26). The expectation function for the unpolarized and polarized components, for a given channel and *x,y* pair are shown below in Equations (3.27) and (3.28). As before, *o* is the object function, and *i*, the image function, which is the same as the mean of *d*. The subscript *c*, as well as the *c* in the summation, denotes a specific channel which will correspond with a specific ϕ and θ.

$$o_c(x) = \frac{1}{2}\lambda_u(x) + \lambda_p(x)T(\chi, \alpha, \theta_c, \phi_c). \tag{3.25}$$

$$d_c(y) = \sum_x D_{uc}(y,x) + \sum_x D_{pc}(y,x). \tag{3.26}$$

$$E\left[D_{uc}(y,x)\right] = \frac{1}{2}\lambda_u(x)h_c(y-x). \tag{3.27}$$

$$E\left[D_{pc}(y,x)\right] = \lambda_p(x)T(\chi, \alpha, \theta_c, \phi_c)h_c(y-x). \tag{3.28}$$

The objective function is defined below in Equation (3.29), where L is the log likelihood of the data. While this last term is derived more thoroughly in [2] , it is shown below in Equation (3.30). Now that the log likelihood for the system has been defined, the angles

selected previously can be verified via a Cramer Rao Lower Bound (CRLB). The method by which this was done is described in Appendix A.

$$Q^{n+1}\left(\lambda_u,\lambda_p,h,\alpha\right)=E\left[L\left(\lambda_u,\lambda_p,h,\alpha\right)\mid d,\lambda_u{}^n,\lambda_p{}^n,h^n,\alpha^n\right] \tag{3.29}$$

$$\begin{aligned}L\left(\lambda_u,\lambda_p,h,\alpha\right)&=\sum_x\sum_y\sum_c\left\{D_{uc}\left(y,x\right)\ln\left[\frac{1}{2}\lambda_u\left(x\right)h_c\left(y-x\right)\right]-\frac{1}{2}\lambda_u\left(x\right)h_c\left(y-x\right)\right\}\\&+\sum_x\sum_y\sum_c\left\{D_{pc}\left(y,x\right)\ln\left[\lambda_p\left(x\right)h_c\left(y-x\right)T\left(\chi,\alpha,\theta_c,\phi_c\right)\right]-\lambda_p\left(x\right)h_c\left(y-x\right)T\left(\chi,\alpha,\theta_c,\phi_c\right)\right\}\end{aligned} \tag{3.30}$$

The expectation value itself is defined as $\psi_{kc}^{n+1}\left(y,x\right)$ in Equation (3.31) where the subscript *k* is either *u* for unpolarized data or *p* for a polarized data. The results for the *u* and *p* portions of the conditional expectation value may be found by referencing back to Equations (3.27) and (3.28) [2].

$$\psi_{kc}^{n+1}\left(y,x\right)=E\left[D_{kc}\left(y,x\right)\mid d_c,\lambda_k^n,\alpha^n,h_c^n\right] \tag{3.31}$$

$\psi_{pc}^{n+1}\left(y,x\right)$ is more complicated than it was for the linear case but $\psi_{uc}^{n+1}\left(y,x\right)$ is unchanged. Because λ_{uc} and λ_{pc} are each Poisson, and the collected data consists of their sum (for a given channel) their expectation can be shown in Equation (3.32) where i_c is the mean value of the total intensity for channel *c* [24].

$$E\left[\lambda_{kc}\middle|\lambda_{uc}+\lambda_{pc}\right]=\frac{\left(\lambda_{uc}+\lambda_{pc}\right)\overline{\lambda_{kc}}}{\overline{\lambda_{uc}}+\overline{\lambda_{pc}}}=\frac{d_c}{i_c}\overline{\lambda_{kc}}\,. \tag{3.32}$$

Equations (3.21) and (3.22) show the respective λ_{kc} values for each given pixel, *x*. $\psi_{uc}^{n+1}\left(y,x\right)$ and $\psi_{pc}^{n+1}\left(y,x\right)$ become what is shown below in Equations (3.33) and (3.34) respectively.

$$\psi_{uc}^{n+1}(y,x)=\frac{1}{2}\frac{d_c^n(y)}{i_c^n(y)}\lambda_u^n(x)h_c^n(y-x). \tag{3.33}$$

$$\psi_{pc}^{n+1}(y,x)=\frac{d_c^n(y)}{i_c^n(y)}\lambda_p^n(x)h_c^n(y-x)T(\chi,\alpha,\theta_c,\phi_c). \tag{3.34}$$

3.2.2. Maximization Step

Next, the derivative of Q^{n+1} was taken with respect to the various parameters of interest listed and set the result equal to 0 for each pixel, x_0. For example, looking at λ_p or λ_u yields Equations (3.35), or (3.36) respectively.

$$\frac{dQ^{n+1}}{d\lambda_p(x_0)}=\sum_y\sum_c\left[\frac{\psi_{pc}^{n+1}(y,x_0)}{\lambda_p(x_0)}\right]-\sum_c\left[T(\chi,\alpha,\theta_c,\phi_c)\right]\equiv 0. \tag{3.35}$$

$$\frac{dQ^{n+1}}{d\lambda_u(x_0)}=\sum_y\sum_c\left[\frac{\psi_{uc}^{n+1}(y,x_0)}{\lambda_u(x_0)}\right]-\frac{C}{2}\equiv 0. \tag{3.36}$$

As with the three Stokes case, the specific values of θ_c and ϕ_c selected in Equations (3.13) and (3.14), the $\sum_c\left[T(\chi,\alpha,\theta_c,\phi_c)\right]$ in Equation (3.35) simplifies to 2 for all combinations of α and χ when you sum across all channels. This allows Equation (3.35) to simplify Equation (3.37).

$$\frac{dQ^{n+1}}{d\lambda_p(x_0)} = \sum_y \sum_c \left[\frac{\psi_{pc}^{n+1}(y, x_0)}{\lambda_p(x_0)} \right] - 2 \equiv 0 . \tag{3.37}$$

Because C=4, Equation (3.37) can be rewritten as Equation (3.38) putting it in a similar form to Equation (3.36).

$$\frac{dQ^{n+1}}{d\lambda_p(x_0)} = \sum_y \sum_c \left[\frac{\psi_{pc}^{n+1}(y, x_0)}{\lambda_p(x_0)} \right] - \frac{C}{2} \equiv 0 . \tag{3.38}$$

Equations (3.36) and (3.38) can now be generalized as Equation (3.39) [2] .

$$\begin{aligned}
&\frac{dQ^{n+1}}{d\lambda_k(x)} = \sum_y \sum_c \left[\frac{\psi_{kc}^{n+1}(y, x)}{\lambda_k^{n+1}(x)} \right] - \frac{C}{2} = 0 \\
&\frac{C}{2} = \sum_y \sum_c \left[\frac{\psi_{kc}^{n+1}(y, x)}{\lambda_k^{n+1}(x)} \right] \\
&\frac{\lambda_k^{n+1}(x) C}{2} = \sum_y \sum_c \left[\psi_{pc}^{n+1}(y, x) \right] \\
&\lambda_k^{n+1}(x) = \frac{2}{C} \sum_y \sum_c \left[\psi_{kc}^{n+1}(y, x) \right]
\end{aligned} \quad . \tag{3.39}$$

Following the similar steps in Eq 3.35 and 3.36, estimating the unknown parameters α and χ was expected to be found by maximizing the log-likelihood function with respect to the parameter. This is worked out in Appendix A and B. Unfortunately, due to the coupling of parameters, the angles could not be isolated in the same manner as the other parameters. To alleviate this problem, an intuitive solution was proposed that involve the creation of a polarized Stokes vector (similar to $\overline{S}_p$ in Equation (3.19)) for each pixel, x_0 , from the existing polarization angle estimates ($a^n(x_0)$ and $\chi^n(x_0)$) as well as $\lambda_p^{n+1}(x_0)$. The unpolarized component is omitted because it does not contribute to the polarization

angle. This Stokes vector, $\overline{S}^{n+1}$ can then be used to calculate the angle of linear polarization, $a^{n+1}(x_0)$ via Equation (3.40) [2] as well as the next estimate of the ellipticity, $\chi^{n+1}(x_0)$, via (3.41).

$$\alpha^{n+1}(x_0) = \frac{1}{2}\tan^{-1}\left(\frac{S_2^{n+1}(x_0)}{S_1^{n+1}(x_0)}\right). \tag{3.40}$$

$$\chi^{n+1}(x_0) = \frac{1}{2}\tan^{-1}\left(\frac{S_3^{n+1}(x_0)}{\sqrt{\left(S_1^{n+1}(x_0)\right)^2 + \left(S_2^{n+1}(x_0)\right)^2}}\right). \tag{3.41}$$

The only piece remaining is the PSF, $h_c(y-x)$. As seen in Equation (2.6) the PSF consists of a pupil function and a phase. The pupil function is already known, based upon the camera, leaving the phase to be estimated. This estimation is done using the Gerchberg–Saxton (GS) phase retrieval algorithm, just as it had been in prior work [25] [6].

3.2.3. Algorithm Pseudocode

An intuitive way to express how the different functions operate together is to display it as pseudocode. The entire algorithm is run 1000 times for each simulation, thus there are 1000 total iterations of the update functions. However within each of these 1000 iterations, the GS phase retrieval algorithm is run to 25 times before selecting the updated phase angle. So, the update algorithm for a given pixel, might have a pseudocode resembling:

A.) For iteration = 1:1000

1.) Calculate λ_u^{n+1} from Equation (3.39).
2.) Calculate λ_p^{n+1} from Equation (3.39).

3.) Calculate Stokes vector estimate, $\overline{S}^{n+1}$, using the $\mathbf{W}^{-1}$ as well as λ_p^{n+1}, α^n, and χ^n.
4.) Calculate α^{n+1} using Equation (3.40).
5.) Calculate χ^{n+1} using Equation (3.41).
6.) For each channel, c, calculate h_c^{n+1} by estimating the phase angle
    a. For j=1 to 25
        i. Run the GS phase retrieval algorithm to estimate the phase angle for this channel, $\widetilde{\varphi}_c$, for the atmospheric effect of the PSF.
    b. $\varphi_c^{n+1} = \widetilde{\varphi}_c$, which is plugged into (2.6) to give h_c^{n+1} for each channel
    c. End
7.) End

B.) End

The output of the above pseudocode will be the updated estimates for h_c for each channel, as well as λ_p, λ_u, α, and χ for the original target.

3.3. MATLAB Simulation

A polarized target was simulated in MATLAB (shown below in Figure 12) containing the letters A, F, I, and T. The A is polarized to $\alpha = 60°$, χ=0°. This mostly removes the A from channel 2. The F is polarized to $\alpha = -64.2°$, χ=0°. This mostly removes F from the image produced by channel 3. This will become relevant when channel 3 is 'cleaned' because the image output of channel 3 then looks clear but is missing the F. The I is polarized at $\alpha = 45°$, χ=0°. The T is the circularly polarized component with polarization angles of $\alpha = 0$, χ=45°. This is detailed in Table 4.

This target was passed through a randomly generated PSF for each channel. During the simulated trials, a r_o of 0.1 m was used and 100 Zernike polynomials were calculated. The four resulting images are each passed through a different channel. These channels are differentiated by the angle of the waveplate, θ_c, as shown above in Equation (3.14). This creates the four images shown below in Figure 13. The Poisson noise that describes the random photon arrival to the sensor was then simulated via a Poisson random number generator within MATLAB. These four images then became the input data for each channel, or d_c. Each letter in the image was polarized to a different angle such that each channel had one letter that was virtually invisible, as can be seen in Figure 13. The 'T' was circularly polarized. The aperture diameter was set to be 1 meter.

Figure 12: Object

Table 4: Polarization States of Simulated Data

Letter	**α**	**χ**
A	60	0
F	-64.2	0
I	45	0
T	0	45

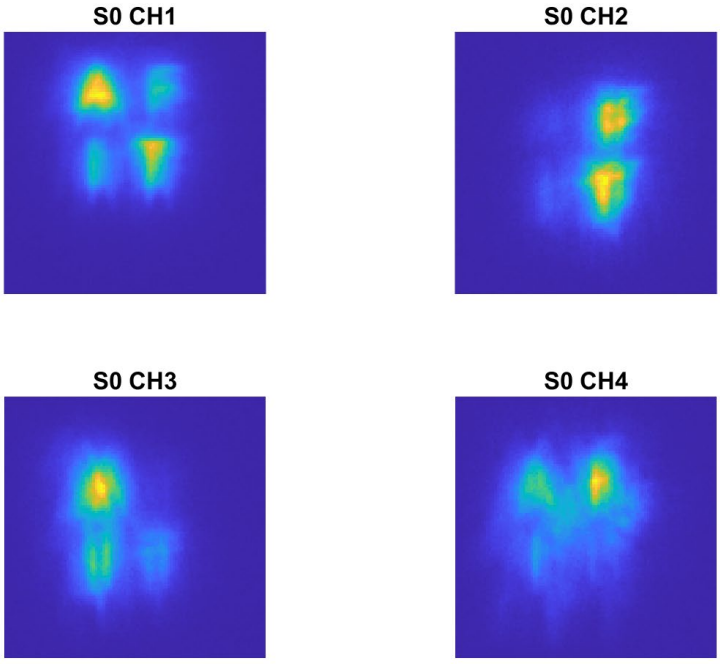

Figure 13: Data With Turbulence

After the data was created, it was sent to a separate program, along with information about the angles of the waveplate. That second program executed the GEM based blind deconvolution algorithm described above. It then output an estimated λ_u, λ_p, α, and χ for each pixel in the object plane, in an effort to recreate the target. The program also made estimations of the PSF, per the GS algorithm which it also exported for comparison with the original PSFs.

3.4. Variations

Additionally, several variations of this simulation were performed to compare the results. In the first, the effects of atmospheric turbulence were removed by setting $r_o = D = 1$ meter to verify the algorithm's functionality in that condition. Next, the

algorithm was applied to a known PSF (r_o = 0.1 meter). This essentially made it a deconvolution algorithm instead of a blind deconvolution algorithm. Third, the simulation was repeated with one turbulence free PSF ($r_o = D$) and three 'normal' channels (r_o = 0.1 meter). This third simulation, with three 'normal' channels and one turbulence free channel most closely resembles the earlier work performed in [6]. Then, the simulation was repeated with an initial guess consisting only of the PSF of the lens to demonstrate how much of a role the initial guess plays in the overall result.

Lastly, simulations were run at different retardances to simulate varying the retardance of the waveplate. This was done to see how far from the ideal 132º retardance a reasonable result could be produced because quarter waveplates (with a 90º retardance) are far more readily available than those waveplates with the desired retardance.

For the $r_o = D$ case, Figure 14 shows what the intensity data looked like for one of the trials and for the simulation. Figure 15 shows an example of what the intensity data looked like for each of the channels in one trial where three of the channels were 'normal' and one had no atmospheric turbulence. For all of the other variations (where all four channels had 'normal' PSFs), the intensity at the receiver used the same parameters as those seen in Figure 13.

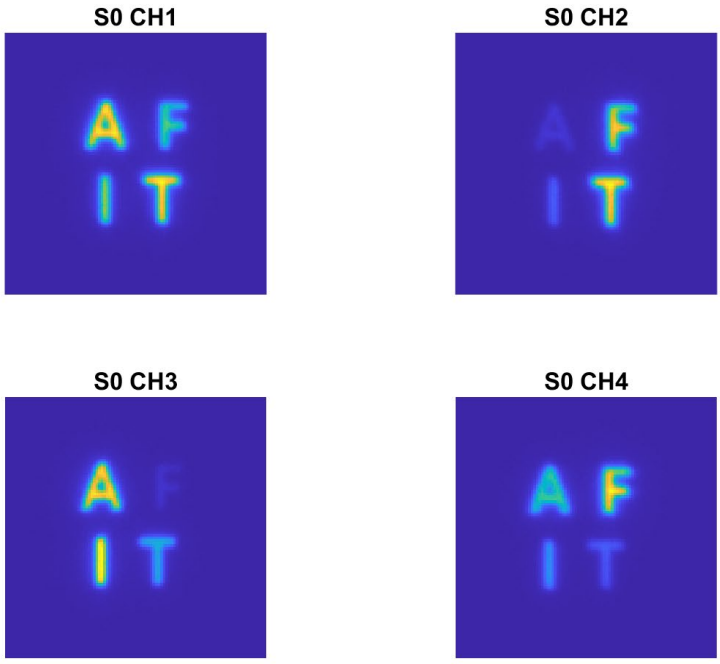

Figure 14: Turbulence Free Data

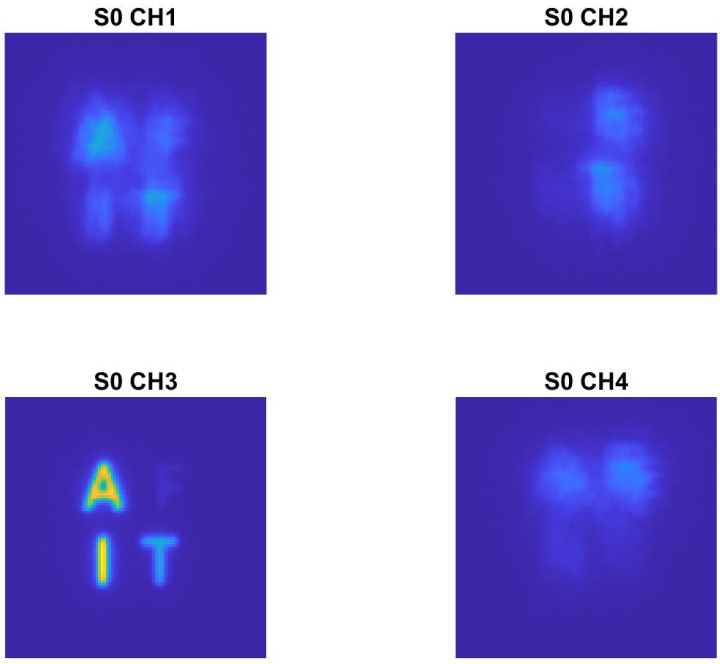

Figure 15: Data With One Turbulence Free Channel

3.5. Laboratory Experiment

To begin the simulation, a fiberoptic broadband light source was connected to a narrow bandpass filter centered at 1550 nm. In order for the waveplate to have the appropriate retardance for all of the measured light, it is necessary for that light to be of about the same wavelength. Next, the light in the fiberoptic line was linearly polarized to 45º then passed through a quarter waveplate which was rotated to an angle of 23.5º ($\pi/8$ radians) relative to the same frame as the linear light. This produced the source light with an ellipticity of 45º.

This source light passes through a polarization filter, then a 125 mm focal length lens before reaching the CCD array. The camera used was a Goldeye G-033 TECless which has a pixel pitch of 15 microns. The overall magnification of the system was approximately 2.5. The polarization filter consists of a Variable Retardance Waveplate (VRW) which was tuned to 132º retardance at 1550 nm followed by a horizontally oriented linear polarizer (denoted with LP in Figure 16). The VRW was a Thorlabs LC-1111T-C. The ideal temperature for achieving a retardance of 132º is 25º C and a voltage of 1.22 VRMS is applied to it. The light source is 290 mm from the lens which is 220 mm from the CCD array to place the target in focus of the CCD array. This is shown visually in Figure 16. The data that was produced is shown below in Figure 17. The light source was a fiberoptic element approximately 10 microns on a side which will cause it to appear as a point source, much like an object in geostationary orbit would to an Earthbound telescope. While this involves measuring light from a source, instead of light reflecting off of an

object, the algorithm itself simply calculates the Stokes vector of the arriving light and so is still capable of recreating the image of the source.

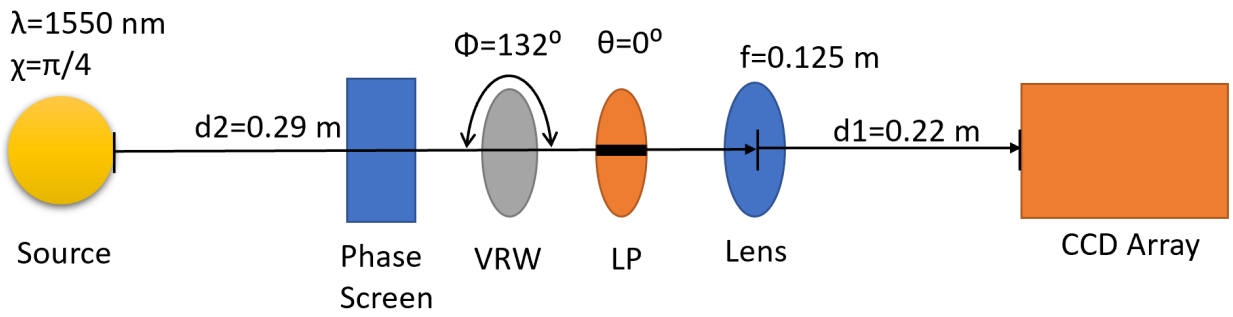

Figure 16: Experimental Setup

The VRW was rotated to -51° from horizontal, and a plastic film was placed over the polarization filter to simulate turbulence blurring the image primarily along the y-axis. Then the waveplate was rotated to -15° from horizontal, and the film was stretched to blur it along the y axis. A second image was taken in this state. Afterwards, the waveplate was rotated to 15° from horizontal and the film was removed. A third image was taken. Finally, the waveplate was rotated to 51° from horizontal and the film was stretched in the x-y axis to produce turbulence at a 45° angle to maximize the diversity between the different point spread functions. The fourth and final picture was taken in this state. The linear polarizer remained horizontal throughout the experiment. The resulting intensity from each channel is shown below in Figure 17.

Afterwards, the quarter waveplate was replaced with a linear polarizer (rotated to 90°) to produce linearly polarized light at a specific angle. This gave the algorithm a chance to verify that it would not incorrectly classify a linearly polarized source as circularly

polarized by assigning a nonzero χ. The process of producing a phase screen was repeated and the intensity results are shown below in Figure 18.

Next, a variation of this setup was then used to create multiple sources. To do this, a splitter was inserted into the fiberoptic line to split the light equally in each line. The end of the first line matched that of the first experiment, with elliptically polarized source light. The second line produced a source matching the second experiment, with linearly polarized light at 90º. The purpose of this was to show that the algorithm can differentiate between two sources of different polarization types. A photo of this setup is shown below in Figure 19. Turbulence was added in the same manner as the previous two scenarios and the data was inserted into the algorithm. The initial data is shown below in Figure 20. Finally, the point sources were replaced with a bar. This consisted of a back illuminated 150 micron slit placed where the previous source had been. The light was elliptically polarized at $\chi = 45°$. This time, turbulence was created in each channel by the plastic film, and the film was stretched in a different direction in each channel. This allows testing of the blind deconvolution portion of the algorithm. The channel inputs are seen below in Figure 21.

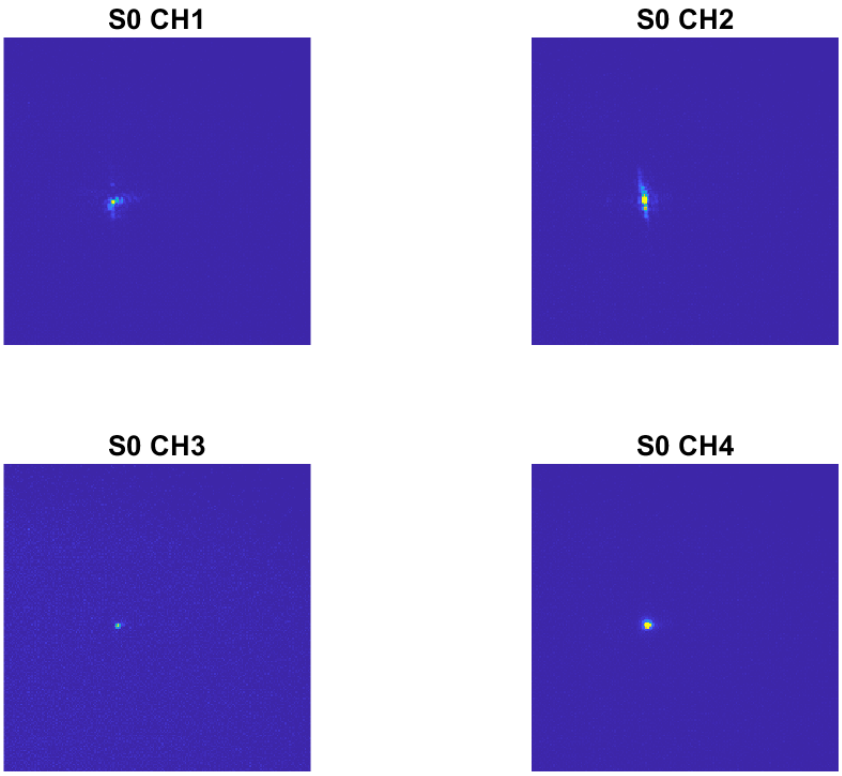

Figure 17: Circularly Polarized Sample With Turbulence

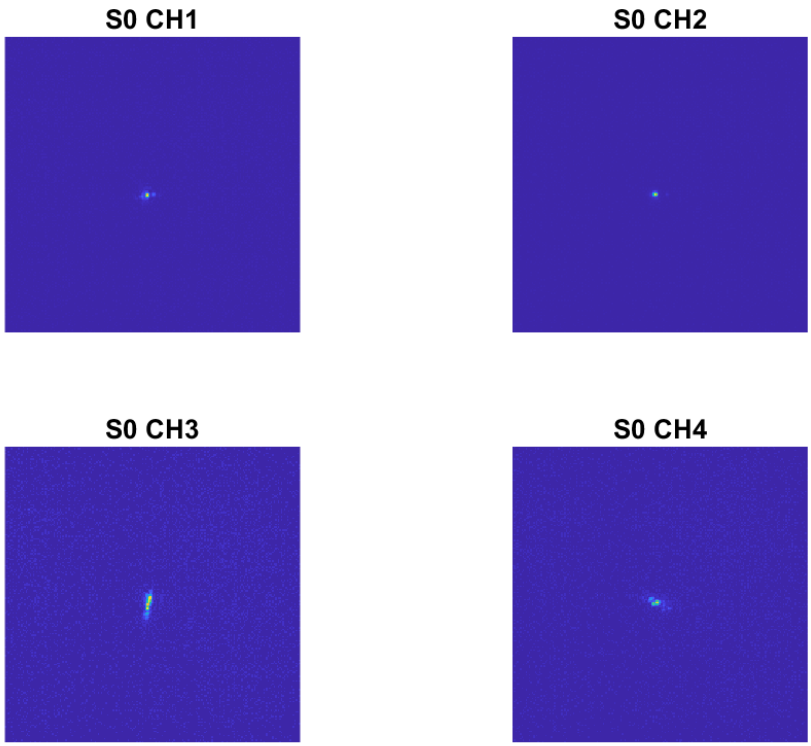

Figure 18: Linearly Polarized Sample With Turbulence

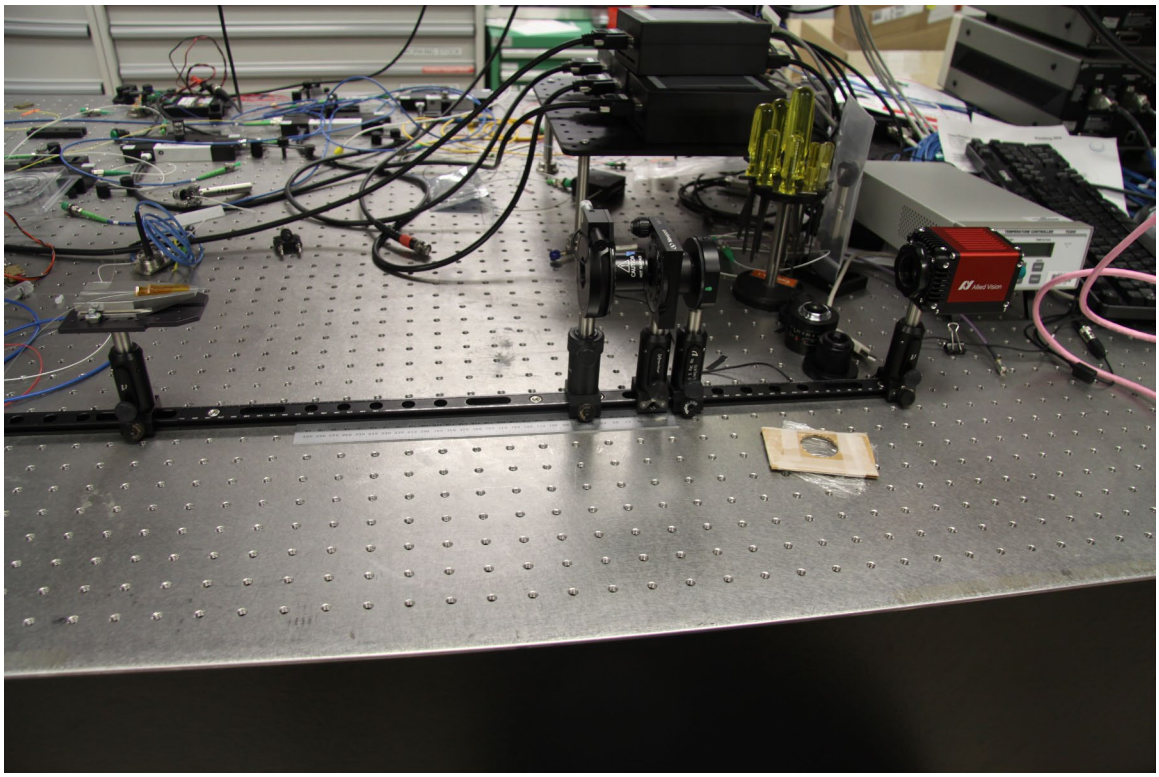

Figure 19: Laboratory Setup Photo

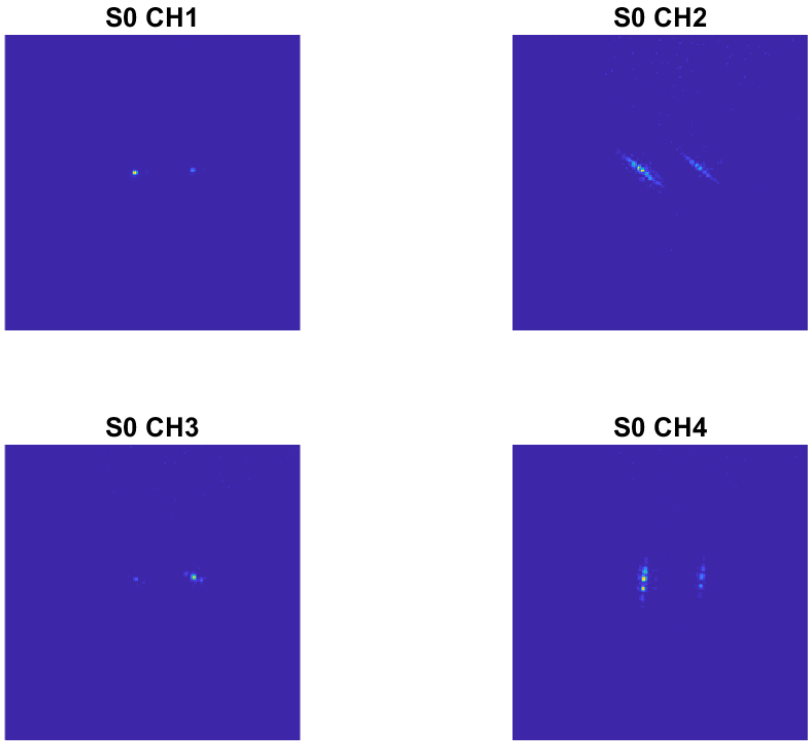

Figure 20: Experimental Data Sample with a Linear and a Circular Source

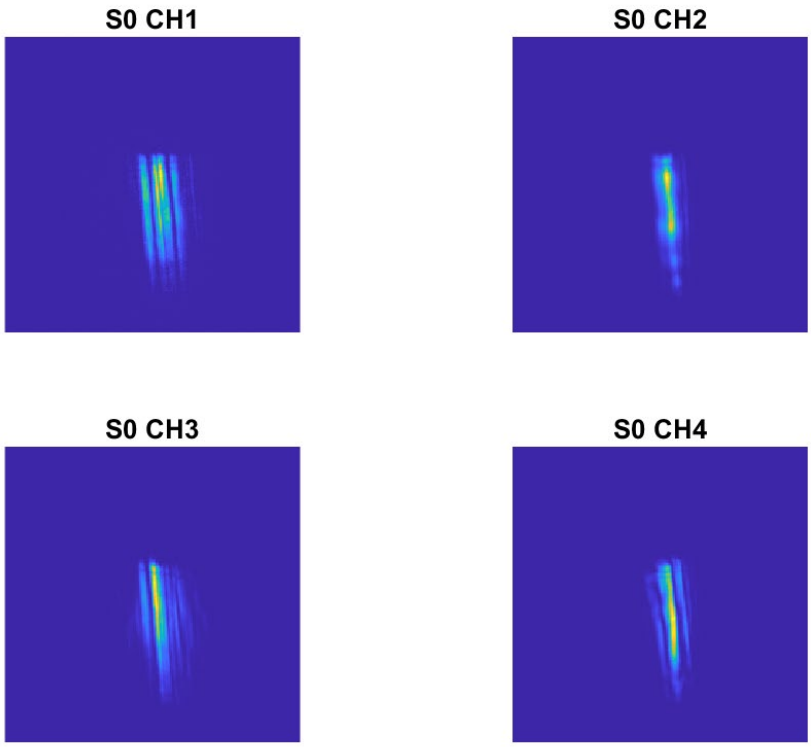

Figure 21: Experimental Data with an Elliptically Polarized Bar Source

4. Results

4.1. Chapter Overview

This chapter will cover the results from the experiments and simulations discussed in chapter 3. First it will discuss the baseline simulation focusing initially on a single trial then expanding to show some statistics for a group of 10 trials performed with the same settings. Next the chapter will discuss the variations performed from the baseline simulation. Following that discussion, the chapter will cover the results of the laboratory

experiments performed. Finally the chapter will mention some interesting notes on the results and conclude with a chapter summary.

4.2. Baseline Simulation

The first scenario to be discussed is the simulation referred to as the 'baseline'. Figure 22 shows the PSFs used to create the raw channel images in Figure 13. The estimated PSF produced by the algorithm is depicted in Figure 23 for comparison. In the end there is a very close visual match. Several different methods were attempted for defining the initial guess for the PSF. To produce an initial estimate, 1000 sample PSFs were generated using the same parameters mentioned in chapter 3. This would be based upon r_0, D and the number of Zernike polynomials used in the PSF. These samples were then recentered so that the max values overlap and then they were averaged together. The resulting average was used as the initial guess for the PSF that was actually used. An image of this initial guess is shown below in Figure 24.

The main outputs of this algorithm are the variables λ_u, λ_p, α, and χ. These are shown below in Figure 25. The truth data is shown in Figure 26 along with the truth data for the default scenario in which all four channels had 'normal' PSFs. At each iteration, the Normalized Mean Squared Error (NMSE) between the truth data and the GEM output is shown below in Figure 27. Although this experiment was run up to 1000 iterations, the improvements typically stagnated after around 200 iterations. In this scenario, error in reconstruction of λ_p appears to be the deciding factor on when to cease iterating. The discontinuities in the two angle plots occurs when the estimated PSF center shifts, causing

the resulting estimated object to shift. Because the letters are only a few pixels wide this shift causes a relatively large change from one iteration to the next. Comparing the λ_p output in the lower left of Figure 25 to the input in Figure 13, one can see that the image greatly improves over any individual channel, as a result of the information provided by the other channels. In essence, applying the blind deconvolution algorithm to the four channels together yields more information than would be gained by looking at any of the channels independently.

Finally, in Figure 28, a series of 10 experiments with the same input parameters for the PSF generator were performed to provide a clear sense of the variability that can be expected from this approach. Only λ_p is shown because it most closely resembles the initial object and can thus provide a clear, visual interpretation of how well the original object was recreated. Figure 29 shows the mean of the NMSE for the 10 trials as well as a blue band representing one standard deviation from the mean. The mean NMSE was approximately $0.9e^{-5}$. The expected mean NMSE will be situational. Situations in which the PSF creates a greater distortion on the object will likely produce a greater mean NMSE and vice versa. Conversely, situations in which the target has simpler geometry would be expected to have a lower mean NMSE.

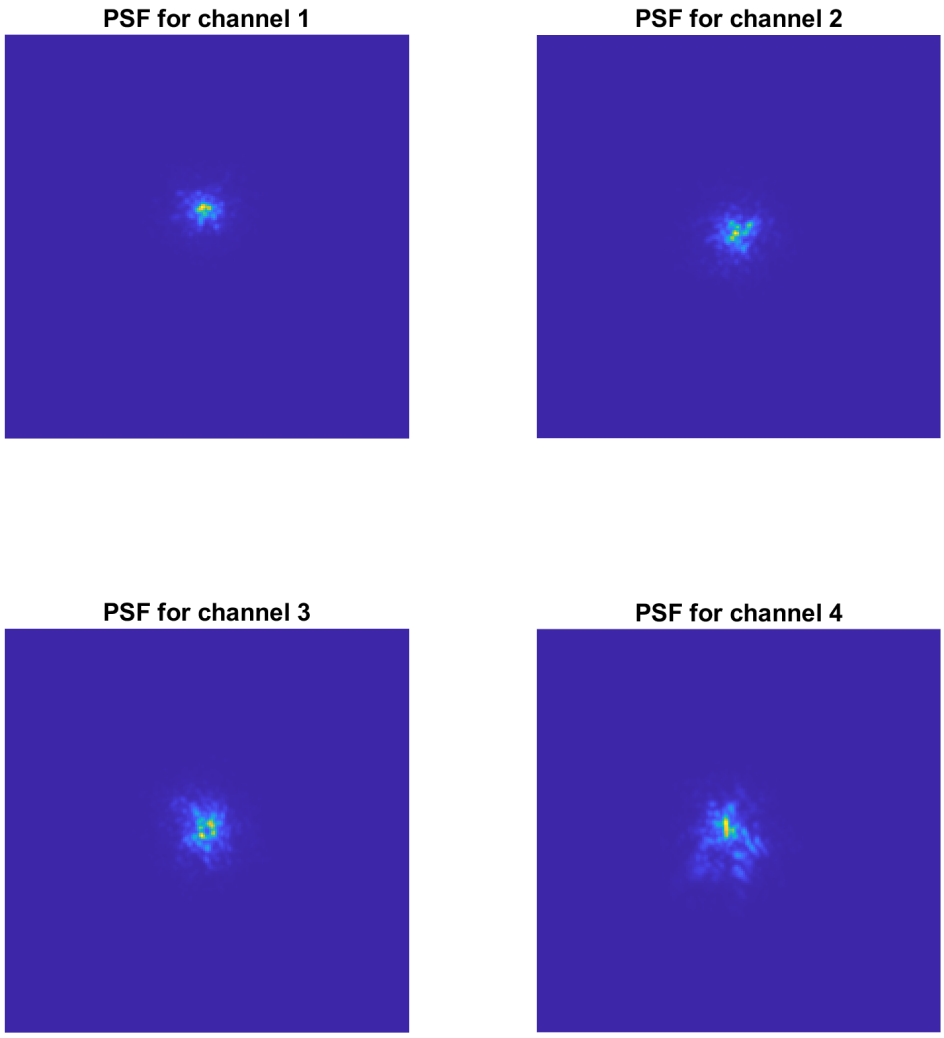

Figure 22: Actual PSF Used in Trial 1

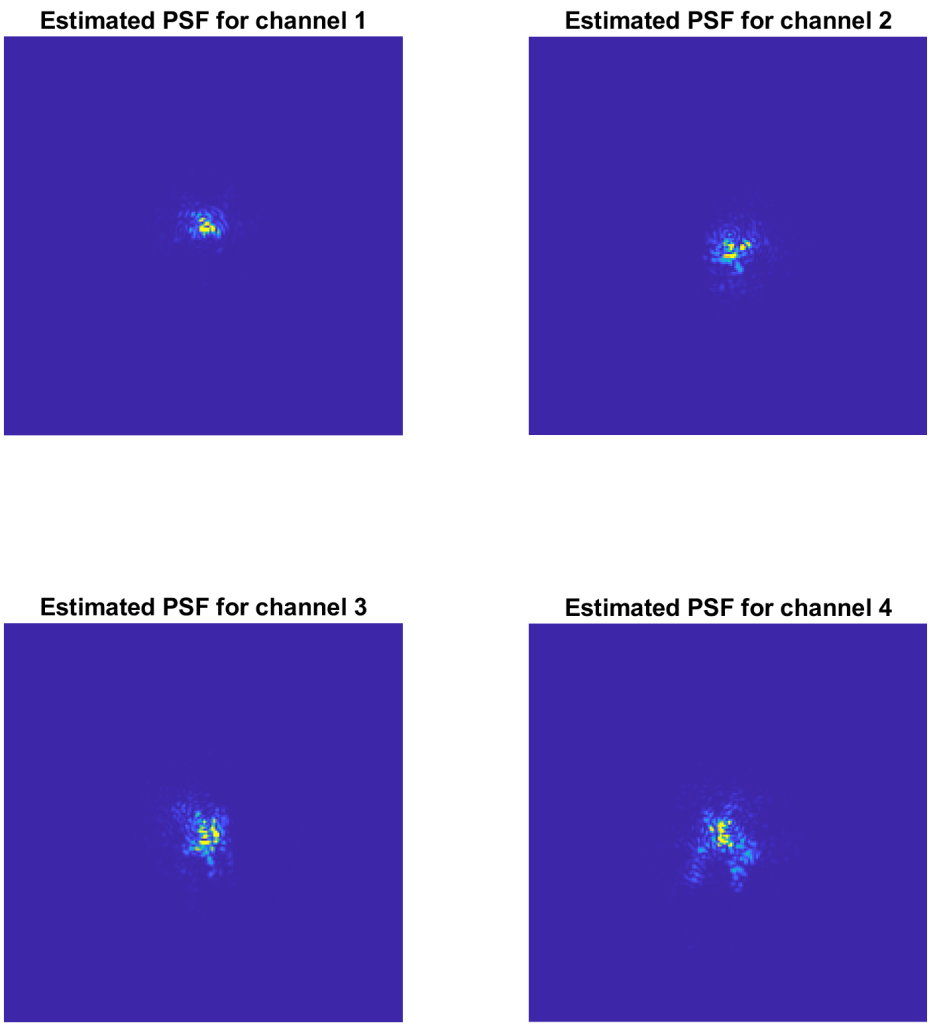

Figure 23: Estimated PSF From Trial 1

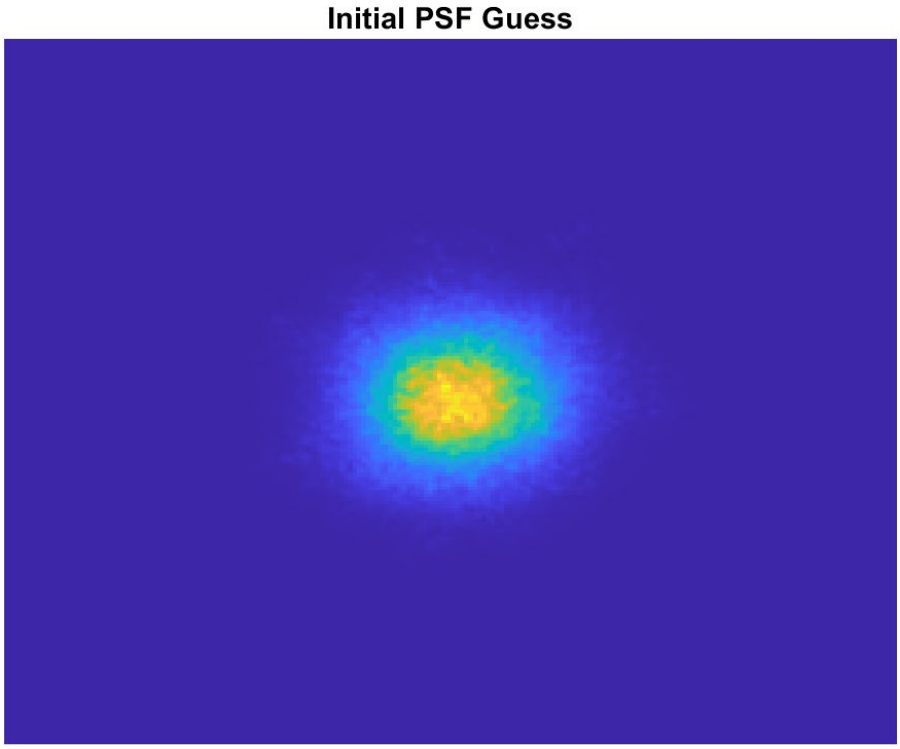

Figure 24: Initial PSF Guess

Figure 25: GEM Output From Trial 1

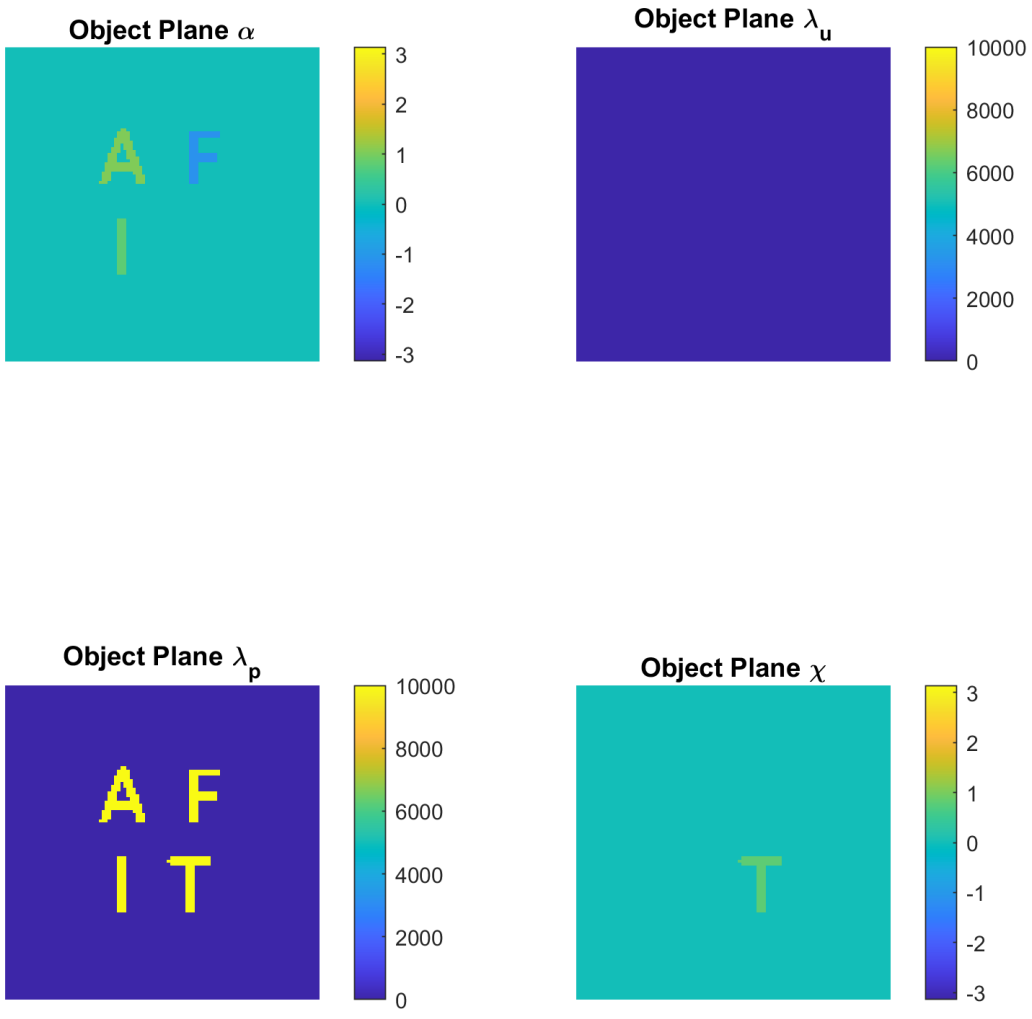

Figure 26: Object Used in Trial 1

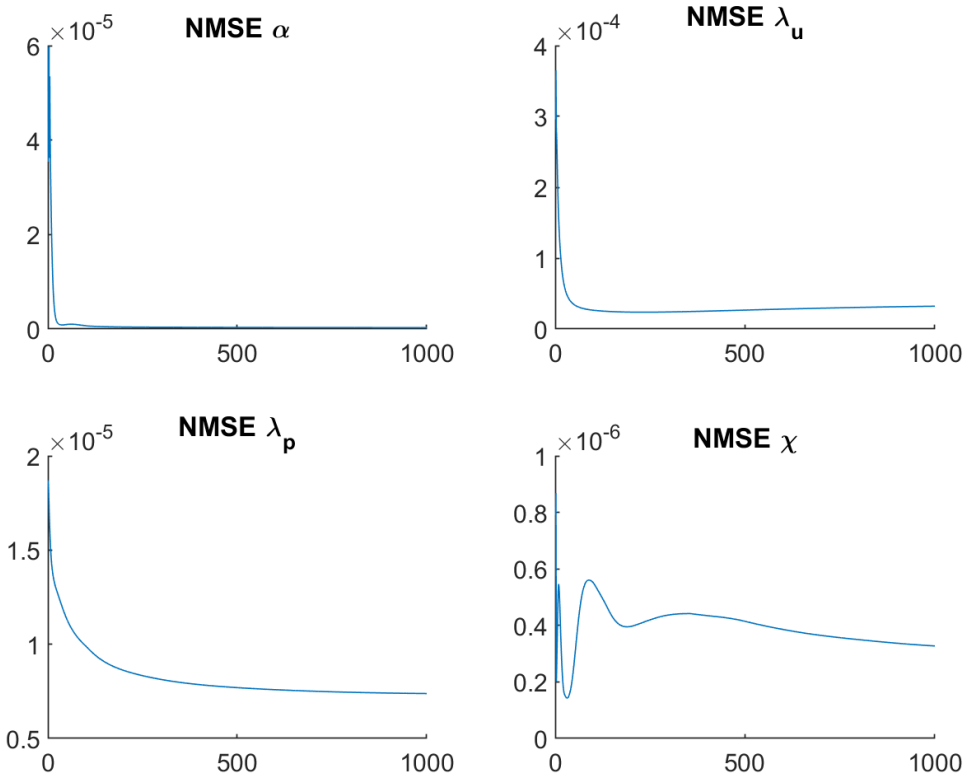

Figure 27: NMSE for GEM Output

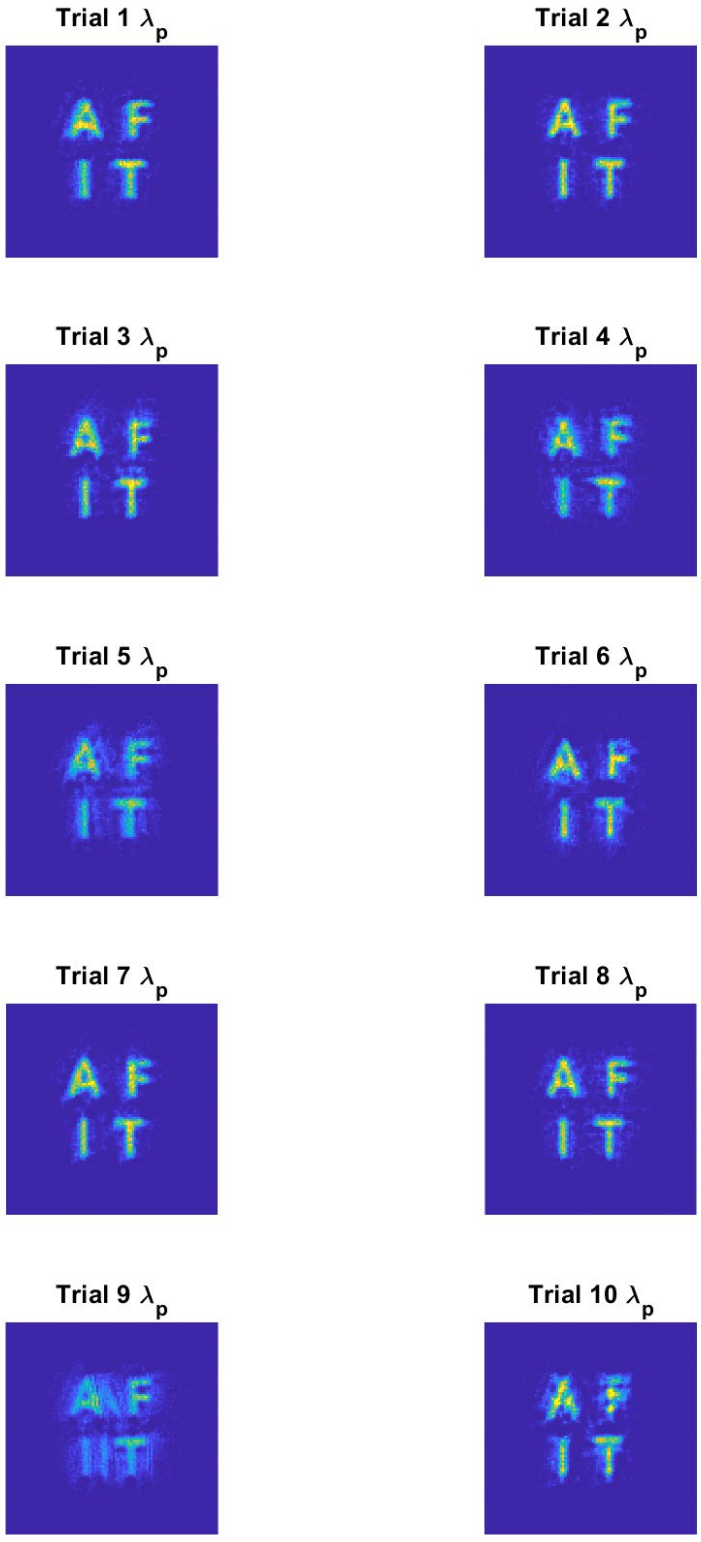

Figure 28: λ_p Estimates Across 10 Baseline Trials

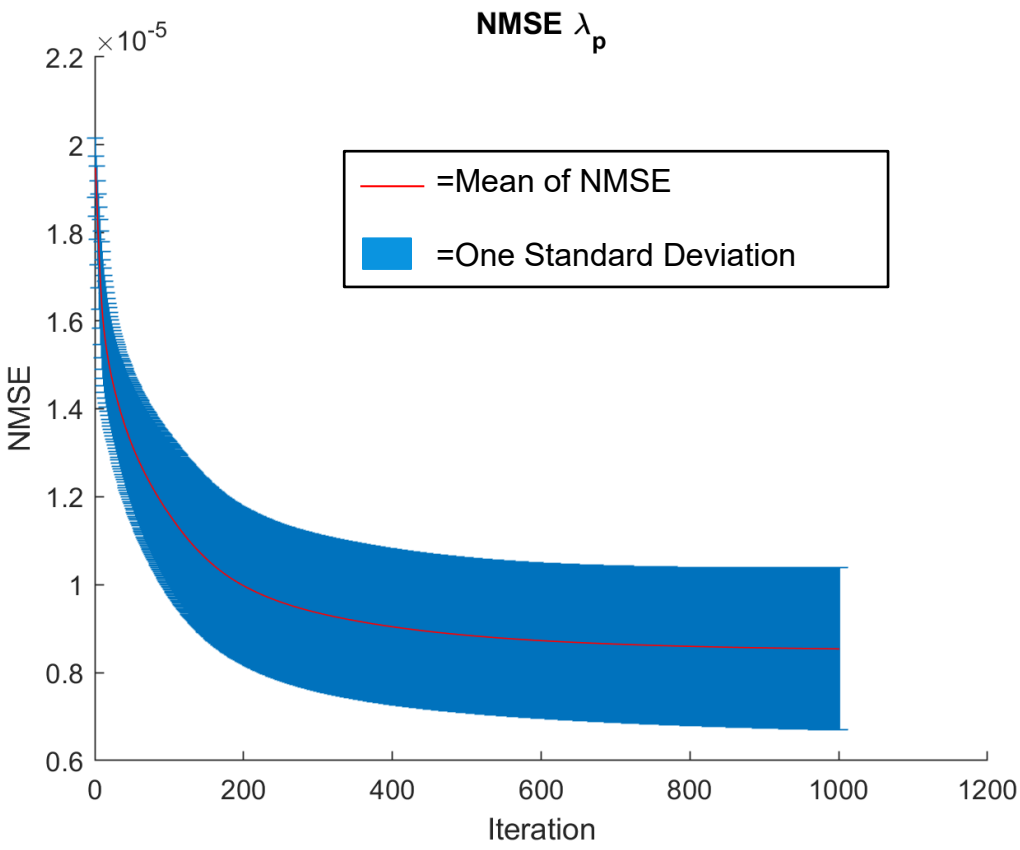

Figure 29: NMSE for λ_p For Baseline Trials

4.3. Simulation Variations

Then ten trials done for each of the variation scenarios are shown below in Figure 30-Figure 37. The λ_p outputs for the trials tested under the turbulence free phase screen $(r_0 = D)$ are shown in Figure 30 and the NMSE results over iteration number for each trial are shown in Figure 31. In this variation the input data used follows was created with the same statistics as the sample shown in Figure 14. All of the results quickly reach a very legible result. Given the clarity of the initial inputs, however, this was not an unexpected

result. Less expected is that in many cases, the results actually get worse shortly after reaching their lowest value, at least based upon the NMSE. That said, it is worth noting that the NMSE between the target and the GEM output is on a very small scale. At the end the mean NMSE for the trials was around $0.4e^{-5}$, which is roughly half the error of the baseline plot.

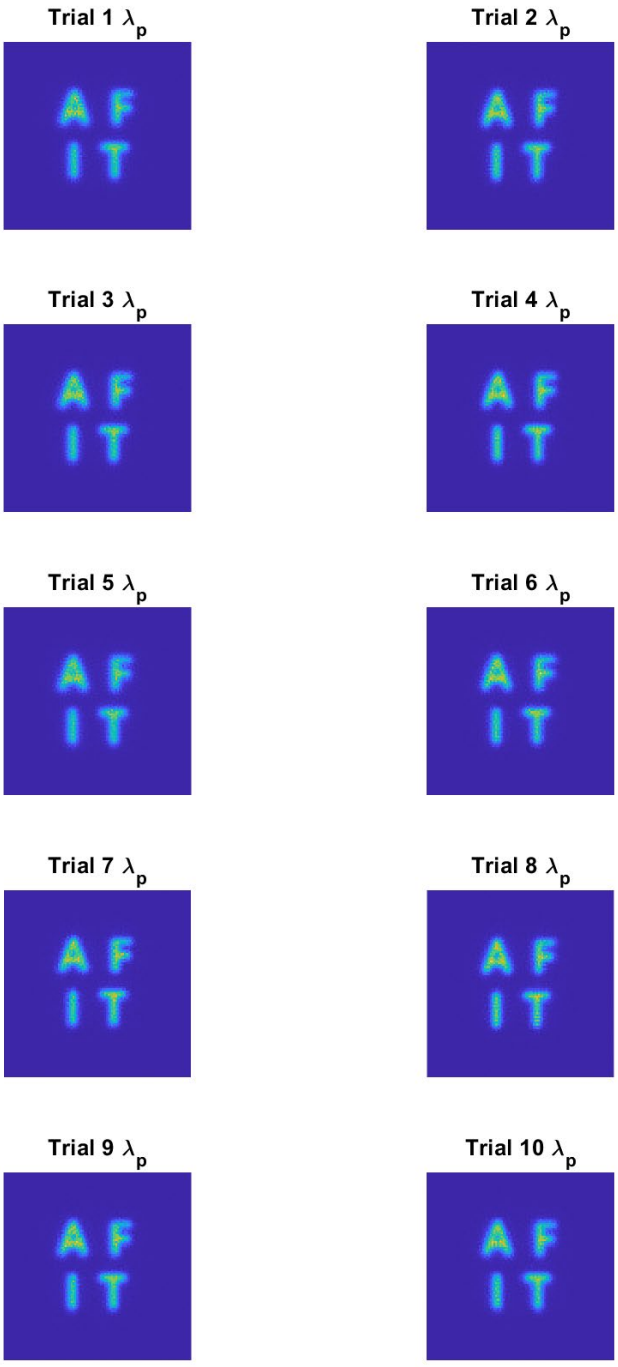

Figure 30: λ_p Estimates $r_0 = 1$ meter

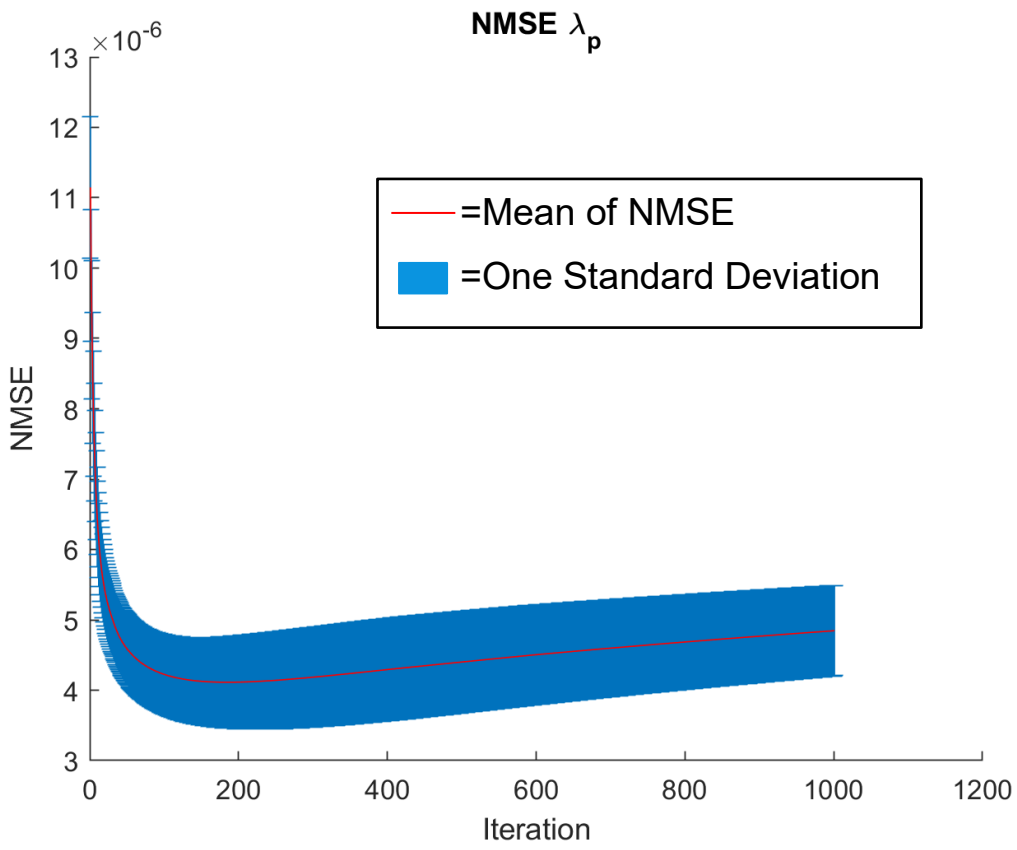

Figure 31: NMSE Results for $r_0 = 1$ meter

Next, the process was repeated with a known 'normal' PSF case ($r_0 = .1$ meter). This refers to the sample input shown in Figure 13. This variation used the same input variables as the initial experiments, but substituted the true PSF in each channel for h_c. This allowed the new portion of the GEM to be tested without being negatively impacted by issues with the GS algorithm. However, this does make it simply a 'deconvolution algorithm' instead of a 'blind deconvolution' algorithm. The resulting λ_p estimate for each trial are shown below in Figure 32 and the NMSE results are shown in Figure 33.

Although this variation has PSFs that were created with the same variables as those in the baseline, the output is far more ideal in that it has a much lower NMSE, and converges quickly. This indicates that the majority of the error in the baseline likely comes from the PSF estimation process. In this case, the mean NMSE was around $0.5e^{-5}$. Contrary to what one may expect, this result is not as good as the turbulence free case. This outcome could be a result of the cutoff occurring at 1000 iterations. It is worth noting that at this point, the turbulence free case has begun to diverge, but the known PSF case is still improving. It is also worth noting that in the known PSF case, the variance was smaller than for all other cases. In other words, because the correct PSF was entered into the equation as the initial guess, each of the different sample datasets produced roughly the same amount of error.

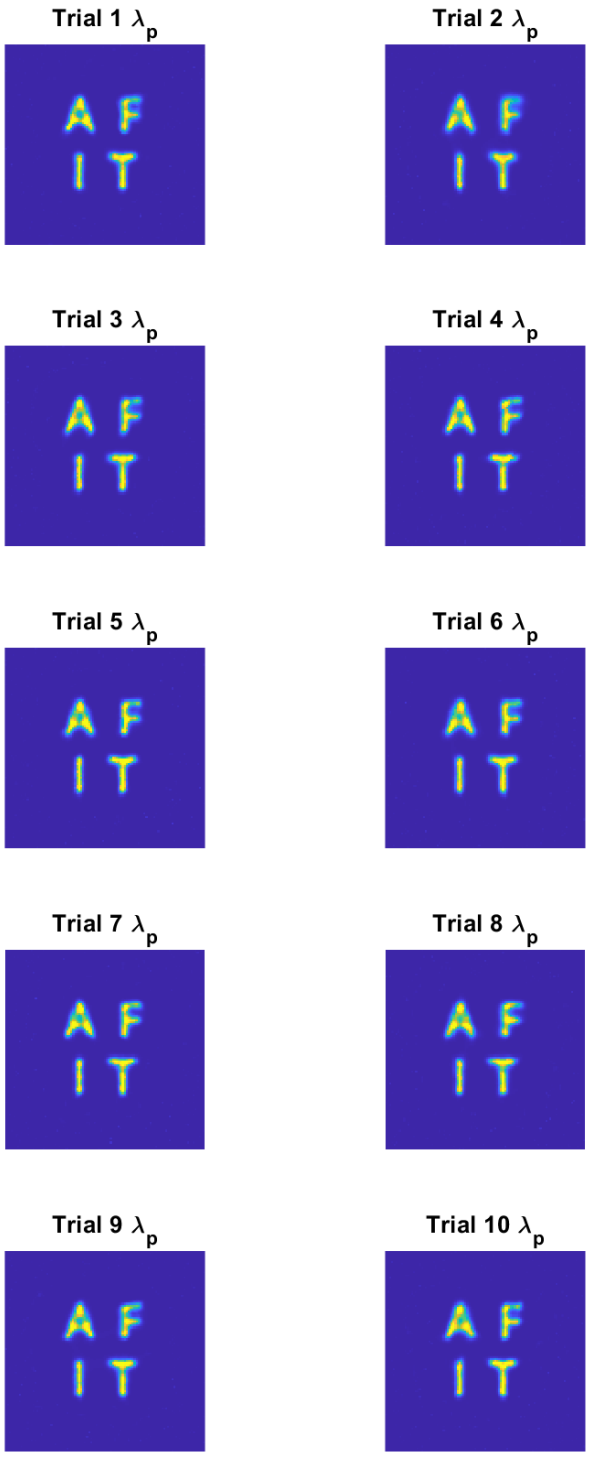

Figure 32: λ_p Estimates for a Known PSF

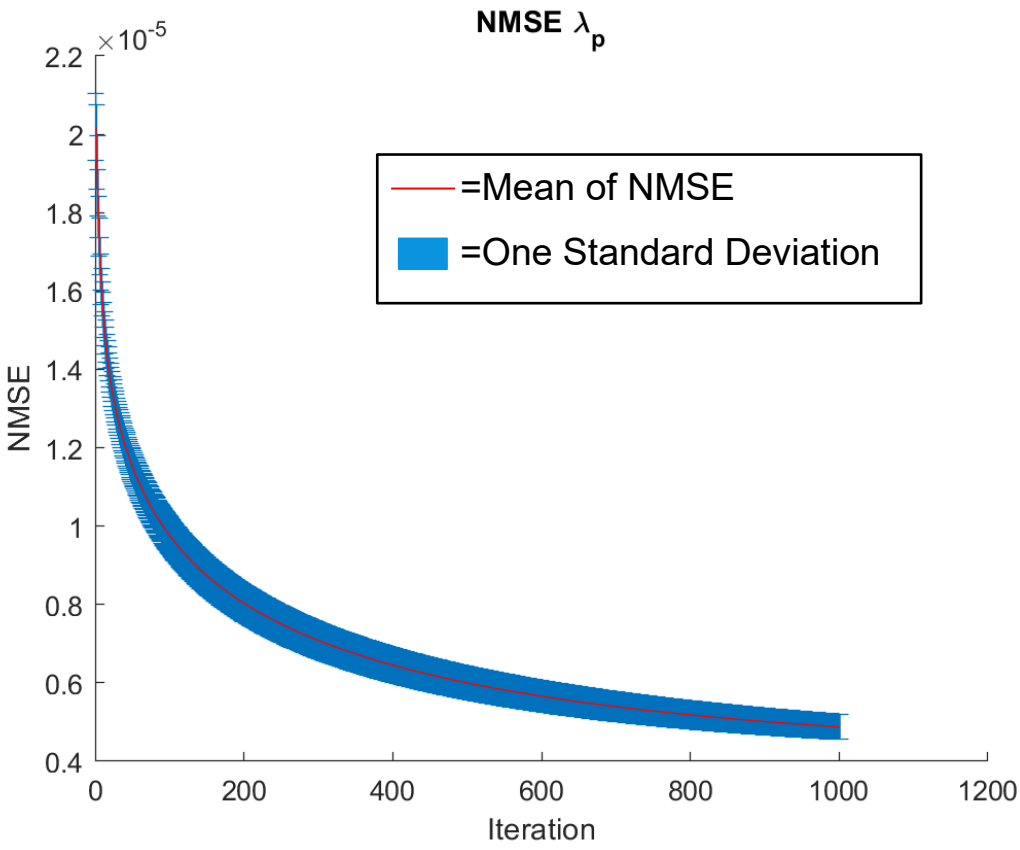

Figure 33: NMSE Results for Known PSF

The third scenario involves one channel with a turbulence free PSF ($r_0 = 1$ meter) and three with a 'normal' PSF ($r_0 = .1$ meter). This matches the input shown in Figure 15. The results of the ten trials are shown below in Figure 34 and Figure 35. While the results do not converge quite as quickly or nicely as in the known PSF case, the end result appears better than the baseline. This is due to the effect of channel 3 being able to give the majority of the information. The F is still invisible in that channel because the polarization state of the F is almost perpendicular to that of the Mueller matrix of the filter in front of channel

3. However, because of the ‘clean’ information that is obtainable, the PSFs for the other channels are easier to infer and thus the missing data can be acquired. In spite of the clean appearance, in the end, this case produced around a NMSE of $0.9e^{-5}$, which is roughly the same as that in the original experiment, though the variance is much tighter.

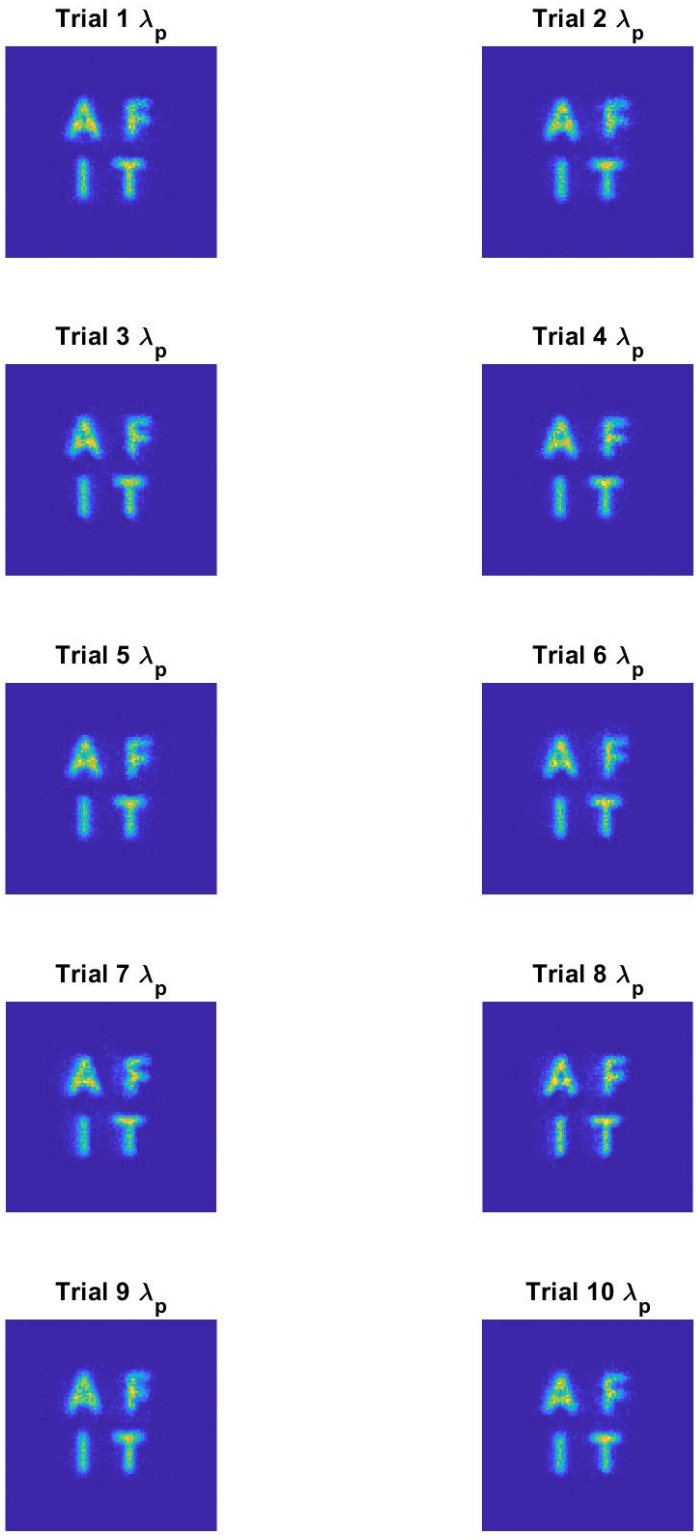

Figure 34: λ_p Estimates for Clean Channel Variation

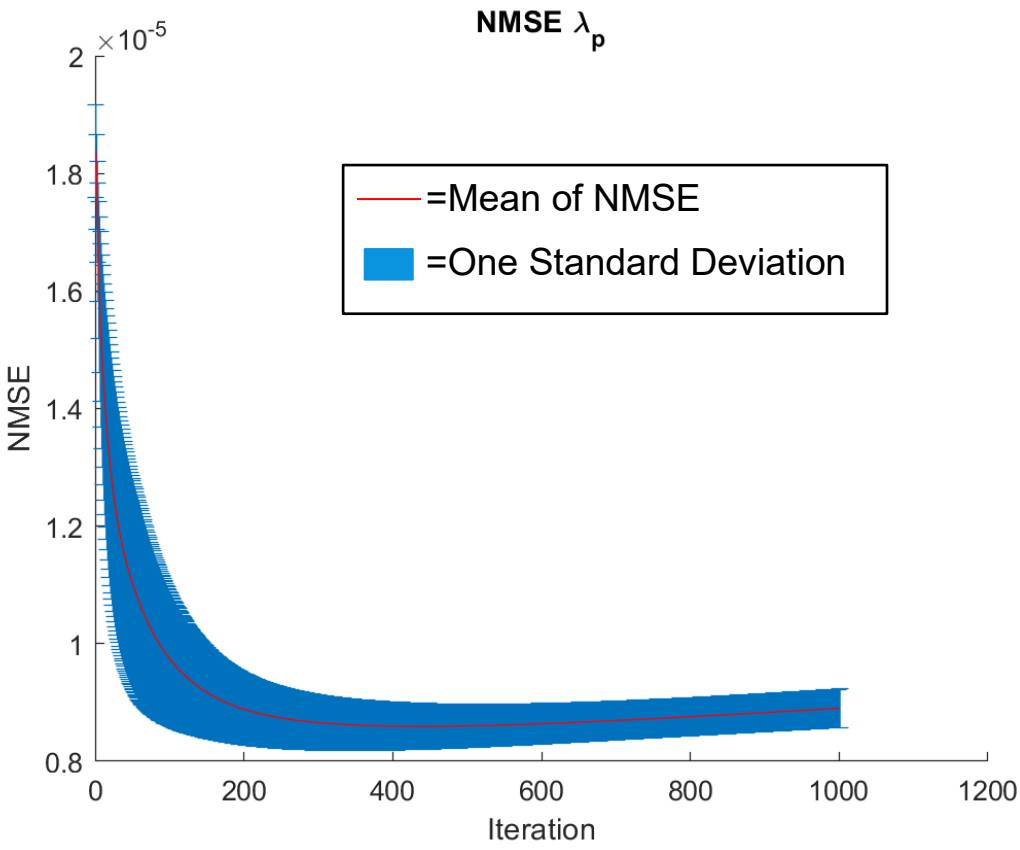

Figure 35: NMSE Results for Clean Channel Variation

Next, using the baseline PSF variables (shown in Figure 13) a different PSF initialization guess was attempted. In this case, the guess of the starting PSF was that there was nothing but a lens in front of it and the algorithm would iterate from there to discover the true PSF. Thus, any phase variation in the initial guess would be a result of known aberrations in the optical system. While this is a realistic scenario if you know nothing about the atmospheric conditions, it is severe and demonstrates the importance of having an initial guess that at least resembles the true PSF. The results are shown below in Figure

36 and Figure 37. Not only does the convergence typically happen much later (if at all) the NMSE at the point of convergence is much higher than in any of the other methods examined here.

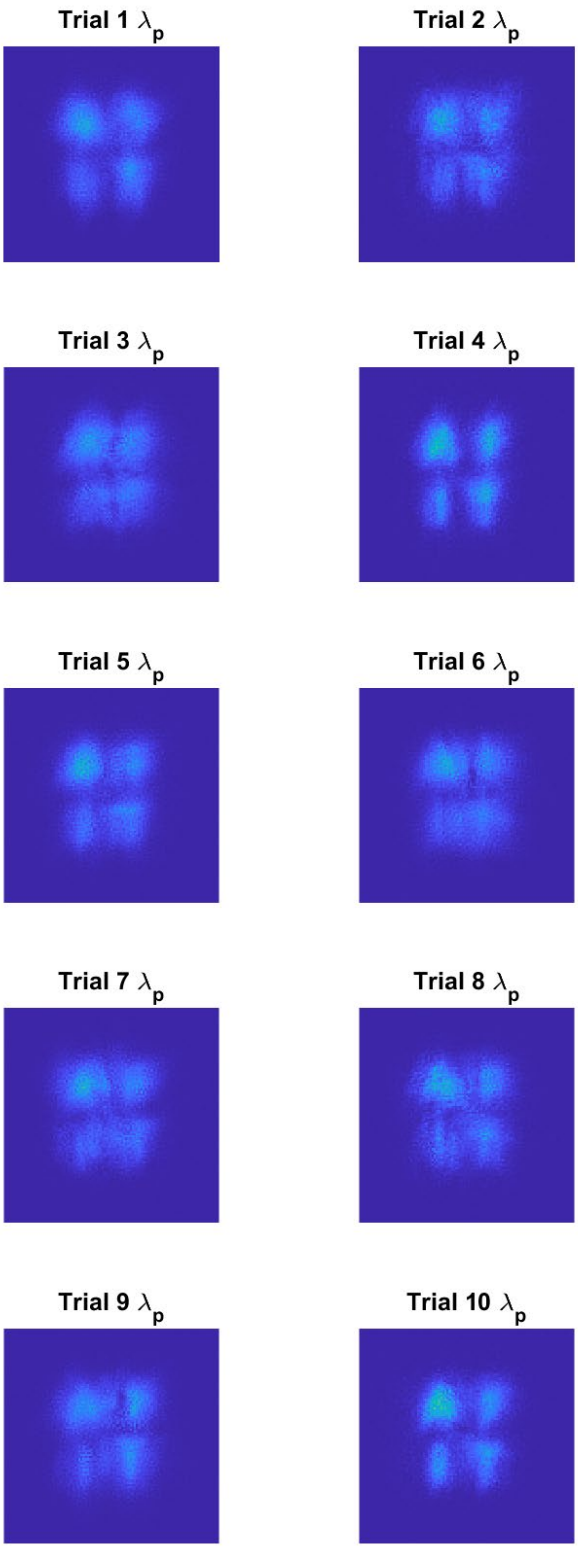

Figure 36: λ_p for Lens Only Initial Guess

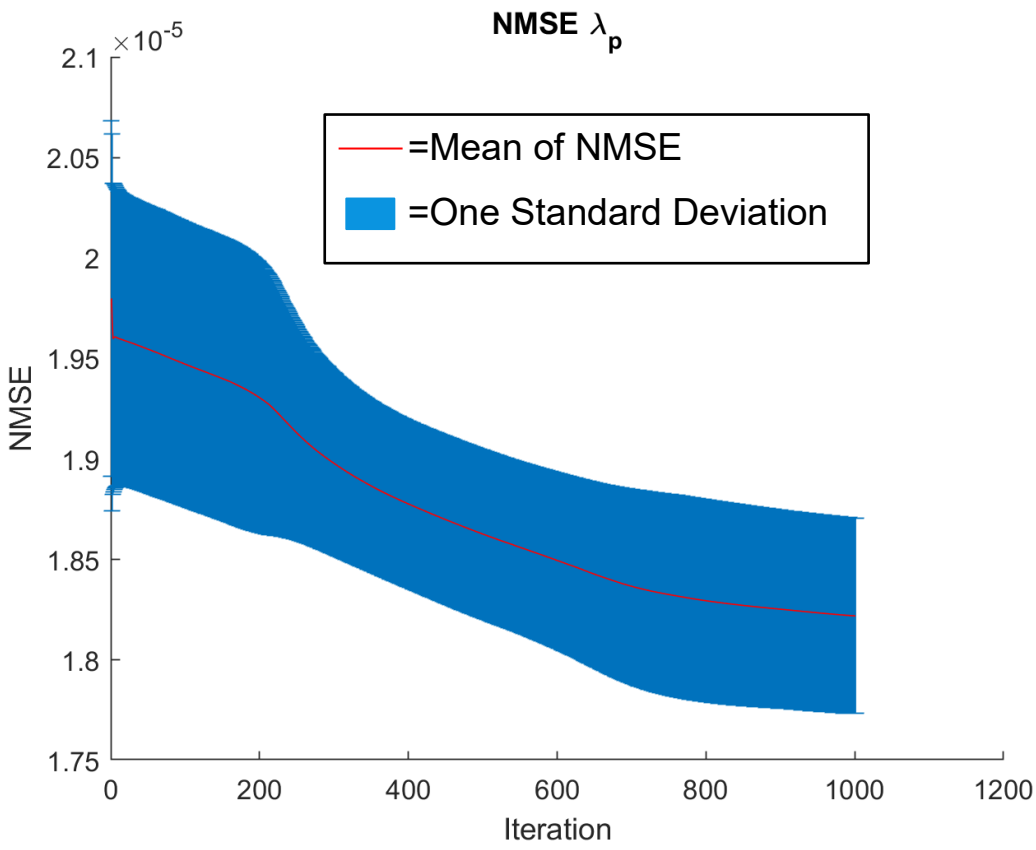

Figure 37: NMSE for Lens Only Initial Guess

Lastly a set of trials were run varying the retardance of the waveplate. This was performed using the 'normal' PSF generating parameters in all four channels which creates data similar to what is shown in Figure 13. The retardance ranged from 123-132º in one degree increments for a 10º span. The results are shown below in Figure 38**.** With a few degree offset, the image is still intelligible, however once you get past around three degrees from the baseline of 132º the restoration rapidly deteriorates, as shown in Figure 39. Even with a tuned VRW, a small temperature shift could mean a few degrees change in retardance which could seriously skew the results. An alternative method could be to

employ a quarter waveplate paired with a tight bandpass filter to achieve the desired retardance. Also, it is noteworthy that the result reaches an optimal point fairly early on in many of these cases and then diverges.

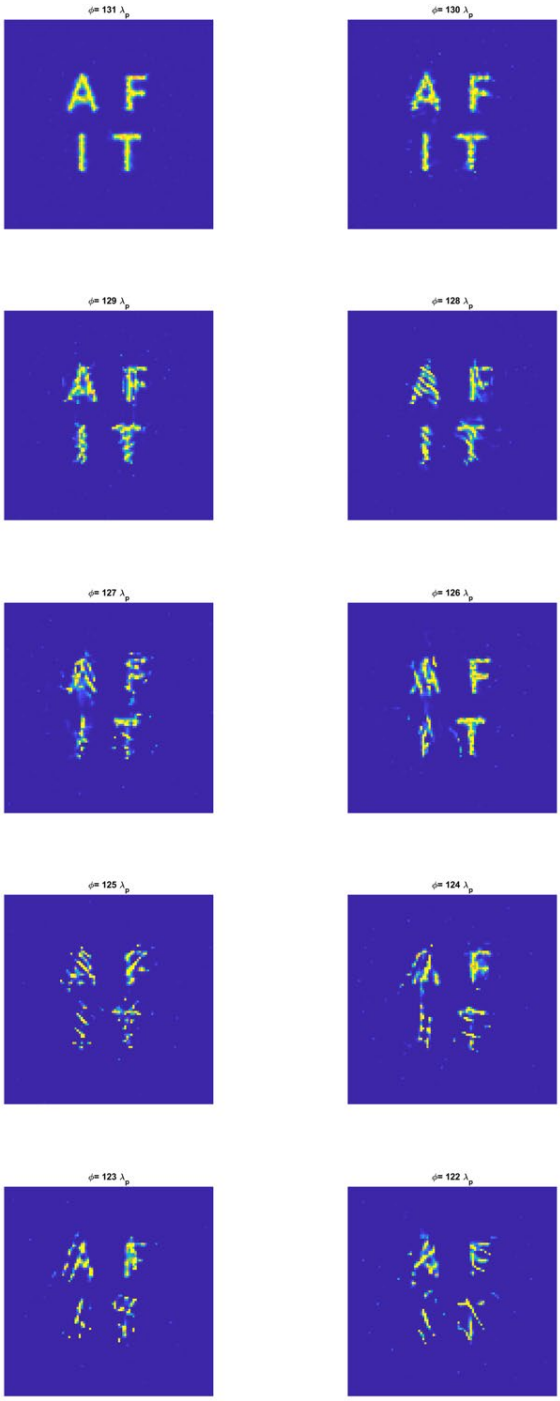

Figure 38: Effect of Lens Retardance on λ_p

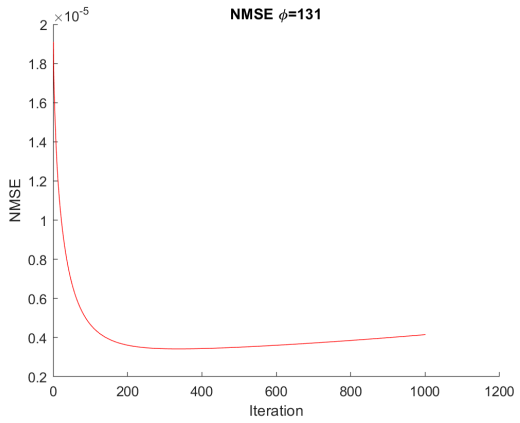
NMSE ϕ=131
$\times 10^{-5}$
NMSE
Iteration

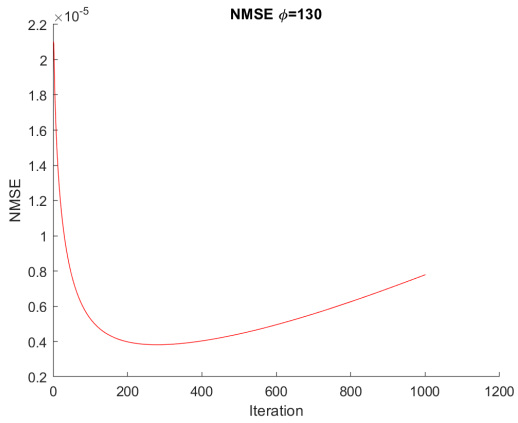
NMSE ϕ=130
$\times 10^{-5}$
NMSE
Iteration

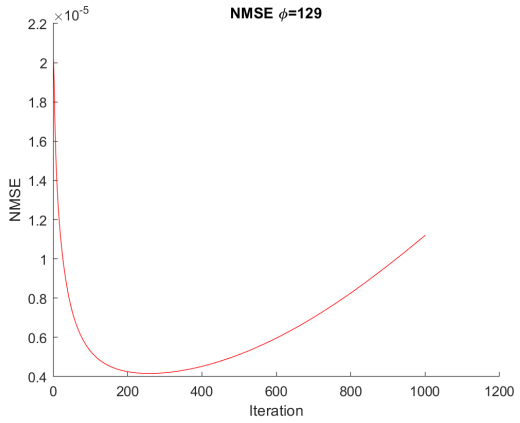
NMSE ϕ=129
$\times 10^{-5}$
NMSE
Iteration

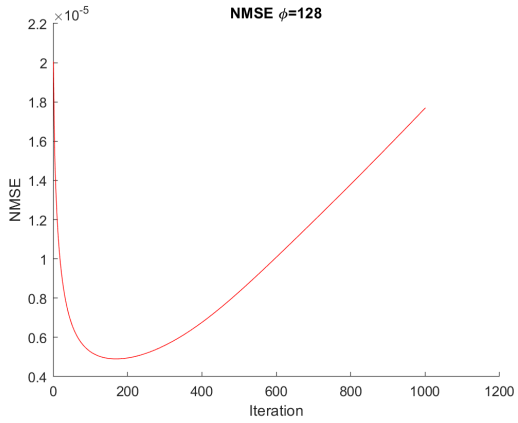
NMSE ϕ=128
$\times 10^{-5}$
NMSE
Iteration

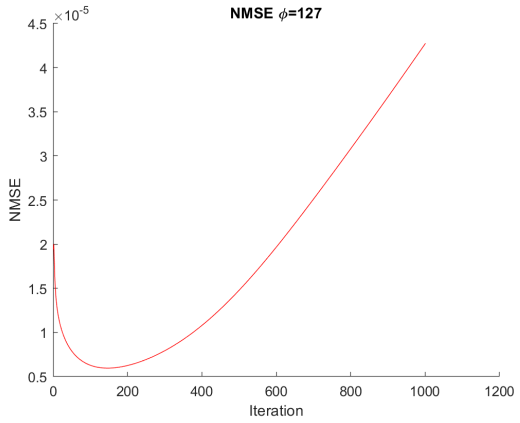
NMSE ϕ=127
$\times 10^{-5}$
NMSE
Iteration

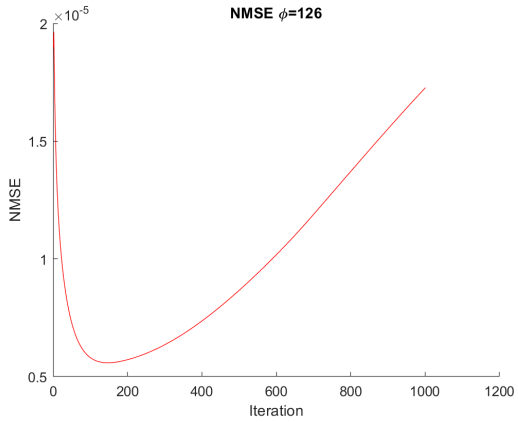
NMSE ϕ=126
$\times 10^{-5}$
NMSE
Iteration

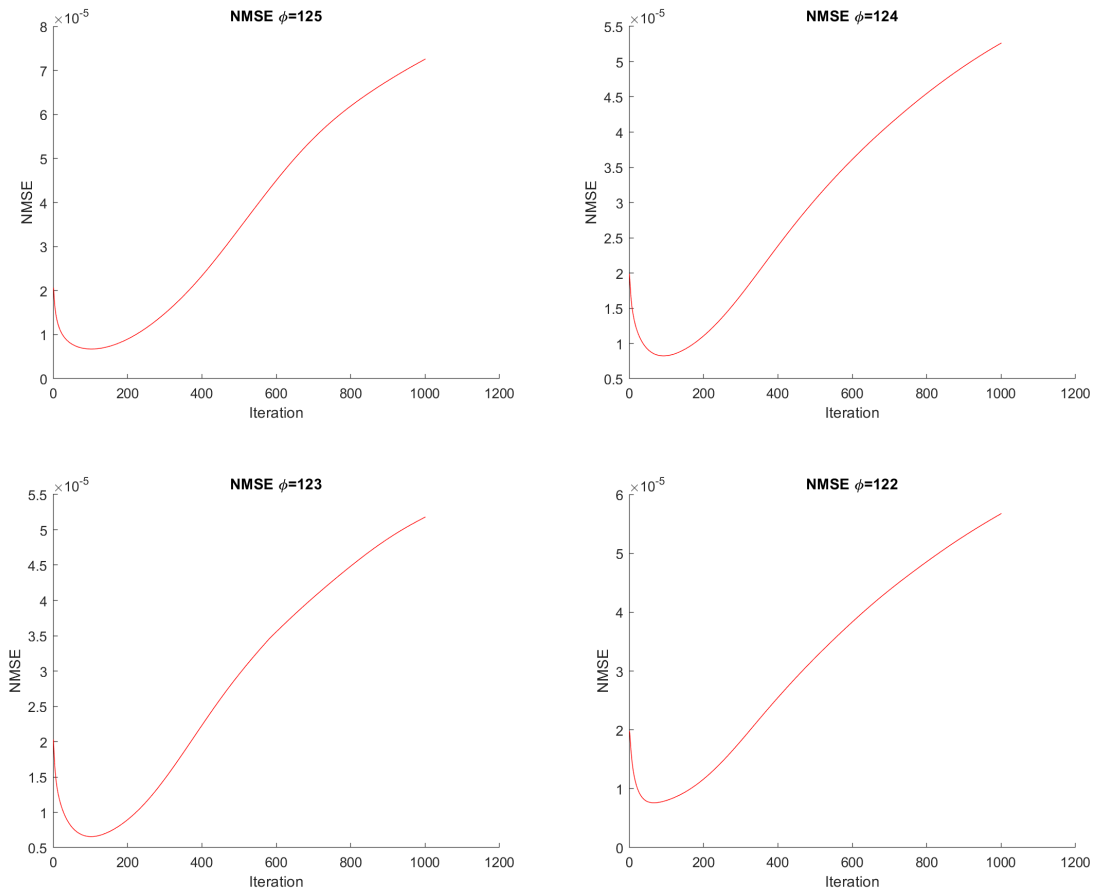

Figure 39: NMSE Effect of Lens Retardance

4.4. Lab Results

4.4.1. Single Target Tests

In the single circular light source scenario, (with initial channel inputs shown above in Figure 17), the algorithm managed to deconvolve the image into approximately a point source, which roughly matches the original source. The GEM algorithm estimated that χ was approximately 45º, which corresponds to circularly polarized light

coming from the quarter waveplate. As seen above in Figure 3, α will vary with circularly polarized light, so the value of α was not expected to be predictable unless the distance between the source and collector is known to a very precise value (ie fractions of a wavelength). The GEM output plot for this scenario is shown below in Figure 40. Because this point source is difficult to see in the full scale, additional images are attached which have been zoomed in around the area of the point source. Figure 41 shows the trimmed and zoomed image around the target to show that it was resolved to a point source. The calculated χ at that region was within 5º of the estimated value in the original source. A trimmed and zoomed version of the source, around that region, can be seen in Figure 42. The PSF estimate can be seen in Figure 43. Because the actual truth data was not known in this case, a NMSE calculation was not possible. However, it is worth noting that after 100 iterations, the image began to get worse.

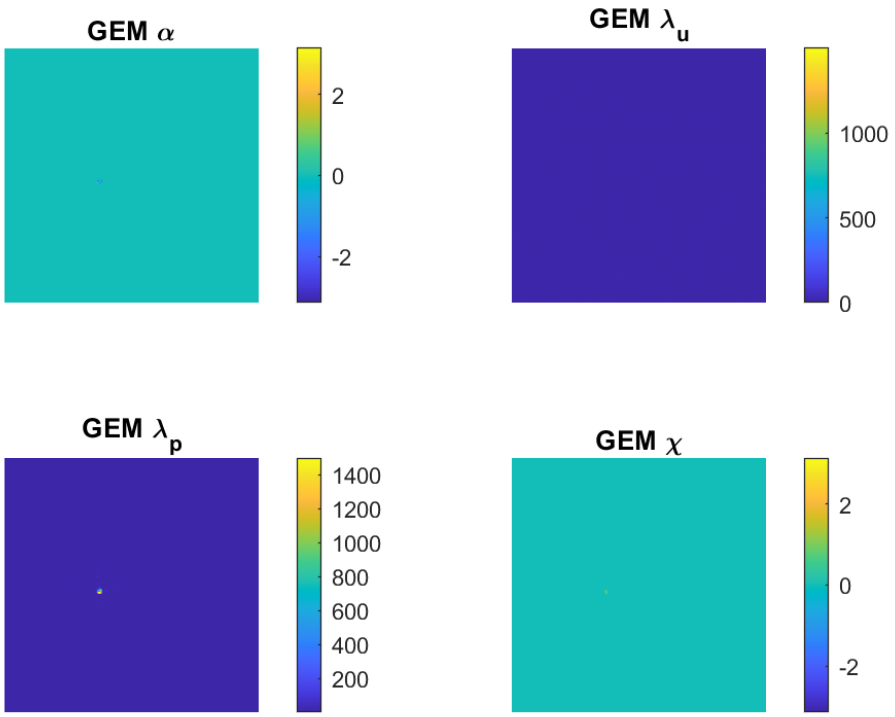

Figure 40: GEM Output from Laboratory Experiment

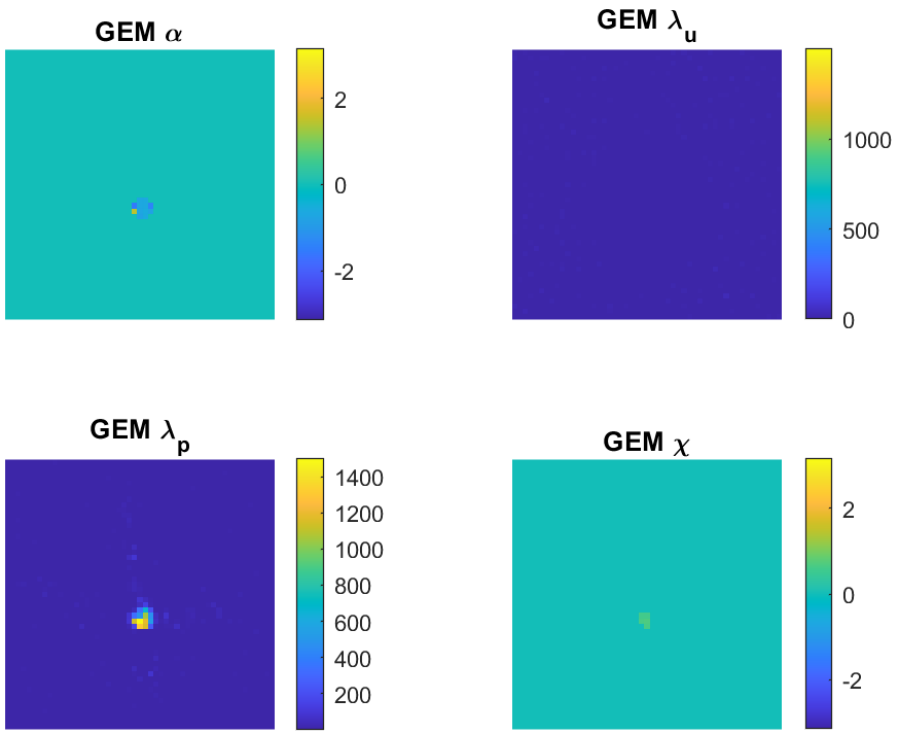

Figure 41: GEM Output Closeup

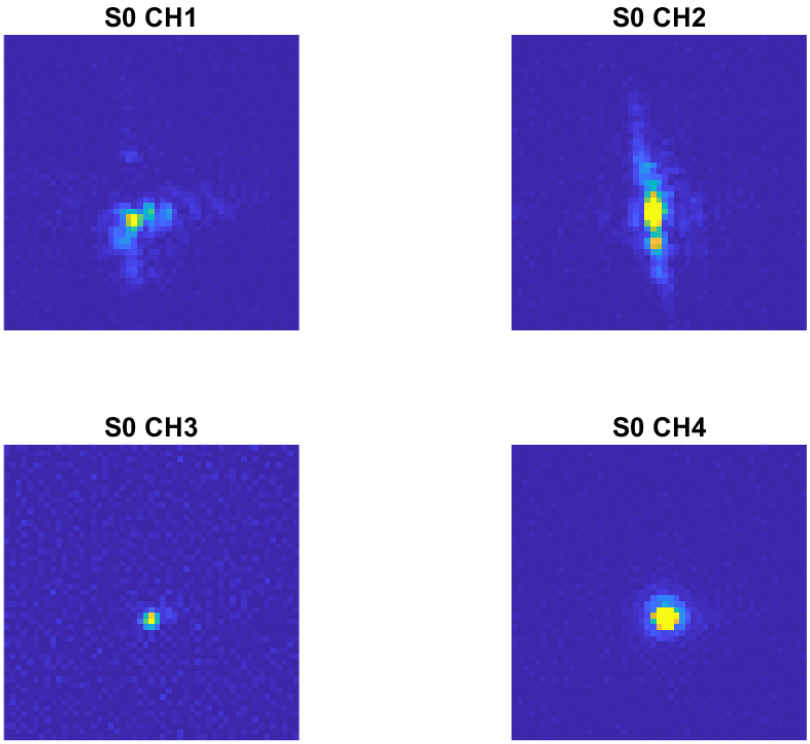

Figure 42: Original Signal

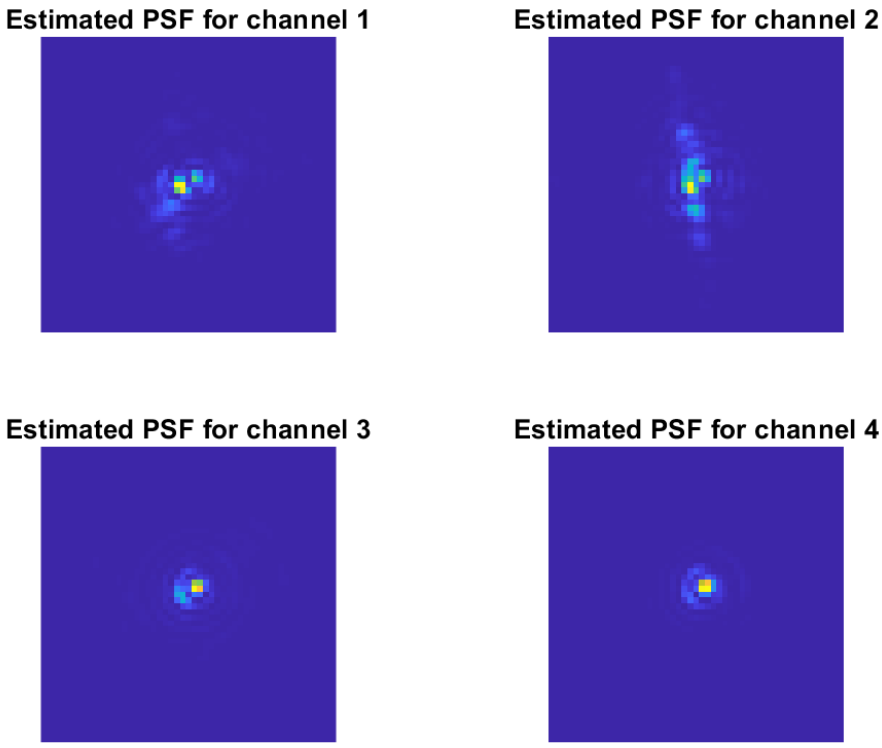

Figure 43: PSF Estimate

For the linearly polarized sample, the algorithm also successfully reconstructed the point source. It correctly determines that $\chi = 0$ at the source. The angle of polarization however, has a range of values across the source. While it does cross over the 45º mark, it ranges all the way from -45º to 75º. This is shown below in Figure 44. As with the circularly polarized sample, a zoomed in version of the original data is shown below in Figure 45. The PSF estimation is shown in Figure 46. The inability to correctly determine the angle of polarization was likely due to thermal fluctuations in the VRW. Temperature shifts in the device can cause a large shift in retardance. This is also possibly why the

algorithm resolved the target to a pair of point sources instead of just one, creating a PSF estimation that seems inconsistent with the initial data. Following the experiments, the thermal regulator registered that VRW varied from 23º C to 27º C during the experiment despite being engaged and set at 25º C. As above, the image eventually got worse but here after only around 30 iterations.

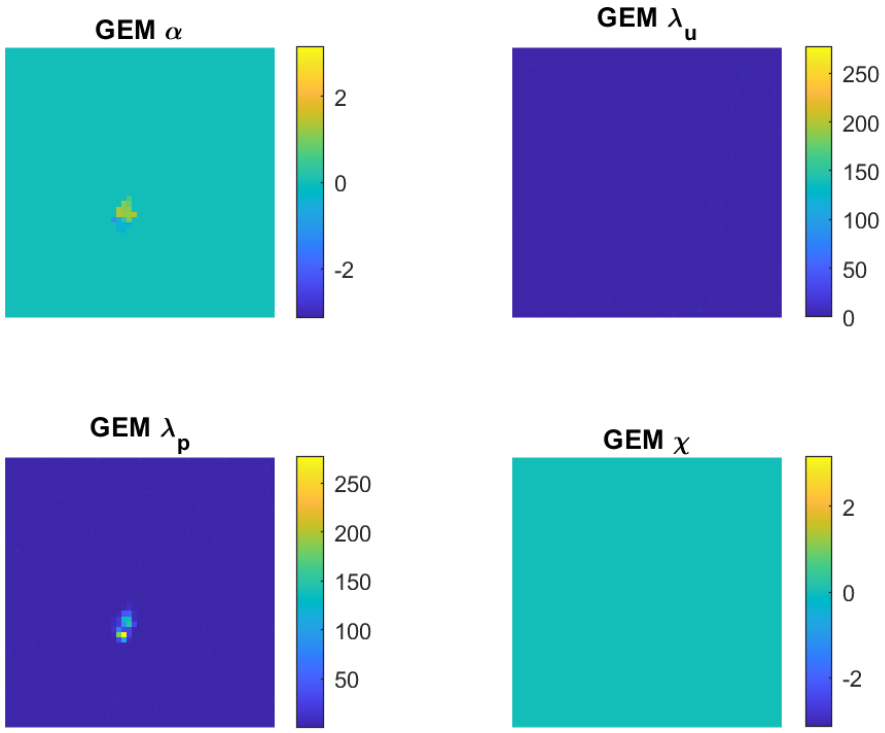

Figure 44: Linearly Polarized Point Source

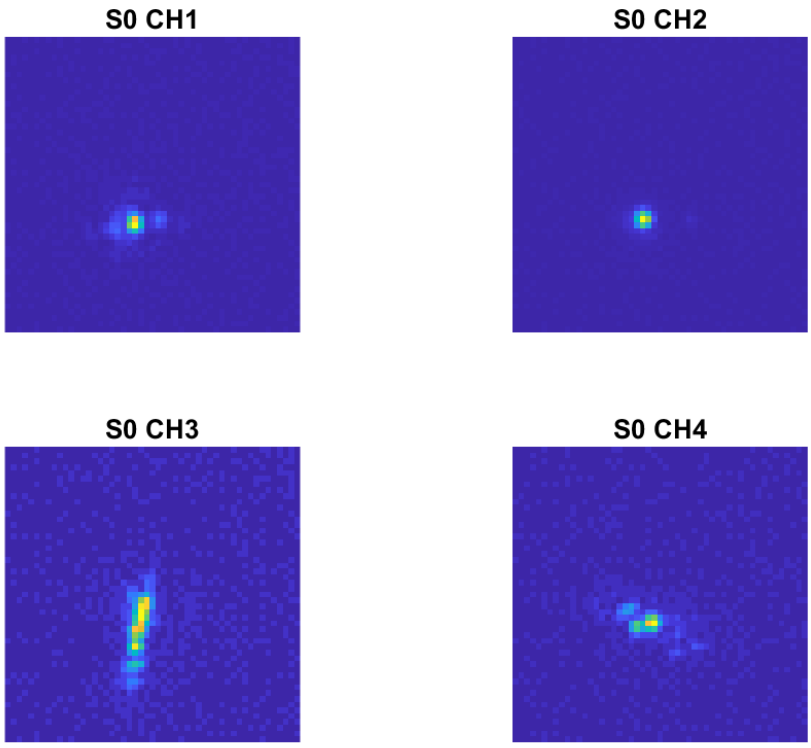

Figure 45: Linearly Polarized Source Data

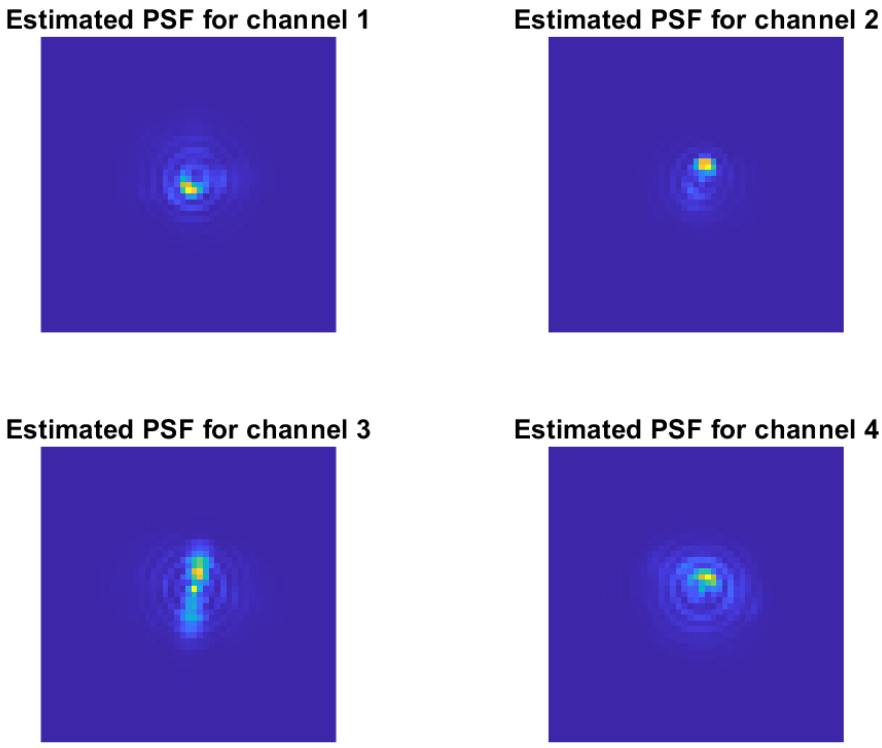

Figure 46: Estimated PSF for Linearly Polarized Source

4.4.2. Multiple Targets

In the scenario where there were two sources (with the initial inputs shown above in Figure 20), one circularly polarized and one linearly polarized, the algorithm succeeded in identifying which was which. For the linear source, the reading was $\alpha = -91°$ on a source that was actually $-90°$. The measurement was $\chi = 34°$ from light that should have had an ellipticity of $45°$. Much of this error can likely be explained by variability within the VRW. While not as large a range as in the linear case, the thermal regulator was frequently off by around a degree Celsius which can account for a shift in the waveplate's retardance. The results were actually better than expected given the results of the angle variation test

and the fact that all rotational angles had to be controlled to by hand. The GEM outputs are shown below in Figure 47. The scale for the χ has been changed to add contrast because, after filtering, it is only non-zero in a single pixel.

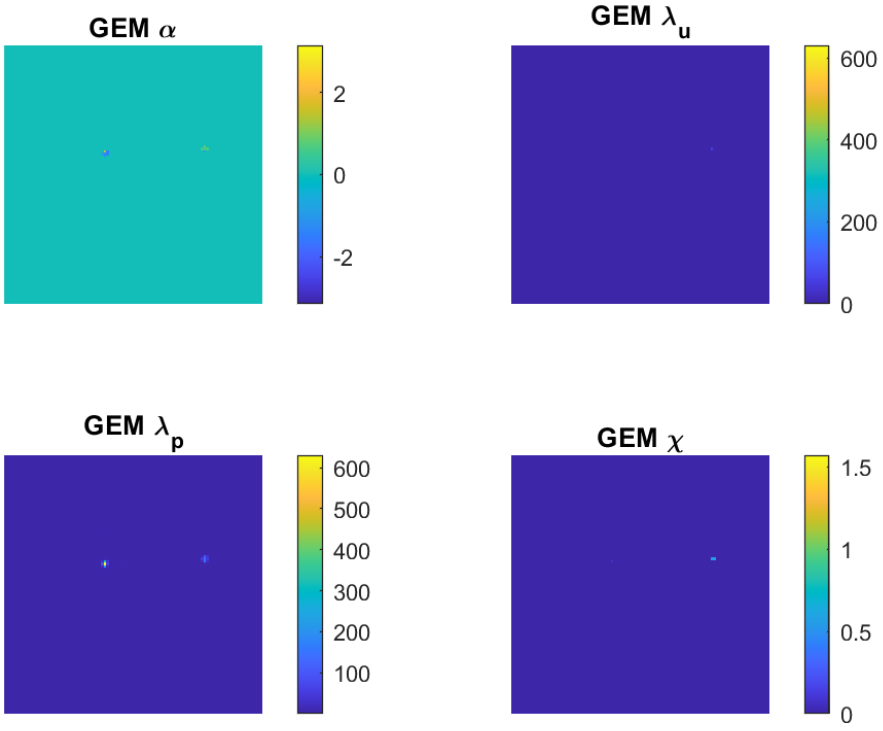

Figure 47: Two Source Differentiation

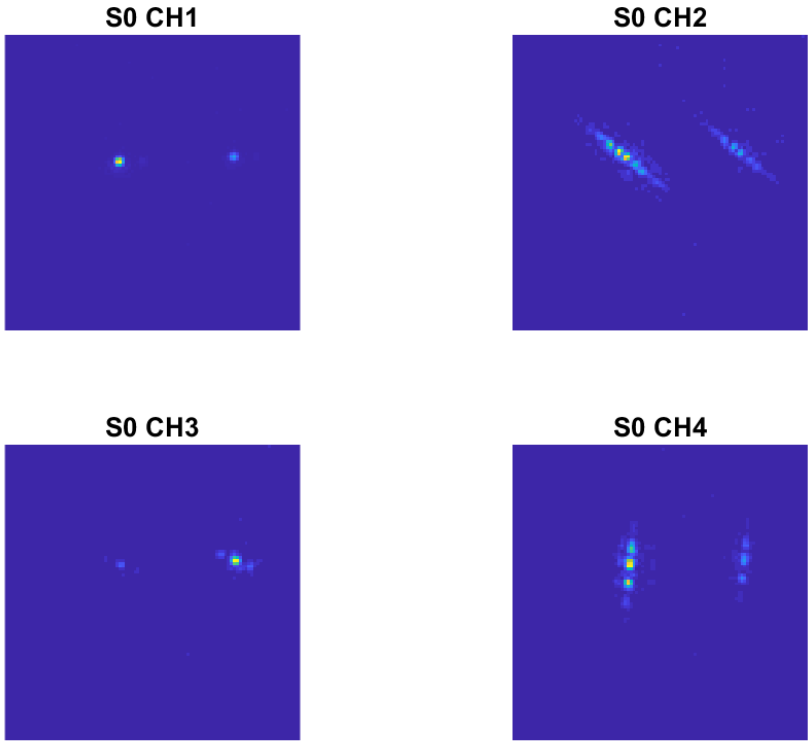

Figure 48: Data Input for Two Sources

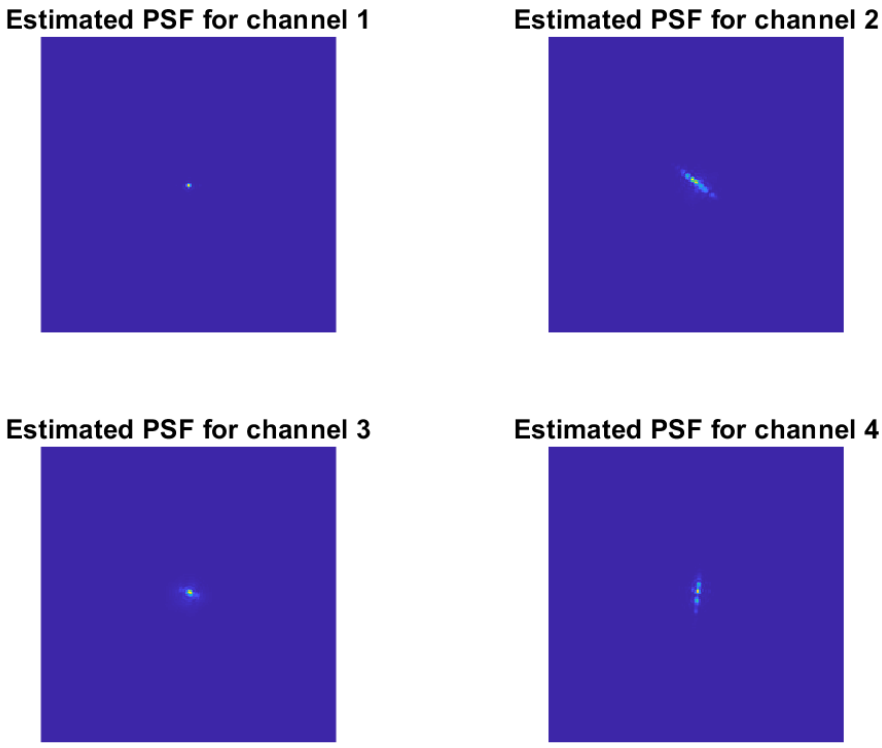

Figure 49: PSF Estimation for Two Sources

4.4.3. Multiple Targets

Finally, the bar case demonstrates the algorithm's ability to deconvolve a less trivial source. The initial inputs for this case were displayed above in Figure 21. The GEM output can be seen below in Figure 50. As before, the angle of polarization is unpredictable because the light is circularly polarized. There is no unpolarized light erroneously detected. The shape of the polarized light reconstruction matches that of the original slit. The ellipticity estimated is approximately 48º compared to the original ellipticity of 45º. A zoomed version of the original data is displayed in Figure 51 and the PSF estimate is shown in Figure 52. The bar is successfully reconstructed, however

there are some errors in the PSF estimation for channel 1. This is likely due to the turbulence produced by the plastic film not being completely isoplanatic across the image.

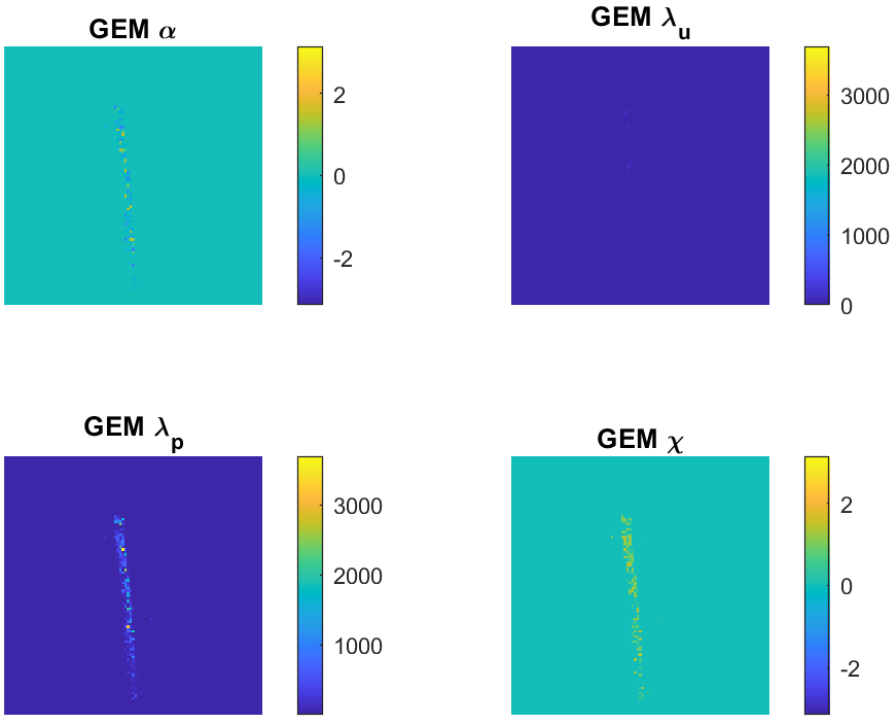

Figure 50: Bar Target GEM Output

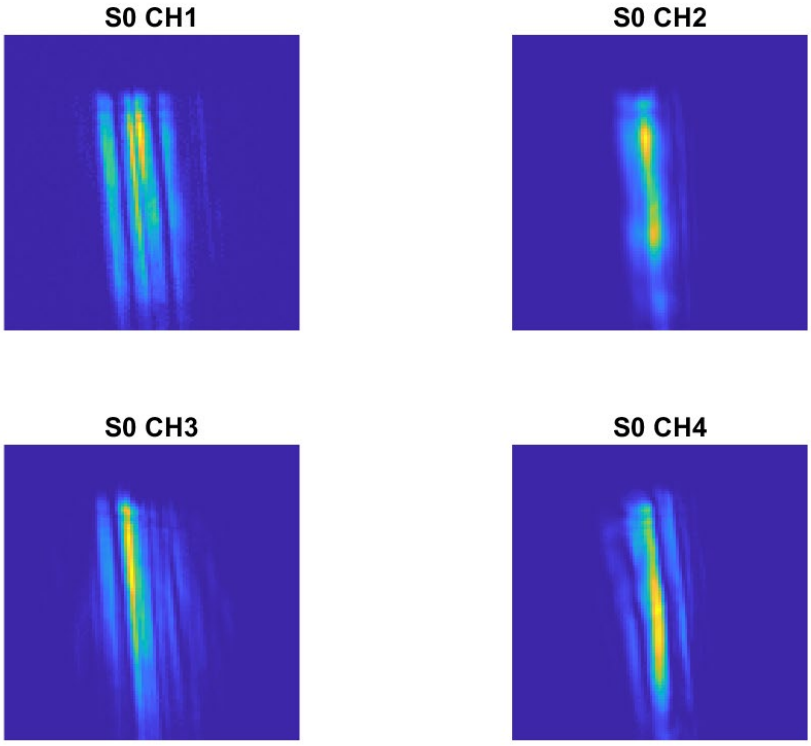

Figure 51: Data Input for Bar Target

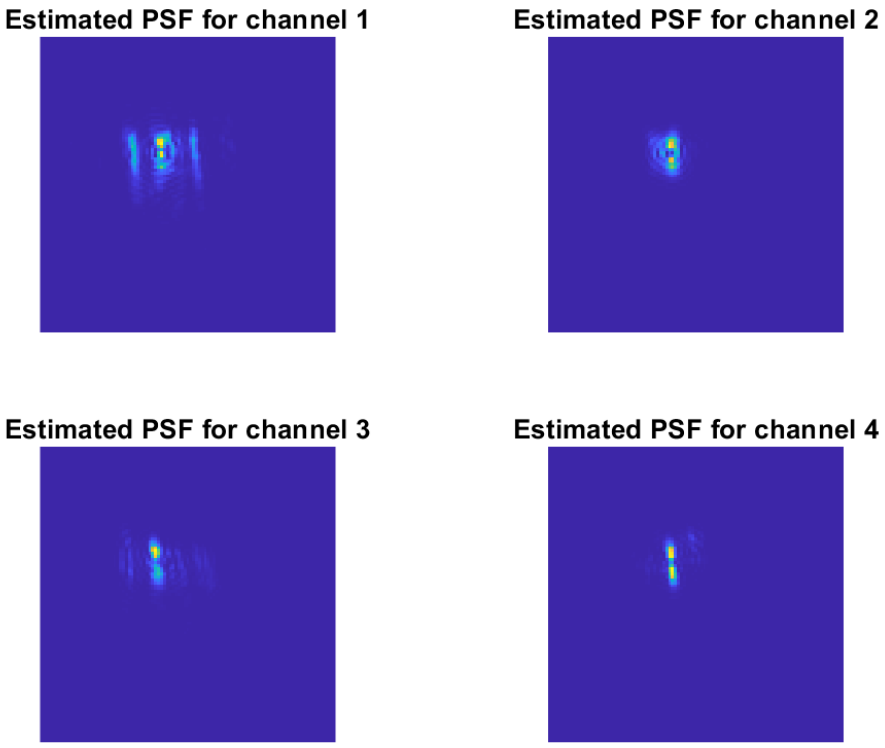

Figure 52: PSF Estimation for Bar Target

4.5. Discontinuity Discussion

Much of the discussion thus far as dealt with λ_p. This is because λ_p most closely comprises the data of the initial object. However, there are some noteworthy observations from the angle calculations as well. While this did not occur in the first trial, shown in

Figure 27, in many of the later trials, such as the example shown in Figure 53 discontinuities appear in the NMSE plots for χ.

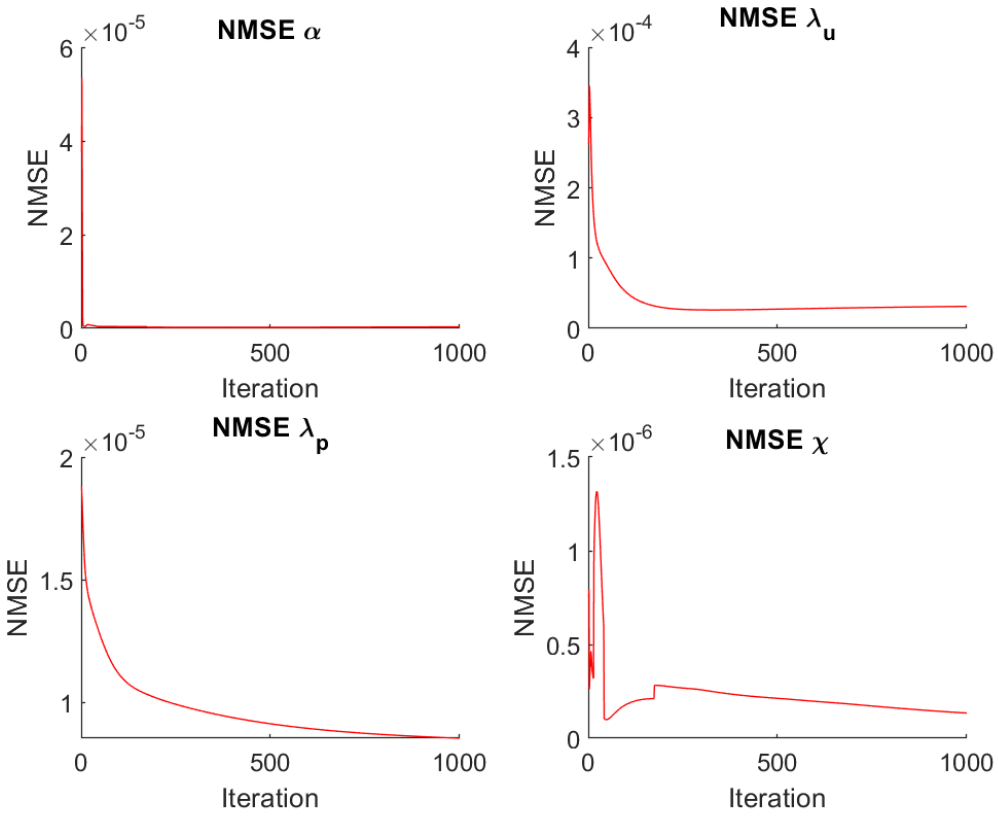

Figure 53: NMSE Data for Trial 3

This is likely caused by shifts in the estimated PSF causing a shift in the center of the estimated object. Because of the way the data is filtered, any pixel that does not contain an object is zeroed out in the angle displays, because it does not make sense to include angle estimates where there is no object. The λ_p and λ_u estimates are provided for each pixel.

Coupling this filtering with the fact that many of the letters are only a few pixels wide, a pixel or two shift in the estimated center of the object can provide a large change in the

angle estimate, potentially causing each pixel in an individual letter to change. This large shift from one iteration to the next, especially on as small a scale as the NMSE plot is, can create the discontinuities observed. This can be visually seen below in Figure 54, which shows the χ estimate for iteration 174 and Figure 55, which displays the χ estimate for iteration 151. This shows that the angle estimates for the T shift a pixel downward in the y direction during the disconnect observed in Figure 27 for χ between iteration 174 and 175.

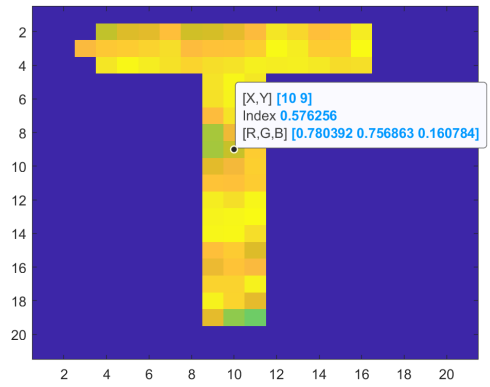

Figure 54: χ estimate for iteration 174

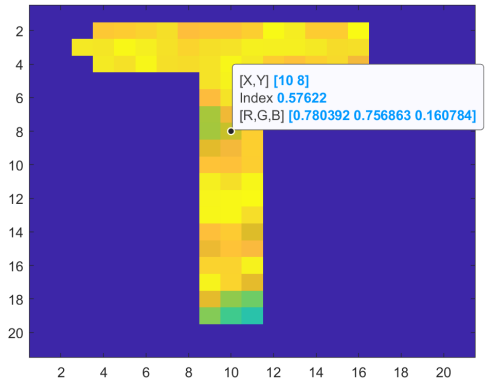

Figure 55: χ estimate for iteration 175

5. Conclusions

5.1. Summary

This chapter will discuss conclusions that have been drawn from the data collected and discussed in the previous chapters. First it will give a broad overview of the effectiveness and conditions of effectiveness for the algorithm. Then suggested areas of future research will be stated.

5.2. Effectiveness

In chapter 3, an iterative algorithm is derived which takes the equations developed by Dr. Lemaster and adds a circular polarization component to it [6]. This algorithm utilizes data from four distinct channels to develop estimates for polarized intensity, unpolarized intensity, angle of polarization, ellipticity, and the point spread function. The effectiveness of the resulting algorithm in identifying the polarization state of light is demonstrated both by laboratory experimentation and MATLAB simulations. This should enable a novel means of active polarimetric sensing that is not currently in use. Given that passive polarimetric sensing is currently employed to characterize certain materials, the addition of active polarimetry will likely expand upon this currently employed capability [26].

As seen in chapter 4, the algorithm produced a NMSE of 0.9e-5 under baseline conditions. Baseline conditions consisted of a D/r_0 of 10 and 100 Zernike polynomials for the PSF. The overall shape of the NMSE curve matches that of the prior work done in [2]. The results seen throughout this research indicate that an algorithm was developed to express

circular polarization in terms of the variables used in [6]. The resulting image, for both the baseline simulation and the experiment, was very close to the original target image in terms of both the polarized and unpolarized components. The angle of linear polarization and the ellipticity was reconstructed well in the baseline simulation as well as in some of the lab simulations. The mean ellipticity (the component that is being added by this research) error for the baseline simulation was approximately 5º. The ellipticity error in the simple circular only lab experiment was 5º and for the bar target the error was 3º. However, the lab experiments in which the temperature, and thus the ellipticity, of the waveplate varied during the simulation, the resulting angle of polarization as well as the ellipticity, tended to be less accurate. But even in these cases, the algorithm did succeed in creating a good reconstructing of the polarized and unpolarized image. The angle of ellipticity in the scenario with two targets, that is, the scenario with circularly polarized light that had the greatest thermal variance, was 11º

The variations of the baseline simulation demonstrated that having a PSF estimate that is of the same form as the one used makes a large difference in the outcome. When the PSF form is not known (as was demonstrated with the experimental example) the best outcome is achieved with an initial guess of a Zernike phase screen with one to two waves of defocus. While eliminating all turbulence provided a predicably improved outcome (cutting the NMSE by 50%), clearing up only one channel did not improve the outcome.

5.3. Future Work

This section discusses recommendations for future work related to this field. These suggestions could help further develop the existing algorithm and likely enhance its efficacy.

5.3.1. Multiframe Blind Deconvolution

Coupling this technique with a multi-frame blind deconvolution technique such as that seen in [18] or [27] would likely help the outcome. Adding additional frames to each channel has helped to improve other blind deconvolution methods so it is logical to assume that it would here as well.

5.3.2. Retardance Stability

The retardance of the VRW was shown to be very dependent upon temperature. Therefore a different, more specialized waveplate that is less thermally sensitive will also lead to a more stable replication of the original image. This could be done by having a lens cut to deliver the specified retardance at a desired wavelength. Finding a material that is more thermally resilient would likely be a material science project. A simpler solution could even be to match a quarter waveplate with a narrow bandpass filter to create the optimal retardance.

5.3.3. Waveplate Diagnostics

An alternative method of dealing with errors mentioned in 5.3.2. would be to include an algorithm to maximize the likelihood of the waveplate error. This could enable retardance error to be calculated out of the output. This would not only alleviate

the need for a more stable waveplate but also could allow for corrections in other areas, such as the wavelength filter.

5.3.4. Improved Stopping Criteria

Another area of future work could be to develop a more accurate stopping criteria. As seen in both Figure 39 and the laboratory experiment, if the retardance of the waveplate is not properly tuned, the algorithm does not always converge. However, as seen in the laboratory experiments, a reasonable result can still be gained if you look at an image in the middle of the algorithm. Figuring out where to stop to get the optimal image could be an interesting project as well.

5.3.5. Material Characterization

As discussed in chapter 2, if light bounces off of an object, and the elements of the initial Stokes vector are known, this algorithm allows the elements of the reflected light to be estimated. Knowing both the initial and the final Stokes vectors allows the polarimetric reflectance of the material to be calculated. A database of the polarimetric reflectances could be compiled, similar to what was done in [8], but including circular polarization as well. Doing so would enable this algorithm to assist in material identification through a turbulent medium, such as the atmosphere.

Appendix A: Proof for α

The first method to attempt to optimize the α update equation was to follow suite from the other update equations and take the derivative of Q^{n+1} with respect to α, set it equal to zero and solve for α. Doing so produced Equation (A.1).

$$\frac{dQ^{n+1}}{d\alpha} = \sum_y \sum_c \left(\begin{array}{l} h_c \lambda_p \left(\begin{array}{l} \cos(2\chi)\sin(2\alpha)\left(\cos(2\theta_c)^2 + \cos(\phi_c)\sin(2\theta_c)^2\right) \\ +\cos(2\alpha)\cos(2\chi)\cos(2\theta_c)\sin(2\theta_c)\left(\cos(\phi_c)-1\right) \end{array} \right) \\ -\dfrac{\psi_{pc} \left(\begin{array}{l} \cos(2\chi)\sin(2\alpha)\left(\cos(2\theta_c)^2 + \cos(\phi_c)\sin(2\theta_c)^2\right) \\ +\cos(2\alpha)\cos(2\chi)\cos(2\theta_c)\sin(2\theta_c)\left(\cos(\phi_c)-1\right) \end{array} \right)}{\left(\begin{array}{l} \dfrac{\cos(2\alpha)\cos(2\chi)\left(\cos(2\theta_c)^2 + \cos(\phi_c)\sin(2\theta_c)^2\right)}{2} \\ -\dfrac{\sin(2\chi)\sin(2\theta_c)\sin(\phi_c)}{2} \\ -\dfrac{\cos(2\chi)\sin(2\alpha)\cos(2\theta_c)\sin(2\theta_c)\left(\cos(\phi_c)-1\right)}{2} + \dfrac{1}{2} \end{array} \right)} \end{array} \right) \quad \text{(A.1)}$$

After the summing over the four channels, and then substituting in θ_c and ϕ_c from Equations (3.14) and (3.13) , Equation (A.1) becomes Equation (A.2).

$$\frac{dQ^{n+1}}{d\alpha} = \sum_{y} \begin{aligned} &\psi_1\left(\frac{0.376\cos(2.0\alpha)\cos(2.0\chi)+0.58\cos(2.0\chi)\sin(2.0\alpha)}{0.361\sin(2.0\chi)-0.29\cos(2.0\alpha)\cos(2.0\chi)+0.188\cos(2.0\chi)\sin(2.0\alpha)+0.5}\right) \\ &-h\lambda_p\left(0.376\cos(2.0\alpha)\cos(2.0\chi)+0.58\cos(2.0\chi)\sin(2.0\alpha)\right) \\ &-\psi_2\left(\frac{0.726\cos(2.0\alpha)\cos(2.0\chi)+0.58\cos(2.0\chi)\sin(2.0\alpha)}{0.188\sin(2.0\chi)+0.29\cos(2.0\alpha)\cos(2.0\chi)-0.363\cos(2.0\chi)\sin(2.0\alpha)+0.5}\right) \\ &-h\lambda_p\left(0.726\cos(2.0\alpha)\cos(2.0\chi)+0.58\cos(2.0\chi)\sin(2.0\alpha)\right) \\ &+\psi_3\left(\frac{0.726\cos(2.0\alpha)\cos(2.0\chi)-0.58\cos(2.0\chi)\sin(2.0\alpha)}{0.288\cos(2.0\alpha)\cos(2.0\chi)-0.188\sin(2.0\chi)+0.363\cos(2.0\chi)\sin(2.0\alpha)+0.5}\right) \\ &-h\lambda_p\left(0.726\cos(2.0\alpha)\cos(2.0\chi)-0.58\cos(2.0\chi)\sin(2.0\alpha)\right) \\ &+1.0\psi_4\left(\frac{0.376\cos(2.0\alpha)\cos(2.0\chi)-0.58\cos(2.0\chi)\sin(2.0\alpha)}{0.361\sin(2.0\chi)+0.29\cos(2.0\alpha)\cos(2.0\chi)+0.188\cos(2.0\chi)\sin(2.0\alpha)-0.5}\right) \\ &+1.0h\lambda_p\left(0.376\cos(2.0\alpha)\cos(2.0\chi)-0.58\cos(2.0\chi)\sin(2.0\alpha)\right) \end{aligned}$$

(A.2)

Fortunately, many of these terms cancel out, simplifying the equation to Equation (A.3).

$$\frac{dQ^{n+1}}{d\alpha} = \sum_{y} \begin{aligned} &\psi_1\left(\frac{0.376\cos(2.0\alpha)\cos(2.0\chi)+0.58\cos(2.0\chi)\sin(2.0\alpha)}{0.361\sin(2.0\chi)-0.29\cos(2.0\alpha)\cos(2.0\chi)+0.188\cos(2.0\chi)\sin(2.0\alpha)+0.5}\right) \\ &-\psi_2\left(\frac{0.726\cos(2.0\alpha)\cos(2.0\chi)+0.58\cos(2.0\chi)\sin(2.0\alpha)}{0.188\sin(2.0\chi)+0.29\cos(2.0\alpha)\cos(2.0\chi)-0.363\cos(2.0\chi)\sin(2.0\alpha)+0.5}\right) \\ &+\psi_3\left(\frac{0.726\cos(2.0\alpha)\cos(2.0\chi)-0.58\cos(2.0\chi)\sin(2.0\alpha)}{0.29\cos(2.0\alpha)\cos(2.0\chi)-0.188\sin(2.0\chi)+0.363\cos(2.0\chi)\sin(2.0\alpha)+0.5}\right) \\ &+\psi_4\left(\frac{0.376\cos(2.0\alpha)\cos(2.0\chi)-0.58\cos(2.0\chi)\sin(2.0\alpha)}{0.361\sin(2.0\chi)+0.29\cos(2.0\alpha)\cos(2.0\chi)+0.188\cos(2.0\chi)\sin(2.0\alpha)-0.5}\right) \end{aligned}$$

(A.3)

The next step involves substituting in ${\psi_{t,c}}^{n+1}$, which is the angle dependent portion of ${\psi_c}^{n+1}$, or ${\psi_{t,c}}^{n+1} = \frac{i_c \lambda_{pc}^{n+1} {\psi_c}^{n+1}}{h d_c}$. It is worth noting that while ψ_c in the above equation is

known based on the current estimates, $\psi_{t,c}^{\,n+1}$ is based upon the angles that are about to be calculated.

$$\frac{dQ^{n+1}}{d\alpha} = \sum_{y} \begin{array}{l} \psi_1\left(\frac{\left(\cos\left(2.0\alpha\right)+\cos\left(2.0\chi\right)\right)\left(0.376+0.58\tan\left(2.0\alpha\right)\right)}{\psi_{t,1}^{\,n+1}}\right) \\ -\psi_2\left(\frac{\left(\cos\left(2.0\alpha\right)+\cos\left(2.0\chi\right)\right)\left(0.726+0.58\tan\left(2.0\alpha\right)\right)}{\psi_{t,2}^{\,n+1}}\right) \\ +\psi_3\left(\frac{\left(\cos\left(2.0\alpha\right)+\cos\left(2.0\chi\right)\right)\left(0.726-0.58\tan\left(2.0\alpha\right)\right)}{\psi_{t,3}^{\,n+1}}\right) \\ -\psi_4\left(\frac{\left(\cos\left(2.0\alpha\right)+\cos\left(2.0\chi\right)\right)\left(0.376-0.58\tan\left(2.0\alpha\right)\right)}{\psi_{t,4}^{\,n+1}}\right) \end{array} \tag{A.4}$$

$$\frac{dQ^{n+1}}{d\alpha} = \sum_{y} \begin{array}{l} \psi_1\left(\frac{\left(0.376+0.58\tan\left(2.0\alpha\right)\right)}{\psi_{t,1}^{\,n+1}}\right) \\ -\psi_2\left(\frac{\left(0.726+0.58\tan\left(2.0\alpha\right)\right)}{\psi_{t,2}^{\,n+1}}\right) \\ +\psi_3\left(\frac{\left(0.726-0.58\tan\left(2.0\alpha\right)\right)}{\psi_{t,3}^{\,n+1}}\right) \\ -\psi_4\left(\frac{\left(0.376-0.58\tan\left(2.0\alpha\right)\right)}{\psi_{t,4}^{\,n+1}}\right) \end{array} \tag{A.5}$$

$$\frac{dQ^{n+1}}{d\alpha} = \sum_{y} \begin{array}{l} \psi_1\left(\frac{\left(0.648+\tan\left(2\alpha\right)\right)}{\psi_{t,1}^{\,n+1}}\right) \\ -\psi_2\left(\frac{\left(1.25+\tan\left(2\alpha\right)\right)}{\psi_{t,2}^{\,n+1}}\right) \\ +\psi_3\left(\frac{\left(1.25-\tan\left(2\alpha\right)\right)}{\psi_{t,3}^{\,n+1}}\right) \\ -\psi_4\left(\frac{\left(0.648-\tan\left(2\alpha\right)\right)}{\psi_{t,4}^{\,n+1}}\right) \end{array} \tag{A.6}$$

Unfortunately, setting this equation to 0 and solving for α does not yield a solution as is. However, if the assumption is made that the product of any three ${\psi_{t,c}}^{n+1}$ are equal, setting (A.6) equal to 0 and solving for α finds Equation (A.7). Unfortunately, this assumption is only true for certain specific combinations of angles.

$$\begin{aligned}\alpha^{n+1} &= \frac{1}{2}\tan^{-1}\left[\frac{-324\left(\psi_1-\psi_4+1.93\left(\psi_3-\psi_2\right)\right)}{-500\left(-\psi_1+\psi_2-\psi_3+\psi_4\right)}\right] \\ &= \frac{1}{2}\tan^{-1}\left[0.648\frac{\left(\psi_1-\psi_4+1.93\left(\psi_3-\psi_2\right)\right)}{\left(-\psi_1+\psi_2-\psi_3+\psi_4\right)}\right]\end{aligned} \tag{A.7}$$

Now the intermediate Stokes vector described in Section 3.2.2 is constructed. The elements are described below in Equation (A.8)

$$\begin{aligned}S_0^{n+1} &= \frac{1}{2}\psi_1+\psi_2+\psi_3+\psi_4 \\ S_1^{n+1} &= 0.865\left(-\psi_1+\psi_2+\psi_3-\psi_4\right) \\ S_2^{n+1} &= 0.562\left(\psi_1+\psi_4+1.93\left(\psi_3-\psi_2\right)\right) \\ S_3^{n+1} &= 0.564\left(\psi_2+\psi_3+1.93\left(\psi_1-\psi_4\right)\right)\end{aligned} \tag{A.8}$$

This allows the substitution to be made yielding Equation (A.9)

$$\alpha^{n+1} = \frac{1}{2}\tan^{-1}\left[\frac{S_2^{n+1}}{S_1^{n+1}}\right] \tag{A.9}$$

Appendix B: Proof for χ

Solving the optimization equation for χ follows a similar set of steps to those for α in Appendix A.

$$\frac{dQ^{n+1}}{d\chi}=\sum_{y}\sum_{c} \quad dh\lambda_{pc}^{n+1}\left(\begin{array}{l}\frac{1}{2}+\frac{\cos(2\alpha_n)\cos(2\chi_n)\left(\begin{array}{l}\cos(2\theta_c)^2\\+\cos(\phi_c)\sin(2\theta_c)^2\end{array}\right)}{2}\\-\frac{\sin(2\chi_n)\sin(2\theta_c)\sin(\phi_c)}{2}\\-\frac{\cos(2\chi_n)\sin(2\alpha_n)\cos(2\theta_c)\sin(2\theta_c)\left(\cos(\phi_c)-1\right)}{2}\end{array}\right)$$

$$-\frac{h\lambda_p\left(\begin{array}{l}\cos(2\alpha)\sin(2\chi)\left(\cos(2\theta_c)^2+\cos(\phi_c)\sin(2\theta_c)^2\right)\\+\cos(2\chi)\sin(2\theta_c)\sin(\phi_c)\\-\sin(2\alpha)\sin(2\chi)\cos(2\theta_c)\sin(2\theta_c)\left(\cos(\phi_c)-1\right)\end{array}\right)}{i_c\left(\begin{array}{l}\frac{\cos(2\alpha)\cos(2\chi)\left(\cos(2\theta_c)^2+\cos(\phi_c)\sin(2\theta_c)^2\right)}{2}-\frac{\sin(2\chi)\sin(2\theta_c)\sin(\phi_c)}{2}\\-\frac{\cos(2\chi)\sin(2\alpha)\cos(2\theta_c)\sin(2\theta_c)\left(\cos(\phi_c)-1\right)}{2}+\frac{1}{2}\end{array}\right)}$$

(B.1)

Also, as above, when the sum is taken across the channels, substituting in the angles for the individual channels and taking the sum across the channels simplifies the equation, causing the first term to cancel out and leaving Equation

$$\frac{dQ^{n+1}}{d\chi}=\sum_{y}\begin{matrix}\dfrac{\psi_1\left(0.723\cos\left(2.0\chi\right)+0.58\cos\left(2.0\alpha\right)\sin\left(2.0\chi\right)-0.376\sin\left(2.0\alpha\right)\sin\left(2.0\chi\right)\right)}{0.361\sin\left(2.0\chi\right)-0.29\cos\left(2.0\alpha\right)\cos\left(2.0\chi\right)+0.188\cos\left(2.0\chi\right)\sin\left(2.0\alpha\right)+0.5}\\ +\dfrac{\psi_2\left(0.374\cos\left(2.0\chi\right)-0.58\cos\left(2.0\alpha\right)\sin\left(2.0\chi\right)+0.726\sin\left(2.0\alpha\right)\sin\left(2.0\chi\right)\right)}{0.188\sin\left(2.0\chi\right)+0.29\cos\left(2.0\alpha\right)\cos\left(2.0\chi\right)-0.363\cos\left(2.0\chi\right)\sin\left(2.0\alpha\right)+0.5}\\ -\dfrac{\psi_3\left(0.374\cos\left(2.0\chi\right)+0.58\cos\left(2.0\alpha\right)\sin\left(2.0\chi\right)+0.726\sin\left(2.0\alpha\right)\sin\left(2.0\chi\right)\right)}{0.29\cos\left(2.0\alpha\right)\cos\left(2.0\chi\right)-0.188\sin\left(2.0\chi\right)+0.363\cos\left(2.0\chi\right)\sin\left(2.0\alpha\right)+0.5}\\ -\dfrac{\psi_4\left(0.58\cos\left(2.0\alpha\right)\sin\left(2.0\chi\right)-0.723\cos\left(2.0\chi\right)+0.376\sin\left(2.0\alpha\right)\sin\left(2.0\chi\right)\right)}{0.361\sin\left(2.0\chi\right)+0.29\cos\left(2.0\alpha\right)\cos\left(2.0\chi\right)+0.188\cos\left(2.0\chi\right)\sin\left(2.0\alpha\right)-0.5}\end{matrix}$$

(B.2)

This also can be simplified by removing a tangent term from the numerators and substituting in the $\psi_{t,c}{}^{n+1}$ in the denominator. This yields Equation (B.3)

$$\frac{dQ^{n+1}}{d\chi}=\sum_{y}\begin{matrix}\dfrac{\psi_1\left(0.723\cot\left(2.0\chi\right)+0.58\cos\left(2.0\alpha\right)-0.376\sin\left(2.0\alpha\right)\right)}{\psi_{t,1}{}^{n+1}}\\ +\dfrac{\psi_2\left(0.374\cot\left(2.0\chi\right)-0.58\cos\left(2.0\alpha\right)+0.726\sin\left(2.0\alpha\right)\right)}{\psi_{t,2}{}^{n+1}}\\ -\dfrac{\psi_3\left(0.374\cot\left(2.0\chi\right)+0.58\cos\left(2.0\alpha\right)+0.726\sin\left(2.0\alpha\right)\right)}{\psi_{t,3}{}^{n+1}}\\ -\dfrac{\psi_4\left(0.58\cos\left(2.0\alpha\right)-0.723\cot\left(2.0\chi\right)+0.376\sin\left(2.0\alpha\right)\right)}{\psi_{t,4}{}^{n+1}}\end{matrix}\qquad\text{(B.3)}$$

This equation also does not resolve when set to 0 and solved for χ. Thus, as with α, an established equation will be used instead. This equation will be updated with optimized values for both λ_p and λ_u and has been shown to yield reasonable solutions both in

simulation and in the laboratory experiments for the polarization angle and ellipticity of the given targets.

Bibliography

[1] J. Devitt, D. Forrai, M. Eismann and others, "Multi-Spectral Polarimetric Large Format IR-FPA's for Persistent Surveillance Applications," *DTIC,* 2007.

[2] D. A. Lemaster and S. C. Cain, "Multichannel blind deconvolution of polarimetric imagery," *Optical Society,* pp. 2170-2176, 2008.

[3] M. D. Morris, "Acoustic Imaging of Geosynchronous Satellites via a Newly Upgraded Hyper-Temporal Imaging Instrument," Marita D. Morris, Tucson, Arizona, 2018.

[4] "National Security Space Strategy Unclassified Summary," United States Government, Washignton DC, 2011.

[5] Office of the President of the United States of America, "National Space Policy of the United States of America.," United States Government, Washington DC, 2010.

[6] D. A. Lemaster, "Statistical Methods for Polarimetric Imagery," Air Force Institute of Technology, Wight Patterson Air Force Base, 2008.

[7] D. S. Sabatke, A. M. Locke, E. L. Dereniak, J. P. Garcia and T. C. P., "Design and development of a Snapshot Spectropolarimeter," in *Ground Target Modeling and Validation Conference*, Houghton, MI, 2002.

[8] M. W. Hyde, "Determining the Index of Refraction of an Unknown Object Using Passive Polarimetric Imagery Degraded by Atmospheric Turbulence," Air Force Institute of Technology, Wright Patterson Air Force Base, OH, 2010.

[9] J. W. Goodman, Introduction to Fourier Optics, New York, NY: W.H. Freeman and Company, 2017.

[10] E. Hecht, Optics (Fifth Edition), London, England: Pearson Education, 2017.

[11] J. D. Schmidt, Numerical Simulation of Optical Wave Propogation, Bellingham, WA: Society of Photo-Optical Instrumentation Engineers, 2010.

[12] G. Yoon, S. Pantanelli and S. MacRae, "Comparison of Zernike and Fourier Wavefront Reconstruction Algorithms in Representing Corneal Aberration of Normal and Abnormal Eyes," *Journal of Refractive Surgery,* vol. 24, pp. 582-590, 2008.

[13] L. Dai, S. Tong, L. Zhang and W. Yinhuan, "On simulation and verification of the atmospheric turbulent phase screen with Zernike polynomials," in *Photoelectronic Technology Committee*, Changchun, China, 2014.

[14] R. M. Aung, Improving Closely Spaced Dim Object Detection Through Improved Multi-Frame Blind Deconvolution, Wright Patterson Air Force Base, OH: Air Force Institute of Technology, 2020.

[15] AFIT, *zern_phase_screen.m,* WPAFB, OH: Air Force Institute of Technology, 2012.

[16] J. W. Goodman, Statistical Optics, New York City, NY: John Wiley & Sons, Inc, 2000.

[17] C. Byrne, "EM Algorithms," University of Massachusetts Lowell, Lowell, MA, 2011.

[18] T. Schulz, "Multiframe blind deconvolution of astronomical images," *Opt. Soc. Am.,* pp. 1064-1073, 1993.

[19] L. B. Wolff, "Polarization-based material classification from specular reflection," *IEEE Trans. Pattern Anal. Mach. Intelll.,* vol. 12, no. 11, pp. 1059-1071, 1990.

[20] S. Tominaga and A. Kamachi, "Polarization Imaging for Material Classification," *Opt. Eng.,* vol. 47, no. 12, p. 123201, 2008.

[21] D. A. Lemaster and M. T. Eismann, "Multi-Dimensional Imaging," in *Passive Polarimetric Imaging*, Chichester, West Sussex, United Kingdom, John Wiley & Sons, Ltd, 2014, pp. 391-428.

[22] D. S. Sabatke, M. R. Descour, E. L. Dereniak, W. C. Sweatt, S. A. Kemme and G. S. Phipps, "Optimization of Retardance for a Complete Stokes Polarimeter," *Opt. Lett.,* vol. 25, pp. 802-804, 2000.

[23] A. Ambarigan and D. Look Jr., "Optimum angles for a polarimeter: part I," *Optical Engineering,* vol. 34, no. 6, pp. 1651-1655, 1995.

[24] L. Shepp and Y. Vardi, "Maximum Likelihood reconstruction for emission tomography," *IEEE Trans. Med. Imaing,* pp. 113-122, 1982.

[25] R. Gerchberg and W. Saxton, "A practical algorithm for the determination of phase from image and diffraction plane pictures," *Optik,* vol. 35, no. 2, pp. 237-246, 1972.

[26] M. W. Hyde, "Determining the Index of Refraction of an," Air Force Institute of Technology, Wright Patterson Air Force Base, OH, 2010.

[27] J. Liu, Z. Ren, Z. Chen and Y. Liang, "A multi-frame blind deconvolution algorithm with the consistency constraints," in *Sixth Symposium on Novel Optoelectronic Detection Technology and*, Beijing, China, 2019.

[28] S. M. Kay, Fundamentals of Statistical Signal Processing, Upper Saddle River, New Jersey: Prentice Hall PTR, 1993.

REPORT DOCUMENTATION PAGE

Form Approved
OMB No. 0704-0188

1. REPORT DATE *(DD-MM-YYYY)*	2. REPORT TYPE	3. DATES COVERED *(From - To)*
08/09/2022	PhD Dissertation	August 2019 - August 2022

4. TITLE AND SUBTITLE
Multichannel Blind Deconvolution of Circularly Polarized Imagery

5a. CONTRACT NUMBER

5b. GRANT NUMBER

5c. PROGRAM ELEMENT NUMBER

6. AUTHOR(S)
Cunningham, Patrick Major

5d. PROJECT NUMBER

5e. TASK NUMBER

5f. WORK UNIT NUMBER

7. PERFORMING ORGANIZATION NAME(S) AND ADDRESS(ES)
Air Force Institute of Technology
Graduate School of Engineering and Management (AFIT/EN)
2950 Hobson Way
Wright-Patterson AFB OH 45433-7765

8. PERFORMING ORGANIZATION REPORT NUMBER
AFIT-ENG-DS-22-S-014

9. SPONSORING/MONITORING AGENCY NAME(S) AND ADDRESS(ES)
Intentionally Left Blank

10. SPONSOR/MONITOR'S ACRONYM(S)

11. SPONSOR/MONITOR'S REPORT NUMBER(S)

12. DISTRIBUTION/AVAILABILITY STATEMENT
DISTRIBUTION STATEMENT A.
APPROVED FOR PUBLIC RELEASE; DISTRIBUTION IS UNLIMITED.

13. SUPPLEMENTARY NOTES
This work is declared a work of the U.S. Government and is not subject to copyright protection in the United States.

14. ABSTRACT
Current methods can be used to recreate an expected Stokes polarization vector from measured light for characterization purposes. However, this only applies to three of the Stokes parameters, that is, the linear polarization components. Circular polarization is not currently being utilized for object characterization because the mathematical complexity is greater than for that of linear polarization. This research will analyze a way to expand existing algorithms to include circular polarization and enable the complete reconstruction of the Stokes vector from the measured light into a blind deconvolution algorithm for Stokes estimation and image reconstruction.

15. SUBJECT TERMS
Stokes parameters, circular polarization, expectation maximization, blind deconvolution

16. SECURITY CLASSIFICATION OF:			17. LIMITATION OF ABSTRACT	18. NUMBER OF PAGES	19a. NAME OF RESPONSIBLE PERSON
a. REPORT	b. ABSTRACT	c. THIS PAGE			Lt Col David J. Becker, AFIT/ENG
					19b. TELEPHONE NUMBER *(Include area code)*
U	U	U	UU	138	937-255-3636 x4371 david.becker@afit.edu